Techniques for understanding anomalous radar spectra.

PORTEOUS, Joyce.

Fines are charged at 50p per hour

REFERENCE

Techniques for Understanding Anomalous Radar Spectra

Joyce Porteous

A thesis submitted in partial fulfilment of the requirements of
Sheffield Hallam University
for the degree of Master of Philosophy

May 2004

Abstract

This thesis concerns the investigation of the Earth's upper atmosphere, ionosphere and magnetosphere. In particular, it involves a study of the F region, using EISCAT Svalbard Radar data.

Anomalous ion line spectra have been identified in many of the radar experiments which have been conducted at that site. Such spectra are defined as deviations from the standard symmetric "double-humped" spectra derived from incoherent scatter radar echoes from the upper atmosphere. Some anomalous spectra — where there are sharp enhancements of power over restricted height ranges — have been attributed to satellite contamination in the beam path. Here we outline a method for detecting such contamination, and review in detail a few cases where the method enables the identification of anomalous spectra as satellite echoes, subsequently ascribed to specific orbital objects. The methods used here to identify such satellites provide a useful way of distinguishing anomalous spectra due to satellites from those of geophysical origin. Analysis of EISCAT Svalbard Radar data reveals that an average of 8 satellites per hour are found to cross the beam. Based on a relatively small sample of the data set, it appears that at least half of the occurrences of anomalous spectra are caused by satellite contamination rather than being of geophysical origin.

Those anomalous spectra which cannot be explained by satellite contamination appear to occur most frequently during or immediately before magnetic storms, as can be seen when compared with the Dst index and magnetometer data. A model of the chemical structure of the ionosphere is proposed. This gives predictions for the intensity ratios of the 6300Å and 5577 Å emission lines and these are compared with readings from the meridian scanning photometer at Adventdalen.

Acknowledgements

For making this thesis possible and for sustaining me throughout its construction thanks are given to:

Keith A. Berrington, as Director of Studies for his continued support and encouragement, and for introducing me to aspects of atomic chemistry.

Andy M. Samson, as supervisor for his continued support and advice and for introducing me to the theories of the upper atmosphere.

Jeff A. Waldock, as supervisor and especially for his helpful advice when downloading computer software.

Ian W. McCrea, as external advisor, for his support and help with regard to the use of the Rutherford Appleton computer system.

The staff at the Rutherford Appleton Laboratory who were involved in the introductory Workshop at which I gain first hand knowledge of the radars and the system for gaining access to the data, and who were always willing to provide support, especially Steve Crowthers and Paul Gallop.

The Director and staff of EISCAT, for opening the facility and supplying the data.

Mike T. Rietveld, for his helpful suggestions at both the 9th EISCAT Workshop in Tokyo, Japan, 2001, and the 10th EISCAT Workshop in Menlo Park, U.S.A., 2003, and who along with Russell Eberst and Alan Pickup provided helpful suggestions for obtaining the satellite data and directing me to appropriate tracking programs.

Rick von Glahn, for allowing me to use results from the Element Manager for Windows program.

Francis Sedgemore-Schulthess, for supplying the "iaspec" program and for his help in evaluating the published paper.

Charles Deehr, of the Geophysical Institute of the University of Alaska Fairbanks, for making the photometer data available.

All those who presented papers at the EISCAT summer school in Menlo Park, U.S.A., 2003, especially Francois R.E. Forme, Jean-Paul St-Maurice and Tony van Eyken for their encouragement.

Contents

Chapter page

Abstract i

Acknowledgements ii

Contents iv

List of Figures viii

List of Tables xii

Glossary xiii

1 Introduction **1**

1.1 The Earth's Atmosphere 1

1.2 The Ionosphere 4

1.2.1 Ionisation 7

1.2.2 Recombination 9

1.2.3 Chemical Reactions 11

1.2.4 Photodissociation 12

1.2.5 Excitation 12

1.2.6 Radiative Decay 12

1.2.7 Reaction Rates 13

1.3 The Magnetosphere 14

2 Techniques and Instruments **19**

2.1 Scatter Techniques 19

2.1.1 Coherent scatter 19

2.1.2 Incoherent scatter 20

2.2 Incoherent Scatter Radars 21

2.2.1 EISCAT Mainland Radars 23

2.2.2 EISCAT Svalbard Radar (ESR) 23

2.3 GUP3 Experiment 24

2.4 Theory of Spectra 26

2.5 Measurements Obtained 30
2.5.1 Electron Density 31
2.5.2 Electron and Ion Temperature Ratio 31
2.5.3 The Ion Temperature and Ion Mass Ratio 32
2.5.4 The Ion Mass 32
2.5.5 The Plasma Velocity 32

3 Background Theory **33**
3.1 Background 33
3.2 Millstone Hill Radar 38
3.3 EISCAT VHF (933 MHz) and UHF (224 MHz) Radars 40
3.4 EISCAT Svalbard Radar 50

4 Program Techniques **53**
4.1 Searching for Enhanced Spectra in the Data 53
4.2 The Software 55
4.3 Identification of Enhanced Spectra 61
4.4 Long Pulse and Alternating Code Comparisons 69

5 Satellites **72**
5.1 Satellite Contamination 72
5.2 Orbital Elements 73
5.2.1 Inclination 75
5.2.2 Right Ascension of Ascending Node 75
5.2.3 Argument of Perigee 76
5.2.4 Eccentricity 76
5.2.5 Mean Motion 77
5.2.6 Mean Anomaly at epoch 77
5.3 Two-Line Element Files 78
5.4 Tracking Satellites 79
5.5 Checking for Satellites 91
5.6 Comparison with Known Events 96
5.7 Further Modifications to the Subroutine 99

6 Research Outcomes: Space Storms **102**

6.1 Classification of Data 102

6.2 Case Studies 110

6.2.1 Magnetic Storm of 26th August 1998 110

6.2.2 Magnetic Storm of 24th–25th September 1998 114

6.2.3 11th February 1999 119

6.2.4 12th February 1999 124

6.2.5 3rd December 1999 129

6.3 Proposed Atomic Model 134

7 Conclusions **143**

7.1 Satellites 143

7.2 Naturally Enhanced Ion Acoustic Spectra 146

Bibliography 148

Appendix A 155

Appendix B 163

Appendix C 165

Appendix D 167

Appendix E 171

Published Paper 175

List of Figures

Figure		Page
1.1	To show the relation between the Earth's geographical coordinate system and the geomagnetic coordinate system	15
1.2	To show the relationship between the Cartesian coordinate system, (*X*, *Y*, *Z*), and the cylindrical polar coordinate system, (*H*, *D*, *Z*), used at ground stations to measure the magnetic field, **B**	17
2.1	Diagram to show the expected spread in the returned frequencies, due to Doppler shifts, if the radar beam were scattered by the individual electrons	27
2.2	Diagram to show the expected spread in the returned frequencies, due to Doppler shifts, if the radar beam were scattered not by "free" electrons, but by the ions surrounding the electrons	27
2.3	Diagram of theoretical spectrum obtained using the 'iaspec' program with radio frequency = 500 MHz, electron temperature = 2500 K, electron density = 1.5e11 m^{-3}, ion temperature = 1500 K	29
3.1	Theoretical spectra obtained using the 'iaspec' program with radio frequency = 500 MHz, electron temperature = 2500 K, electron density = 1.5e11 m^{-3}, ion temperature = 1500 K and parallel drift = –10, –50 and –100 km/sec, respectively	35
3.2	Theoretical spectra obtained using the 'iaspec' program with radio frequency = 500 MHz, electron temperature = 2500 K, electron density = 1.5e11 m^{-3}, ion temperature = 1500 K and parallel drift = 10, 50 and 100 km/sec, respectively	36

3.3	Theoretical spectra obtained using the 'iaspec' program with radio frequency = 500 MHz, electron temperature = 3000 K and 4500 K respectively, electron density = 1.5e11 m^{-3}, ion temperature = 1500 K and parallel drift = 0 km/sec	37
4.1	Typical rtg program output showing, on the left, a contour plot of the normalised spectra and, on the right, the same spectra shown as a stacked plot for the LP2 channel at 10:53:59 UT on 1st December 1999	56
4.2	A typical spectrum from the right hand panel of the rtg plot window with an indication of the region which was omitted from the search for the secondary peak	56
4.3	Distribution of peak ratios obtained using data from the GUP3 experiments for 1st – 4th December 1999	60
4.4	Results showing (a) spectra and (b) power profile for LP2 data at 10:31:19 UT, 1st December 1999, using EISCAT rtg3 program when a probable satellite was seen in the beam	62
4.5	Results showing (a) spectra and (b) power profile for LP2 data at 11:55:49 UT, 1st December 1999, using EISCAT rtg3 program when enhanced spectra probably due to geophysical causes were seen in the beam	64
4.6	EXCEL charts showing the rtg3 subroutine's calculated values for the power using the LP2 data of 1st December 1999. The charts shown were considered to be typical of (a) a probable satellite, (b) a possible satellite and (c) a possible enhancement due to a geophysical phenomenon	66
4.7	Power profiles obtained using rtg3 for (a) a probable satellite, (b) a possible satellite and (c) a possible enhancement due to a geophysical phenomenon	68
4.8	Histogram showing frequency of occurrence of ln of power ratios obtained when enhanced spectra occurred in the 1st and 2nd December 1999 ESR, GUP3 data	69

4.9	Results showing (a) spectra and (b) power profile for AC2 data at 10:31:19 UT, 1st December 1999, using EISCAT rtg3 program when a probable satellite was seen in the beam	71
5.1	Diagrams to show the orbital elements used to describe the motion of a satellite (a) with respect to the Earth and (b) within an orbit. (http://spaceflight.nasa.gov/realdata/elements/graphs.html)	74
5.2	Geometric showing the elliptical orbit of a satellite, *S*, and its encircling circular orbit	84
5.3	Geometric showing the measurements required to calculate the geographical latitude of a satellite, *S*	88
5.4	Geometric showing the measurements required to calculate the geographical latitude of a satellite, *S*	89
5.5	Path of space debris, NORAD number 24134-94029GH, showing its position relative to the radar at ESR at 10:31:13 UT on 1st December 1999	92
5.6	Geometrical construct to find *z*, the distance between the centre of the radar beam (*R*) and the object (*S*) from the angles given relative to the zenith (*Z*)	92
5.7	Geometric to find the closest distance between the radar beam (*R*) and the orbital object as it travels from position S_1 to position S_2	95
5.8	(a) Power profile for a probable satellite passing through the beam in the GUP0 data and (b) for a geophysical incident in the GUP0 data of 28th January 1998	98
5.9	Examples of (a) a geophysical event and (b) a satellite contamination event found in the GUP3 December 1999 data using the automated subroutine	101
6.1	Example of data dump classified as being due to noise when spectra in adjacent ten-second data dumps appear to be normal	104
6.2	Example of ten-second data dump classified as being noise in the background signal	104

6.3	(a) Typical spectra identified as being of geophysical origin in the GUP3 data and (b) the corresponding power profile	106
6.4	Typical example (a) showing spectra with similar features as those of a satellite with a Doppler shift greater than 4.5 and (b) the corresponding power profile which does not show any evidence of a significant change	107
6.5	Dst indices for 26th and 27th August 1998	111
6.6	Magnetogram showing the stack-plot of the H component of the magnetic field at various stations including Longyearbyen (lyb) on 26th August 1998 obtained from http://geo.phys.uit.no/geomag.html	112
6.7	Two sequences of spectra which include examples of anomalous spectra which occur in the data of 26th August 1998	113
6.8	Examples of typical anomalous spectra which occur in the data dumps of 24th September 1998	115
6.9	Examples of typical anomalous spectra which occur in the data dumps of 25th September 1998	116
6.10	Dst indices for 24th and 25th September 1998	117
6.11	Magnetogram showing stack-plot of the H component of the magnetic field at various stations including Longyearbyen (lyb) on 24th/25th September 1998 obtained from http://geo.phys.uit.no/geomag.html	118
6.12	Examples of typical anomalous spectra which occur in the data dumps of 11th February 1999	120
6.13	Meridian scanning photometer data for 11th February 1999	122
6.14	Magnetogram showing the stack-plot of the H component of the magnetic field at various stations including Longyearbyen (lyb) on 11th February 1999 obtained from http://geo.phys.uit.no/geomag.html	123
6.15	Examples of typical anomalous spectra which occur in the data dumps of 12th February 1999	125
6.16	Meridian scanning photometer data for 12th February 1999	126

6.17	Magnetogram showing stack-plot of the H component of the magnetic field at various stations including Longyearbyen (lyb) on 12th February 1999 obtained from http://geo.phys.uit.no/geomag.html	127
6.18	Dst indices for 11th and 12th February 1999	128
6.19	Examples of typical anomalous spectra which occur in the data dumps of 3rd December 1999	130
6.20	Meridian scanning photometer data for 3rd December 1999	131
6.21	Magnetogram showing stack-plot of the H component of the magnetic field at various stations including Longyearbyen (lyb) on 3rd December 1999 obtained from http://geo.phys.uit.no/geomag.html	132
6.22	Dst indices for 2nd, 3rd and 4th December 1999	133
6.23	Schematic diagram of excitation levels of oxygen	134
6.24	EXCEL chart showing the intensity ratio, $(I_{630.0}/I_{557.7})$, for 3rd December 1999 as calculated from the 98° photometer scan	140
6.25	EXCEL chart showing the intensity ratio, $(I_{630.0}/I_{557.7})$, for 11th February 1999 as calculated from the 98° photometer scan	142
6.26	EXCEL chart showing the intensity ratio, $(I_{630.0}/I_{557.7})$, for 12th February 1999 as calculated from the 98° photometer scan	142

List of Tables

Table		Page
5.1	The satellite parameters as entered in the fourth and following rows of the EXCEL spreadsheet used to identify the items whose positions needed to be checked at a specified time	80
5.2	The entries in the first row of the EXCEL spreadsheet used to identify the items whose positions needed to be checked at a specified time	81
5.3	The entries, containing formulae to estimate the positions of the items needed to be checked at a specified time, taken from the fourth row of the EXCEL spreadsheet	82
5.4	A sample of times at which a satellite or item of space debris appeared within the ESR beam on 1st December 1999	94
6.1	Details of naturally enhanced ion-acoustic spectra (NEIAS) identified in the Common Program GUP3 data between August 1998 and March 2000	108
6.2	Details of lifetimes of occurrences of naturally enhanced ion-acoustic spectra	109
7.1	The number of satellites and possibly naturally enhanced spectra found in the region covered by the ESR beam for 10:11:30 to 13:00:00 UT on 1st December 1999	144

Glossary

character	page
P = pressure at height h	2
P_0 = pressure at height $h = 0$	2
m = molecular (or atomic) mass	2
g = acceleration due to gravity $= 9.81\,\mathrm{m\,s^{-2}}$	2
h = height above the Earth's surface	2
k = Boltzmann's constant $= 1.38\times10^{-23}\,\mathrm{J\,K^{-1}}$	2
T = temperature	2
$H = \dfrac{kT}{mg}$ = scale height	2
f = radio frequency	5
N_e = electron density	5
n = refractive index	5
e = electron charge $= 1.60\times10^{-19}$ C	5
m_e = rest mass of an electron $= 9.11\times10^{-31}$ kg	5
ε_0 = permitivity of free space $= 8.85\times10^{-12}\,\mathrm{F\,m^{-1}}$	5
f_P = plasma frequency	5
T_e = electron temperature	9
T_i = ion temperature	9
T_n = neutral temperature	9
$T_R = (T_i + T_n)/2$	11
(λ_P, φ_P) = geographic spherical polar coordinates for the north geomagnetic pole, P, with origin at the Earth's centre, (78.8°N, 289.1°E)	14
(λ, φ) = the geographic coordinates, used to describe the latitude and longitude for a place on the Earth	14

(λ_m, φ_m) = the geomagnetic coordinates for a point on the Earth 14

B = magnetic field 16

(H, D, Z) = cylindrical coordinates for **B** 16

(X, Y, Z) = Cartesian coordinates for **B** 16

c = speed of light $= 3 \times 10^8$ m s^{-1} in vacuo 19

λ_D = Debye length 20

λ = wavelength of the radar signal 26

V = velocity of the ion-acoustic wave 26

$\Lambda = \frac{1}{2}\lambda$ = wavelength of the ion-acoustic wave 28

$F(\Lambda)$ = frequency shift caused by the Doppler effect 28

m_i = rest mass of the ion 28

V_P = plasma velocity 30

E = electric field 30

σ_1 = Pedersen conductivity 30

σ_2 = Hall conductivity 30

P_R = total power returned from the scattering region 31

σ_e is the scattering cross section of an electron $= 9.98 \times 10^{-29}$ m 31

$\alpha = 4\pi\lambda_D / \lambda$ 31

i = angle of inclination between plane
of equator and plane of elliptical orbit 75

Ω = right ascension of the ascending node,
measured in the equatorial plane, from the first point of Aries 76

ω = argument of perigee 76

e = eccentricity 76

a = semi-major axis of ellipse 76

T_o = mean motion 77

τ = epoch 78

ν_0 = true anomaly 78

ψ_τ = mean anomaly at epoch 80

R_E = mean radius of Earth $= 6.379 \times 10^6$ m 81

M_E = mass of the Earth $= 5.975 \times 10^{24}$ kg 81

G = constant of gravity $= 6.673 \times 10^{-11}$ N m^2 kg^{-2} 81

b = semi-minor axis of ellipse 82

d = distance from line of nodes to satellite 82

θ = eccentric anomaly 85

ψ_t = mean anomaly 86

λ_s = latitude of satellite 87

θ_γ = longitude of first point of Aires

D solar days after the Vernal Equinox 88

θ_s = longitude of satellite 89

n_1 = population of electrons in the ^{1}D state 135

n_2 = population of electrons in the ^{1}S state 135

n_0 = population of electrons in the $^3P_{2,1,0}$ state 135

A_{ij} = radiative decay rates from state i to j 135

C_{ij} = collisional excitation/de-excitation rates from state i to j 135

r = fraction of electron population which is thermal 135

$I_{630.0}$ = emission intensity of the 6300Å line 138

$I_{557.7}$ = emission intensity of the 5577Å line 138

$A_{630.0}$ = Einstein transition probability

for the emission at 6300Å $= 6.54 \times 10^{-3}$ 138

$A_{557.7}$ = Einstein transition probability

for the emission at 5577Å $= 1.124$ 138

Chapter 1

Introduction

This thesis concerns the investigation of the upper atmosphere, so we begin with a brief description of the Earth's atmosphere, the ionosphere and the magnetosphere. We will later look at radar, magnetometer and photometer data.

1.1 The Earth's Atmosphere

Near the Earth's surface the relatively dense atmosphere mainly consists of molecular nitrogen (~80%) and oxygen (~20%), and a small amount (less than 1%) of carbon dioxide, water vapour and other trace gases. As the height above the Earth's surface increases so the pressure and density decrease. At 5.5 km above the Earth's surface the air pressure is ~ ½ of that at sea level (i.e. ½ × normal pressure). At 50 km it is ~ $1/1000$ × normal pressure (Bugoslavskya, 1962).

In addition to its composition, it is clear that a most important feature of the atmosphere is the decrease of pressure and density with increasing altitude. Many properties of the atmosphere can be derived from this information. One of these is the barometric equation, sometimes called the hydrostatic equation. This gives:

$$P = P_0 \exp\left(-\frac{mgh}{kT}\right),$$

where P = pressure at height h,

P_0 = pressure at height $h = 0$,

m = molecular (or atomic) mass,

g = acceleration due to gravity,

h = height above the Earth's surface,

k = Boltzmann's constant, and

T = temperature.

The above equation can be written as:

$$P = P_0 \exp\left(-\frac{h}{H}\right),$$

where $H = \frac{kT}{mg}$ = scale height.

We can show that the scale height is equivalent to the height above the Earth's surface to which the atmosphere would extend if it had a constant density. If this were truly the case the atmosphere would only extend to a height of ~8.3 km.

If in the equation for H, both k and g are considered to be constants, we can see that, for a constant mass, H is proportional to T. This means that, for an isothermal

atmosphere, if the temperature, T, increases then the scale height, H, of the atmosphere increases and vice versa. So the atmosphere can expand and contract. Although in reality the value of g does vary with height we can still find a local value for the scale height, H.

In the lower part of the atmosphere the gas molecules are well mixed and the mean molecular mass (28.8) is used to determine the scale height. However, the temperature between the ground and 100 km altitude varies quite markedly and so the scale height varies between 5.0 and 8.3 km (Brekke, 1997).

At heights above 100 km, the temperature increases and the molecules dissociate so that the molecular mass decreases. This results in each component taking up its individual scale height depending upon its mass. These masses vary considerably ($H = 1, He = 4, O = 16, N_2 = 28, O_2 = 32$). So the lighter gases (helium and hydrogen) which are only trace elements in the lower regions become relatively more abundant as the height increases. This explains why different gas molecules are dominant in different regions, with helium and hydrogen being dominant in the highest region and oxygen atoms being the dominant species from 400 km to 1000 km. However, it must be remembered that the precise detail of the composition is not only dependent upon the scale height but it also depends upon the temperature.

It is possible for individual atoms to escape from the Earth's gravitational attraction. In fact this loss is only significant for hydrogen. However at the same time hydrogen is being replenished in the form of protons and electrons carried by the solar wind.

1.2 The Ionosphere

It is the Sun's ultra-violet rays and the solar wind penetrating the upper atmosphere which ionise the gases. Since the pressure is low in this region, recombination does not happen quickly so there is a permanent population of ions and free electrons (usually in approximately equal numbers). In the region above 400 km from the Earth's surface approximately 0.1% of the gases in this region are ionised (Brekke, 1997). This ionised part of the Earth's atmosphere is known as the ionosphere. It is said to be in a state of dynamic equilibrium. This means that although when looked at in totality it is in a state of equilibrium (i.e. the percentage of ionised particles is remaining constant), in contrast, the particles of which it consists are in a perpetual state of change. So, for example, whilst some oxygen atoms may be being ionised to form oxygen ions and free electrons, at the same time, there will be some oxygen ions combining with an electron to form oxygen atoms. This is shown chemically as:

$$O \rightleftharpoons O^+ + e^-$$

In general, many different reactions are occurring at the same time within the ionosphere but the overall effect is to keep the composition constant.

The density of the ionisation in the ionosphere is normally lower at night than it is in the daytime. This density also varies with the time of year, the solar cycle, the latitude and the level of magnetospheric, or solar wind, disturbance.

The existence of an ionised conducting layer in the upper atmosphere was fully proved in 1924. This was achieved by Appleton and Barnett (1925) in England as well as Breit and Tuve (1926) in the U.S.A. studying the reflections of radio waves from the atmosphere. Appleton and Barnett used a continuous wave transmitter, whilst Breit and Tuve used pulsed radio signals (Beynon and Williams, 1978). By noting the

time which elapsed before the reflected signal was returned and knowing the speed at which the signal was travelling, the height of the reflecting layer could be estimated.

These early experiments showed that there was a region in the upper atmosphere where the ionisation of the gases provided a reflecting layer. The refractive index of such a medium depends upon its electron density. For a radio frequency, f, and a medium of electron density, N_e, the refractive index, n, is given by the equation:

$$n = \left(1 - \frac{e^2 N_e}{4\pi^2 \varepsilon_0 m_e f^2}\right)^{1/2}$$

where e = electron charge,

m_e = rest mass of an electron, and

ε_0 = permitivity of free space.

If n is equal to 1 the signal will pass through the medium without being refracted. For smaller values of n the signal will be refracted away from the normal. The signal will be reflected as the value of n approaches zero. This means that for a medium of electron density N_e a signal of frequency f_P will be reflected if:

$$f_P = 9 N_e^{1/2} \text{ Hz.}$$

This value of f_P is referred to as the plasma frequency.

Initially the experiments used fixed radio frequencies, but within a few years the experiments were carried out using different frequencies. As a result, different layers were found in the ionosphere. These layers are referred to as regions.

The D region is the closest to the Earth's surface (altitude 60–90 km). It is very variable and has a low electron density ($\sim 10^9$ m^{-3}).

The E region (altitude 90–160 km) was historically the first region to be detected, and thus named because of its ability to reflect electromagnetic waves.

The F region typically has a maximum electron density ($\sim 10^{12}$ m^{-3}) around 300 km above the Earth's surface though this can vary between 200 and 600 km. A peak sometimes occurs below this maximum, for example during auroral events. In this case the region of the lower peak is referred to as the F1 region and that of the upper peak is called the F2 region.

The maximum plasma frequency of a given layer is the critical frequency of that layer. As we move further from the surface of the Earth the electron density of the ionosphere increases (until a peak is reached in the F region), so the critical frequency increases for each region as we move from the D region outwards to the F2 region. The maximum critical frequency is referred to as the penetration frequency. A signal of any higher frequency than the penetration frequency, which is vertically incident, will pass straight through the whole of the ionosphere without reflection and will be lost into space.

The ionosphere can be treated as a partially ionised plasma in which the electron density is almost equal to the ion density. It can support strong electric currents and, as a plasma, it both supports and generates a variety of waves, interactions and instabilities which are not present in a neutral gas. There are six key processes which describe the reactions which occur between the electron and ion populations:

1. Ionisation
2. Recombination
3. Chemical Reactions
4. Photodissociation
5. Excitation
6. Radiative decay

The ionosphere is formed by the ionisation of atmospheric gases such as N_2, O_2 and O. At low and middle latitudes the energy required comes from solar radiation ($h\nu$) in the X-ray and extreme ultra-violet (EUV) regions of the spectrum. Another source of ionisation, which is also present at low latitudes but has greater importance at high latitudes, is energetic particles. The sources of such particles at high latitudes are auroral electrons, energetic photoelectrons, and protons which may be emitted from the Sun during solar flares.
Generally, the solar radiation can be expected to be the primary source of ionisation during the daytime when it will enhance the electron and ion populations. However, some background ionisation will occur throughout the whole 24 hours because of the auroral effects.

During dissociative recombination the electron and ion populations will recombine causing depletions during the night. The rate of recombination depends critically on the availability of particular molecular ions. Although the ionisation process produces a supply of charged particles, there are also chemical reactions taking place, which will rearrange the ion population and so affect the recombination rates.

The following sub-sections consider each of the five key processes which occur between the electron and ion populations in the ionosphere in greater detail.

1.2.1 Ionisation

This is the process in which the radiation combined with the atoms or molecules produces ions and electrons. The most important reactions involve nitrogen and oxygen:

The photoionisation reactions are:

$$h\nu(<1026\text{Å}) + O_2 \rightarrow O_2^+ + e^- \quad (1.1)$$

$$h\nu(<910\text{Å}) + O \rightarrow O^+ + e^- \quad (1.2)$$

$$h\nu(<796\text{Å}) + N_2 \rightarrow N_2^+ + e^- \quad (1.3)$$

The dissociative ionisation reactions are:

$$h\nu(<662\text{Å}) + O_2 \rightarrow O^+ + O + e^- \quad (1.4)$$

$$h\nu(<510\text{Å}) + N_2 \rightarrow N^+ + N + e^- \quad (1.5)$$

The ultraviolet (UV) radiation wavelengths (Å) shown in these equations correspond to the ionisation thresholds required for the production of ions in their ground state. Because $h\nu < 1026\text{Å}$ includes more of the solar spectrum than the other wavelengths shown, we expect reaction (1.1) to be the dominant source of electrons. The energy of a photon is inversely proportional to the wavelength, i.e.

$$\text{Energy(eV)} \approx \frac{12400}{\text{Wavelength(Å)}}.$$

The photons in the equations above may be replaced with energetic electrons having equivalent kinetic energy. Some of the photoelectrons and auroral electrons can have sufficient energy to enable them to ionise the atoms and molecules in the ionosphere. For example, the ionisation energy of O_2 is 1026Å ($\approx \frac{12400}{1026} \approx 12\,\text{eV}$), so if a 500Å ($\approx 25\,\text{eV}$) photon hits an O_2 molecule as in equation (1.1) then the resulting photoelectron can carry away up to 13 eV.

$$h\nu(\approx 25\,\text{eV}) + O_2 \rightarrow O_2^+ + e^-(\approx 13\,\text{eV})$$

Since the resulting photoelectron still has more than 12 eV of energy it will be able to perform another ionisation:

$$e^-(>12\,eV) + O_2 \rightarrow O_2^+ + e^- + e^-$$

So, an auroral electron, with approximately 6 keV, say, could ionise up to 500 times in this way.

Although the solar radiation in the upper atmosphere approximates to that of a black body distribution, the electrons produced by the equations (1.1) to (1.5), which carry excess energy with them, can have a range of energies depending upon the final states of the reactants. The distribution of these energies cannot be said to be thermal in the sense of having a definite temperature. However, the electron population will tend towards thermal equilibrium as a result of inelastic collisions with neutrals and ions. The energy of the electron population will be reduced, and some atoms and molecules will be promoted to their exited states. The ions are heavier than the electrons and interact more strongly with the neutrals. Since the ions and neutrals have similar masses, much of the excess energy of the ions is transferred to the neutral gas. These collisions will eventually cause the electron temperature, T_e, to approach the same value as the ion temperature, T_i, or the neutral temperature, T_n, though, in general the relation

$$T_e > T_i > T_n \approx 900\,K$$

is typical of the F region.

1.2.2 Recombination

The dominant cause of the reduction in the electron and ion population is dissociative recombination of molecular ions as shown in the following equations, where "*" indicates the excited state.

$$e^- + O_2^+ \rightarrow O + O^* + 5\,eV \qquad [T_e^{-0.5}] \qquad (1.6)$$

$$e^- + N_2^+ \rightarrow N^* + N^* + 1.04\,eV \qquad [T_e^{-0.39}] \qquad (1.7)$$

$$e^- + NO^+ \rightarrow N + O + 2.75\,eV \qquad [T_e^{-0.85}] \qquad (1.8)$$

In general the dissociative recombination rates are inversely proportional to the electron temperature, as shown in brackets. Hence as the gas cools overnight then recombination will occur.

Radiative recombination may cause a minor depletion in the electron and ion population. This produces oxygen atoms by the following reaction:

$$e^- + O^+ \rightarrow O + h\nu \qquad (1.9)$$

However this process is rather slow relative to the other reactions.

The process of recombination is controlled by the concentration of the molecular ions. In practice the processes described above cannot be the only recombination mechanisms, since they would result in the atmosphere becoming entirely atomic. There are other mechanisms, such as those involving three body reactions to molecules, but these are mainly important below 100 km.

The O_2^+ and N_2^+ required for the reactions in equations (1.6) and (1.7) are produced by the primary reactions in equations (1.1) and (1.3). In contrast, the NO^+ in equation (1.8) requires a chemical source. In fact, NO^+ is considered to be the dominant ion in the E region.

1.2.3 Chemical Reactions

The most important chemical sources for molecular ions are:

$$N^+ + O_2 \rightarrow N + O_2^+ + 2.46\,eV \qquad [\text{constant}] \qquad (1.10)$$

$$O^+ + O_2 \rightarrow O + O_2^+ + 1.55\,eV \qquad [T_R^{-0.4}] \qquad (1.11)$$

$$(O^+)^* + N_2 \rightarrow O + N_2^+ + 1.33\,eV \qquad [\text{constant}] \qquad (1.12)$$

$$N^+ + O_2 \rightarrow O + NO^+ + 6.67\,eV \qquad [\text{constant}] \qquad (1.13)$$

$$O^+ + N_2 \rightarrow N + NO^+ + 1.10\,eV \qquad \begin{bmatrix} T_R^{\,2} \text{ above } 1000K \\ \text{constant below } 1000K \end{bmatrix} \qquad (1.14)$$

where the dependence on the temperature of the rates of the chemical reactions are as shown in the brackets and $T_R = (T_i + T_n)/2$.

Notes:

- Equations (1.10) and (1.11) are chemical sources of O_2^+, which can recombine with electrons as in equation (1.6).
- Equations (1.12) is a chemical source of N_2^+, which can recombine with electrons as in equation (1.7).
- Equations (1.13) and (1.14) are chemical sources of NO^+, which can recombine with electrons as in equation (1.8).
- Equations (1.11) to (1.13) are chemical sources of O.

The ionisation processes explained earlier in 1.2.1 also produce O_2^+ and N_2^+, but (1.14) is the principal source of NO^+.

1.2.4 Photodissociation

The main source of atomic O is photodissociation of O_2.

$$h\nu(< 2422\text{Å}) + O_2 \rightarrow O + O \qquad (1.15)$$

Since shorter wavelengths equate to greater energy levels, when the wavelength of $h\nu$ is less than 1749Å then the ^1D excited state of O is energetically accessible. This is a copious source of excited O.

At 300 km, 99% of the oxygen is atomic rather than molecular, but only about 15% of the nitrogen is atomic because of the lower dissociation of O_2 relative to N_2.

1.2.5 Excitation

This does not change the ionisation balance or chemistry, but it is an important cooling mechanism, for example

$$e^- + N_2(v = 0) \rightarrow e^- + N_2(v > 0)$$

and

$$e^- + O \rightarrow e^- + O^*$$

1.2.6 Radiative Decay

In this process the free electrons are not involved. The radiative decay of excited states leads to a loss via radiation, for example

$$O^* \rightarrow O + h\nu(6300\text{Å})$$

1.2.7 Reaction Rates

The rate at which a reaction occurs in the Earth's atmosphere depends upon the product of the rate coefficient and the concentration of the reactants. The latter tends to change considerably with altitude, temperature and other physical and chemical parameters.

As noted in 1.2.2 the dissociative recombination rate coefficients tend to be inversely proportional to the temperature, i.e. the cooler the electrons, the faster they recombine. Similarly the chemical reaction rates noted in 1.2.3 tend not to increase with increasing temperature. However, the production of the excited states does increase with temperature, and, in the reactions (1.10) to (1.14), the excited state species have far higher rate coefficients than the ground state species. It is the relative slowness of these chemical reactions that prevent the F region ionisation decaying rapidly after sunset as happens in the E region. On the other hand, an increase in the NO^+ concentration by the chemical reaction (1.14) can increase the ion and electron depletion through recombination as in equation (1.8). The reaction given in (1.14) is strongly dependent on the vibrational state of the N_2. In particular, the rate for $v = 2$ vibrational state of N_2 is 40 times faster than for $v = 0$ (Hierl *et al.*,1997). The population of excited states depends upon the temperature of the neutrals.

1.3 The Magnetosphere

Within a few Earth radii the Earth's magnetic field is similar to that which would be produced if an enormous magnet were placed close to the Earth's centre. The magnetic axis would make an angle of 11.2° with the Earth's axis and it would penetrate the Earth at the geomagnetic poles 78.8°N, 289.1°E and 78.8°S, 109.1°E (Brekke, 1977). These poles are not the same as the magnetic poles to which a magnetic needle points. They are imaginary points that help to provide a model to describe the Earth's magnetic field. This magnetic field is referred to as the geomagnetic field.

Sometimes the geomagnetic field is used as the reference system rather than the Earth's geographical system. Using geographic spherical polar coordinates with origin at the Earth's centre, the north geomagnetic pole, P, is described using the coordinates $\lambda_p = 78.8°\text{N}$ and $\varphi_p = 289.1°\text{E}$. The geographic coordinates, (λ, φ), used to describe the latitude and longitude for a place on the Earth can be related to the geomagnetic coordinates, (λ_m, φ_m).

Using spherical trigonometry and with reference to Figure 1.1:

$$\sin\lambda_m = \sin\lambda_p \sin\lambda + \cos\lambda_p \cos\lambda \cos(\varphi_p - \varphi), \text{ and}$$

$$\sin\varphi_m = \frac{\cos\lambda}{\cos\lambda_m}\sin(\varphi - \varphi_p)$$

So at Svalbard, with geographical coordinates (78.15°N, 16.05°E) we have:

$$\sin\lambda_m = \sin 78.8° \sin 78.15° + \cos 78.8° \cos 78.15° \cos(289.1° - 16.05°)$$

$$= 0.9622$$

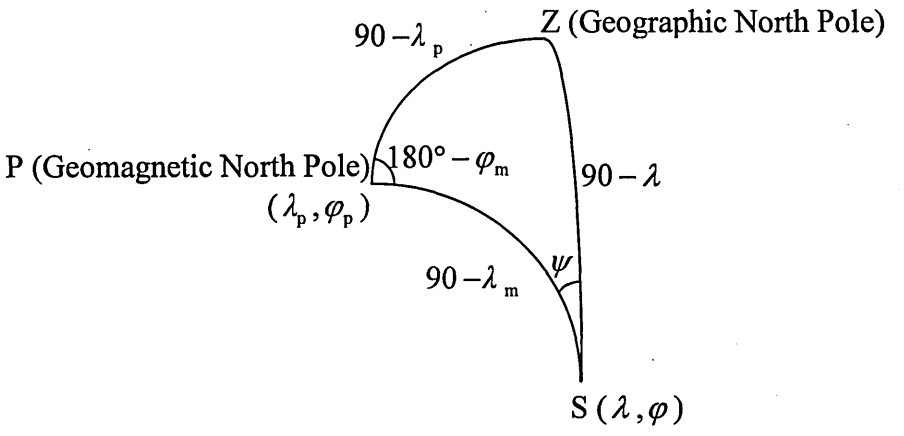

Figure 1.1: To show the relation between the Earth's geographical coordinate system and the geomagnetic coordinate system.

hence,

$$\lambda_m = 74.19°$$

and,

$$\sin\varphi_m = \frac{\cos 78.15°}{\cos 74.19°}\sin(16.05° - 289.1°)$$

$$= 0.7527$$

hence,

$$\varphi_m = 180° - 48.82° = 131.18°$$

So Svalbard has geomagnetic coordinates (74.19°, 131.18°).

The magnetic dipole declination, ψ, is the angle between the direction of the two poles and is measured in the positive eastward direction from the geographic north. From the spherical triangle,

$$\sin\psi = -\frac{\cos\lambda_p}{\cos\lambda_m}\sin(\varphi - \varphi_p)$$

So at Svalbard,

$$\sin\psi = \frac{\cos 78.7°}{\cos 74.19°}\sin(16.05° - 289.1°) = 0.7119$$

$$\psi = 45.39°$$

Hence the magnetic dipole declination is – 45.39°, which is in the westward direction.

Geomagnetic time is sometimes used in auroral studies. Geomagnetic noon is when the Sun is on the geomagnetic meridian of the station, and geomagnetic midnight occurs when the Sun is on the opposite meridian. At the observing site, Svalbard, the noon and midnight times therefore occur when the Sun reaches an azimuth of $180° + \psi$ and ψ (since ψ is negative) respectively. In 1 hour the Earth will rotate through 15°, so at Svalbard, the geomagnetic midnight will be

$$2400 - \frac{45.39}{15} = 2400 - 0302 = 2058 \text{ hours.}$$

The magnetic field, **B**, can be measured at ground stations using magnetometers. It is usually given in terms of cylindrical coordinates (*H*, *D*, *Z*). These can be related to the Cartesian coordinate system (*X*, *Y*, *Z*), where the *x*- and *y*-axes points towards geographic north and east respectively and the *z*-axis points towards the Earth's centre. As Svalbard is in the northern hemisphere the *z*-axis will point downwards as shown in Figure 1.2.

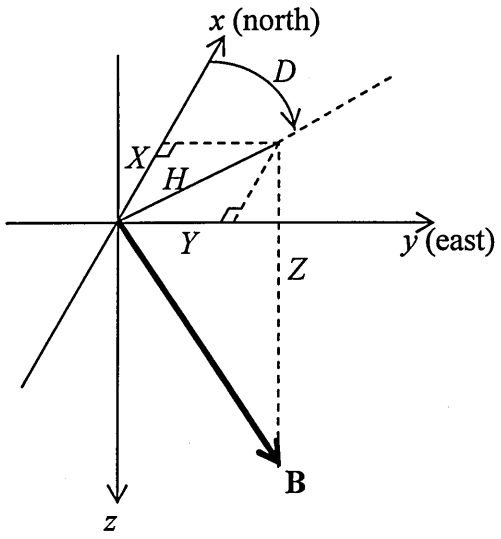

Figure 1.2: To show the relationship between the Cartesian coordinate system, (X, Y, Z), and the cylindrical polar coordinate system, (H, D, Z), used at ground stations to measure the magnetic field, **B**.

In the cylindrical system, H is the component of **B** in the horizontal plane, D is the declination, the deviation with respect to true north and Z is the component of the field along the z-axis as in the Cartesian system. The cylindrical coordinate system is related to the Cartesian coordinate system as follows:

$$H = \sqrt{X^2 + Y^2}$$

$$\tan D = \frac{Y}{X}$$

$$Z = Z$$

The Earth's magnetic field can affect the motion of the ionised particles so changing the electric currents and the movement of the plasma in the ionosphere. In the high regions where the atmosphere is more sparse and the degree of concentration of ions greater the behaviour is dominated by the geomagnetic field. This region is referred to as the magnetosphere. There is no clear distinction between the area where the ionosphere stops and the magnetosphere starts.

As we move further away from the Earth's surface, there is a clearly identifiable boundary between the magnetosphere and the solar wind. This boundary is called the magnetopause. Any activity at the magnetopause determines much of the behaviour of the magnetosphere and the ionosphere at high latitudes. The magnetopause occurs at about 10 Earth-radii from the Earth in the direction of the sun.

The solar wind is mainly due to the solar coronal plasma expanding into interplanetary space. It consists of energetic particles and the 'frozen-in' interplanetary magnetic field. Typically, at a distance of 1 astronomical unit from the sun, the solar wind travels at approximately 400km/sec, though this can increase to about 1000 km/sec during disturbed periods (Davis, 1990). When the solar wind reaches the Earth, travelling at supersonic speeds it distorts the Earth's magnetic field. On the dayside it compresses the Earth's magnetic field, whilst on the nightside it pulls the Earth's geomagnetic field out in a long tail. This tail is called the magnetotail and can extend to approximately 100 Earth radii.

Chapter 2

Techniques and Instruments

2.1 Scatter Techniques

Several types of scatter radar are used to probe the ionosphere. Many use electromagnetic waves which propagate at the speed of light, $c = 3 \times 10^8 \, \mathrm{m\,s^{-1}}$ in vacuo. 'Coherent' and 'incoherent' are terms used to describe the types of scatter involved.

2.1.1 Coherent scatter

Coherent scatter occurs when the transmitted wave reaches a layer in the atmosphere for which its frequency is the critical frequency and, although the medium is stable, there are large-scale changes in conditions, such as a significant wave travelling in the direction of observation. The transmitted wave will then be reflected. This situation is

analogous to that in which a plane wave travels across a ripple tank and on reaching the opposite side is reflected back along the same direction. The scattered signal will then be enhanced in a manner which corresponds to constructive interference, where the amplitudes of the waves may be added coherently.

2.1.2 Incoherent scatter

Incoherent scatter occurs when the electrons are free to move independently. This is analogous to a plane wave travelling across a ripple tank in which there are many randomly positioned minute pins. The main wave will travel across the tank unaffected, but at each pin a tiny circular ripple will be produced. The overall effect on the surface of the tank will hardly be noticeable, but a very small wave will result at the observer end. In this case the observing wavelength needs to be shorter than the smallest irregularities in the electron density in the ionosphere. If the scatter is really incoherent then the random motion of the electrons will scatter signals with unrelated phases and amplitudes so that at the receiver it is the signal powers that must be added.

Results obtained in the early 60's (Dougherty and Farley, 1960; Fejer, 1960; Salpeter, 1960; Hagfors, 1961; Rosenbluth and Rostoker, 1962) showed that it was not appropriate to consider 'free' electrons in the ionosphere because of the electrostatic forces between the electrons and the ions. The ions are attracted to each of the electrons since they are oppositely charged. Meanwhile the ions are dispersed because of their thermal velocities and mutual repulsion. As a result the ions form a mutual shield around each electron. The motion of the electron is hence controlled by the ions. The extent to which the ions control the electron motion depends on the radar wavelength and the Debye length, λ_D, where

$$\lambda_D = 69\sqrt{\frac{T_e}{N_e}} \text{ m}$$

λ_D varies from ~0.3 cm at the F region peak (~250 km) to ~6 cm in the lower E region (~90 km)or at much greater heights (~2000 km) (Beynon and Williams,1978).

If the radar wavelength is $<<\lambda_D$, then we have scattering by 'free' electrons.

However, when the radar wavelength is $>>\lambda_D$, then the motion is controlled by the ions. Waves are set up in the ionosphere as a result of the electrostatic coupling and the thermal motion of the electrons. These waves are known as 'ion-acoustic' and 'electron-acoustic' waves or 'plasma' waves. When the ion or electron density increases locally, as a result of these waves, a net electric charge occurs and electrostatic forces must be taken into account in addition to the forces due to the pressure gradients. The observed scattered signal is a result of these changes in the electron density. Since it is usual for the radar wavelength to be $>>\lambda_D$, then the process used is not really that of incoherent scatter at all, but rather 'quasi-coherent' scattering by thermally induced electron-ion acoustic waves. The process, however, is still universally referred to as 'incoherent scatter'.

2.2 Incoherent Scatter Radars

Bowles (1958) made the first observations of coherently scattered signals in 1958, using a transmitted power of 6 MW at 41 MHz (Rishbeth and Williams, 1985). It became clear that using such a technique enabled scientists to measure the electron density well above the F2 region peak.

The first incoherent scatter radars:—

Jicamara, Peru

Arecibo, Puerto Rico, and

Millstone Hill

were constructed in 1960-61. By 1989 there were only five such radars (Hargreaves, 1995)

The European Incoherent Scatter radar (EISCAT) in Northern Scandinavia had intended to start its operations in 1978, but its UHF transmitter actually commenced operation in 1981, whilst the VHF transmitter was installed in 1984 and started to give results in 1985 (Rishbeth and Williams, 1985). At this time, EISCAT was supported by the science research councils of Finland, France, Germany, Norway, Sweden and Britain (Williams, 1985). In 1996, Japan joined the EISCAT Scientific Association.

Incoherent scatter radars are of two types:

1. **Monostatic**, where the transmitter and receiver are at the same site and usually use the same antenna. These radars must use pulsed signals which are 'gated' to select the ranges at which measurements are made.

2. **Multistatic**, which has separate transmitter and receivers. These radars can use continuous waves.

These are capable of observing both sides of the F region peak simultaneously. They also produce a narrow beam, because the antenna has to be large relative to the radio wavelength, and so achieve better spatial resolution.

Their main disadvantage is that they have to receive a very weak signal which in turn requires a high power transmitter, a large antenna, the most sensitive of receivers and

sophisticated data processing techniques. This adds up to a major facility and a considerable expense. Also, as we will see later, the return signals can be disrupted frequently by metal objects such as satellites and their debris.

2.2.1 EISCAT Mainland Radars

EISCAT incorporates both the monostatic and multistatic types of radar. There are two monostatic radars (one UHF and one VHF) located at Tromsø in Northern Norway. The signal returned from the UHF signal can also be received at the sites in Kiruna, Sweden and Sodankylä, Finland. Precise timing between the three sites enables the ion velocity vector to be determined at points in the ionosphere which are accessible to all three antennae. Common Programmes (CPs) and Special Programmes (SPs) are run from the mainland site. CP data is available to all members of the community, whereas SP data is normally only available to those members who requested the experiment unless special permissions are granted.

2.2.2 EISCAT Svalbard Radar (ESR)

A new radar near Longyearbyen on Svalbard (EISCAT Svalbard Radar — ESR) was officially inaugurated on 22nd August 1996. Unlike the previous incoherent scatter radars the system design was changed so as to make use of commercially produced TV transmitter hardware. This reduced the design risk, lead times and cost to a minimum. It has extended the area being observed to higher latitudes and provides information on the cusp region.

The site is at the geographical location 78° 09′N, 16° 03′E. This corresponds to a geomagnetic inclination of 82° 06′N and an invariant latitude of 75° 18′N. It has a UHF transmitter with an operating frequency of 500 MHz. Wannberg *et al.* (1997) give much of the technical detail of the design of this radar system.

The radar's first experiment, GUP0, was attempted on 16th March 1996. The radar was not used much during this year, however, its usage has gradually increased and many hours worth of data now exist.

There were some problems with clutter, i.e. data which did not analyse properly, which could not be removed from the data. This was a particular problem in the early gates of the background signal. There were also some hardware problems. A new dish and the implementation of a pulse-to-pulse subtraction technique have been successful in reducing the clutter from the data. As a result the early experiments (GUP0 and GUP1) have now been replaced with GUP3 experiments.

The raw ESR data sets were approximately 42 times larger than the corresponding CP-1 data sets from the mainland site. This is due to the ESR data being recorded in more detail even though most of it is not used.

2.3 GUP3 Experiment

The earliest GUP3, Common Programme data which is available is from 25th August 1998.

A description of the GUP3 experiment can be found on the website:

http://www.eiscat.rl.ac.uk/~ian/gup3desc.htm

A brief summary follows.

The GUP3 experiment uses a 640 μsec long pulse (LP) followed by a 16×40 μsec (i.e. 640 μsec) alternating code (AC) from the strong condition code set of 32 randomised codes. The backgrounds are measured in the same frequencies and receiver channels as the signals on alternating inter-pulse periods, IPPs, (on average 1 IPP = 6510 μsec). This requires four frequencies, F1, F2, F3 and F4. At the 7.5 MHz input frequency level these frequencies correspond to the values

F1 = 7.031250 MHz
F2 = 7.265625 MHz
F3 = 7.500000 MHz
F4 = 7.734375 MHz

These rather unusual fixed values are used as they can be represented exactly, without rounding errors, in the internal binary arithmetic of both the transmitter and the receiver side numeric oscillators.

During the first IPP, the first long pulse (LP1) is transmitted at F1, then the first alternating code (AC1) is transmitted at F2, followed by a period in which the signal is received at F1 and F2 whilst the background is received at F3 and F4. Similarly, during the second IPP, the second long pulse (LP2) is transmitted and received at F3, the second alternating code (AC2) is transmitted and received at F4 and the background is received at F1 and F2.

Clutter cancellation is performed on the alternating code data. Since this requires that all 32 codes are sent twice on both frequencies then the full transmission cycle

contains $2\times(2\times32)=128$ IPPs.

The data is integrated over 10 sec intervals. This requires 12 cycles (9999360 μsec) along with 640 μsec idle time at the end of each interval.

2.4 Theory of Spectra

Originally it was believed that the radar beam would be scattered by the individual electrons. Such electrons would have thermal velocities whose component parallel to the beam would have a Gaussian distribution. The resulting Doppler shifts in the return signal would cause a wide spread in the frequencies observed as shown in Figure 2.1.

It is normal, with the frequency of signal used by ESR, for the radar wavelength to be much greater than the Debye length. As a result we should not consider the scattering to be from 'free' electrons since their movement is strongly controlled by the surrounding ions. Any random thermal motion of the electrons will cause waves to be created in the plasma. The changes in the electron density, which result from these waves, give rise to the observed scattered signals. The theory tells us that these waves have a wide range of wavelengths and are propagated in all directions. However, it is those which are of wavelength equal to ½λ, where λ is the wavelength of the original signal, and are travelling upwards and downwards along the direction of the beam which will lead to the strong 'quasi-coherent' scattered signal that is received at the ground. A wave travelling upwards with velocity V will experience a negative Doppler shift of $-\frac{2V}{\lambda}$ and a wave travelling downwards with a velocity V will experience a positive Doppler shift of $\frac{2V}{\lambda}$.

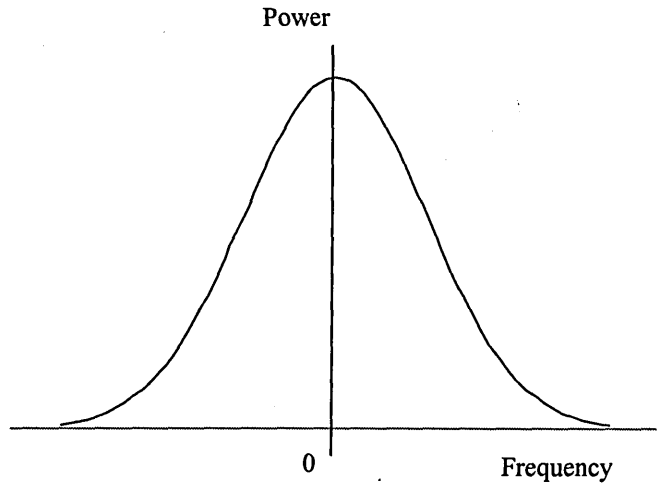

Figure 2.1: Diagram to show the expected spread in the returned frequencies, due to Doppler shifts, if the radar beam were scattered by the individual electrons.

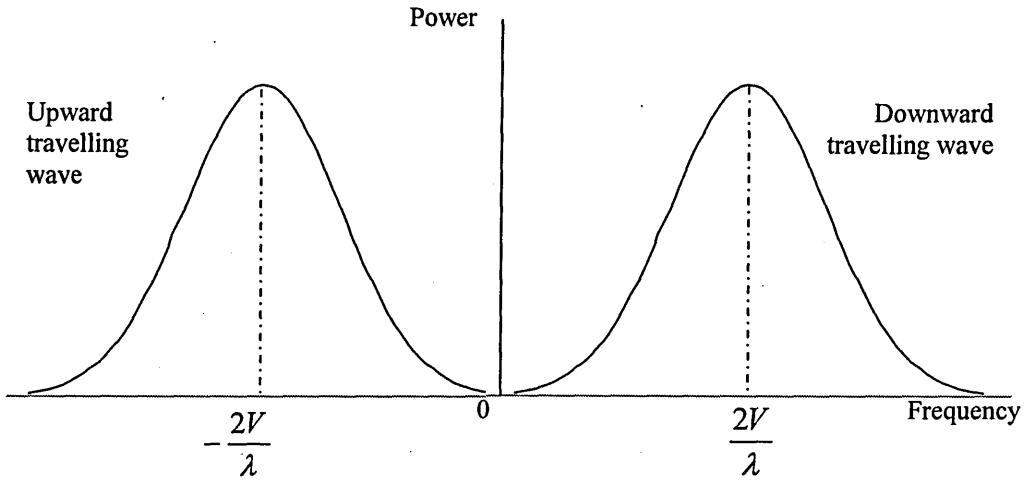

Figure 2.2: Diagram to show the expected spread in the returned frequencies, due to Doppler shifts, if the radar beam were scattered not by "free" electrons, but by the ions surrounding the electrons.

The frequency shift caused by the Doppler effect, $F(\Lambda)$, can therefore be expressed as

$$F(\Lambda) = \pm\frac{2V}{\lambda},$$

where $V =$ the velocity of the ion-acoustic wave, and

$\Lambda = \frac{1}{2}\lambda =$ the wavelength of the ion-acoustic wave.

In the direction of the radar beam we have:

$$\text{energy} = \tfrac{1}{2}mV^2 = \tfrac{1}{2}k(T_i + T_e)$$

But, $m = m_i + m_e \approx m_i$, since $m_i >> m_e$,

where $m_i =$ the rest mass of the ion, and

k, T_i, T_e, m_e and m are as previously defined.

So, $$V^2 = \frac{k(T_i + T_e)}{m_i}$$

Hence, $$F(\Lambda) = \pm\frac{2}{\lambda}\sqrt{\frac{k}{m_i}(T_i + T_e)} = \pm\frac{2}{\lambda}\sqrt{\frac{kT_i}{m_i}\left(1 + \frac{T_e}{T_i}\right)}$$

The spectral lines have little resemblance to those shown in Figure 2.2 since they are greatly broadened as a result of Landau damping (Ratcliffe, 1972). This is when the thermal velocity of the charged particles in the plasma is similar to the phase velocity of the wave. Those particles with a slightly lower velocity than the phase velocity of the wave will be accelerated by the wave and so they will take energy from the wave. As a result the wave will be damped. If the particles are travelling at the same velocity as the phase velocity of the wave, they will simply travel along with the wave with no energy exchange occurring. If, on the other hand, the particles have a slightly higher

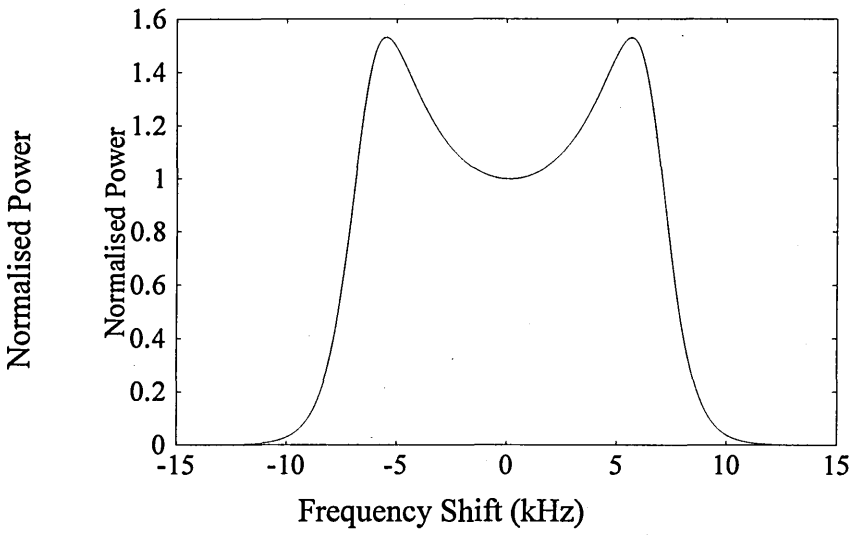

Figure 2.3 Diagram of theoretical spectrum obtained using the 'iaspec' program with radio frequency = 500 MHz, electron temperature = 2500 K, electron density = 1.5e11 m^{-3}, ion temperature = 1500 K.

velocity than the phase velocity of the wave then they will lose some of their energy and the wave would gain energy. Typically, there are more ions travelling slightly slower rather than slightly faster than the wave. Hence the ion-acoustic wave is attenuated and the spectral lines are broadened. This gives rise to the characteristic 'double-humped' ion spectrum. A typical theoretical spectrum obtained using the 'iaspec' program (Sedgemore-Schulthess and St-Maurice, 2001; Sedgemore-Schulthess, 2002), see Appendix A, is shown in Figure 2.3.

The electron-acoustic or plasma waves are generally travelling much faster than the thermal velocities of the majority of the electrons. There will therefore be very little attenuation. They lead to positive and negative frequency shifts which are almost equal to the plasma frequency. This can be as large as 10 MHz. There is almost no broadening of the plasma lines because the electron speeds are too small.

The typical incoherent-scatter spectrum will therefore consist of a double-humped ion spectrum and the plasma lines distributed either side of the transmitted frequency with the ion spectrum close to the transmitted frequency and the two plasma lines at a much greater distance from it.

2.5 Measurements Obtained

Provided the scattered signal is measured with adequate signal-to-noise ratio the following parameters can be determined directly:

the electron density, N_e,

the electron and ion temperature ratio, T_e/T_i,

the ion temperature and ion mass ratio, T_i/m_i

the ion mass, m_i, and

the plasma velocity, V_p.

From these measured quantities it is possible to estimate many other parameters indirectly:

the electric field, **E**,

the ionospheric (Hall and Pedersen) conductivities, σ_1 and σ_2,

the neutral wind velocity,

the neutral air temperature, T_n, and

the downward flux of heat from the exosphere.

Some of these parameters are dependent upon others whilst in some cases values of the parameters can only be determined by making assumptions.

2.5.1 Electron Density

The electron density can be determined using a knowledge of the total power returned from the scattering region. This total scattered power, P_R, corresponds to the area under the curve of the spectrum.

$$P_R \propto \frac{N_e \sigma_e}{\left(1+\alpha^2+{}^{T_e}/_{T_i}\right)\left(1+\alpha^2\right)} \approx \frac{N_e \sigma_e}{1+{}^{T_e}/_{T_i}},$$

where σ_e = the scattering cross section of an electron, and

$$\alpha = {}^{4\pi\lambda_D}/_{\lambda}$$

Alternatively, it may be obtained from the frequency offset of the plasma lines, or from the Faraday Effect if the polarisation can be measured. This latter method allows a value to be obtained for the electron density as a result of noticing the distance travelled through the ionosphere for complete rotations of the circularly polarised wave (Ratcliffe, 1972). This method is not used often as it is not exact and the derived values of the electron content can be as much as 10 – 20% in error.

2.5.2 Electron and Ion Temperature Ratio

The ratio of the electron and ion temperatures, ${}^{T_e}/_{T_i}$, is obtained from the ratio of the peaks to the dip in the spectrum.

The width of the spectrum is proportional to the temperature of the ions.

2.5.3 The Ion Temperature and Ion Mass Ratio

The ratio of the ion temperature to the ion mass, T_i/m_i, can be obtained from the separation of the two peaks of the spectrum. If a value for m_i can be assumed, it is then possible to determine the values of T_e and T_i.

2.5.4 The Ion Mass

Although the value of m_i can be reliably estimated for certain heights, this is not the case for all heights. Fortunately the spectrum of the scattered signal from a plasma containing two different ion species is not the same as that corresponding to the mean ion mass. When there are two ion species present a new family of spectra can be derived. It is thus possible to observe the transition between different ion species.

2.5.5 The Plasma Velocity

If the plasma is moving then the spectrum will receive a Doppler shift. A measure of this shift will give the component of the plasma velocity in the 'mirror' direction. In the lower regions of the ionosphere this drift will be the same as the motion of the neutral air. In the F region, the horizontal plasma drift is due to an electric field.

Chapter 3

Background Theory

3.1 Background

The theory indicates that the spectra obtained should be double-humped where the peaks are approximately equally shifted in opposite directions as for a near-Maxwellian plasma for which the electron temperature is greater than the ion temperature. However this is not true for the lower altitudes (below about 110 km) which have a high ion-neutral collision frequency and where intense high latitude electric fields tend not to give Maxwellian velocity distributions. Both these situations result in the spectra having a prominent central peak. In practice many other variations are obtained. In particular, there are identified times when one or both of the peaks are enhanced. Such occurrences are referred to as enhanced spectra.

A copy of the program 'iaspec', was obtained from Francis Sedgemore-Schulthess (2002). This program can be used to compute theoretical ion-acoustic spectra for

drifting electrons and two types of non-drifting ions. A typical output giving a standard 2-humped spectrum was shown in Chapter 2.

Examples are given in Figures 3.1 and 3.2 of the output from the 'iaspec' program when different values of the parallel drift velocity were input. Figure 3.1 shows the left shoulder is enhanced when the parallel drift velocity is negative, and Figure 3.2 shows it is the right shoulder which is enhanced when the parallel drift velocity is positive. Further examples are given in Sedgemore-Schulthess and St-Maurice [2001].

When the electron temperature is increased, but the ion temperature kept constant (so T_e/T_i increases) the 'iaspec' program shows that a situation occurs in which both shoulders of the spectra are enhanced as shown in Figure 3.3.

A study of the 'iaspec' program shows that these are the only situations which will cause the spectra to become anomalous using this model. In Rietveld *et al.* (1991), it is noted that this program illustrates how the enhancement of one of the ion acoustic peaks can only be produced by a displacement in the thermal electron distribution function and not with large fluxes of a small number of energetic electrons. In this same paper the following three points are made:

1. If the enhancement is in the positive Doppler shifted frequencies then the thermal electrons are travelling toward the observer, i.e. there is a downward field-aligned motion of thermal electrons.

2. The larger the electron temperature, the easier it is to destabilise the ion acoustic peaks.

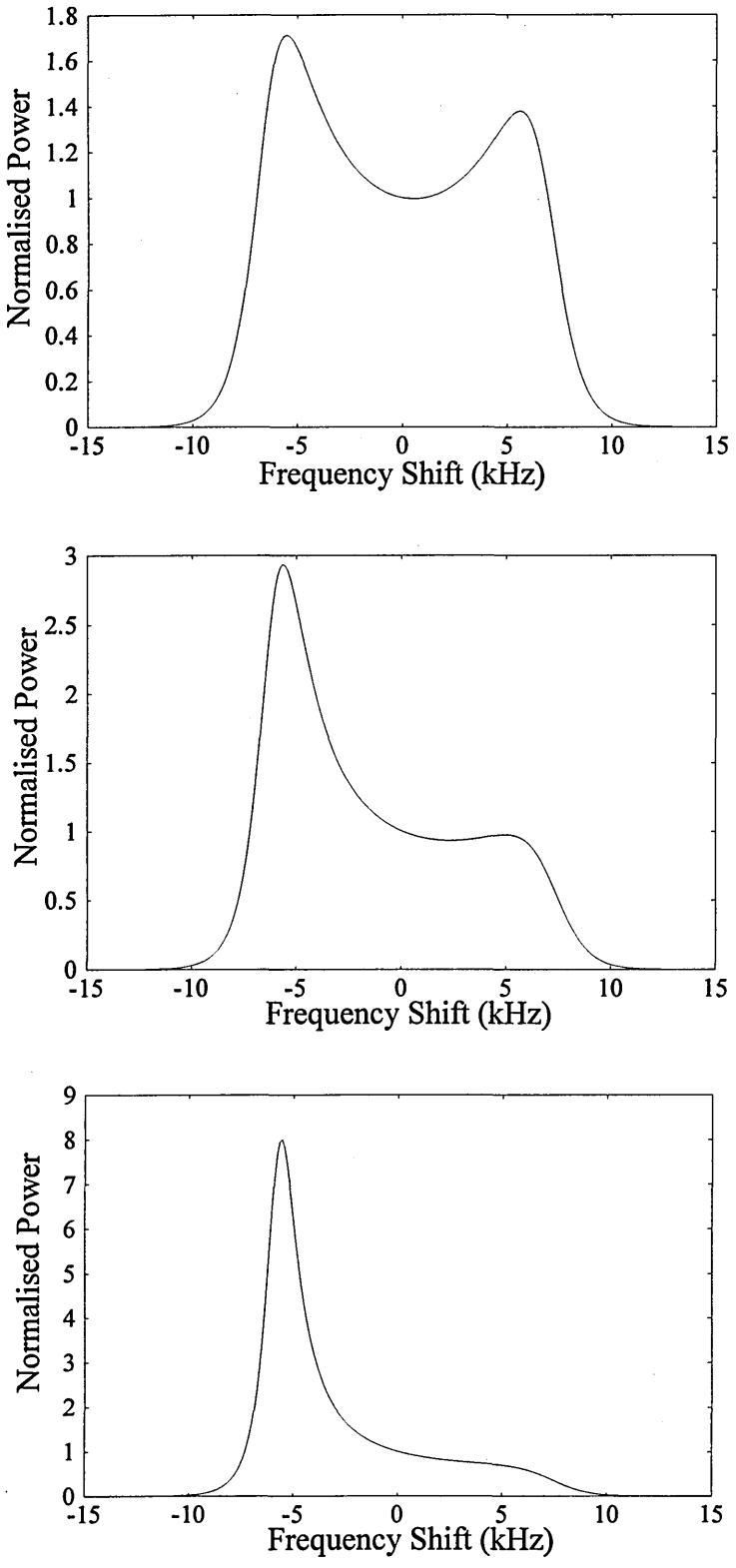

Figure 3.1: Theoretical spectra obtained using the 'iaspec' program with radio frequency = 500 MHz, electron temperature = 2500 K, electron density = 1.5e11 m^{-3}, ion temperature = 1500 K and parallel drift = –10, –50 and –100 km/sec, respectively.

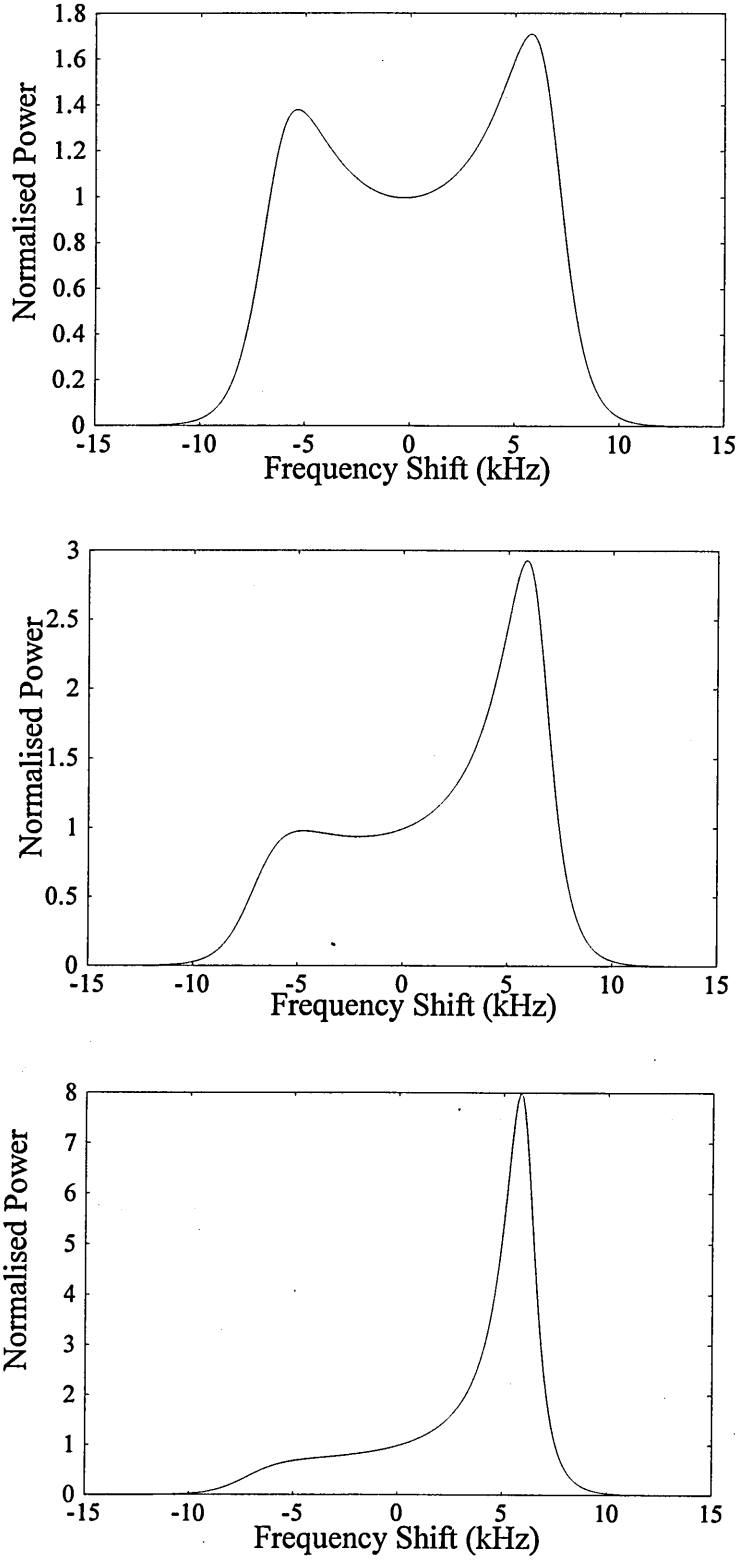

Figure 3.2: Theoretical spectra obtained using the 'iaspec' program with radio frequency = 500 MHz, electron temperature = 2500 K, electron density = 1.5e11 m^{-3}, ion temperature = 1500 K and parallel drift = 10, 50 and 100 km/sec, respectively.

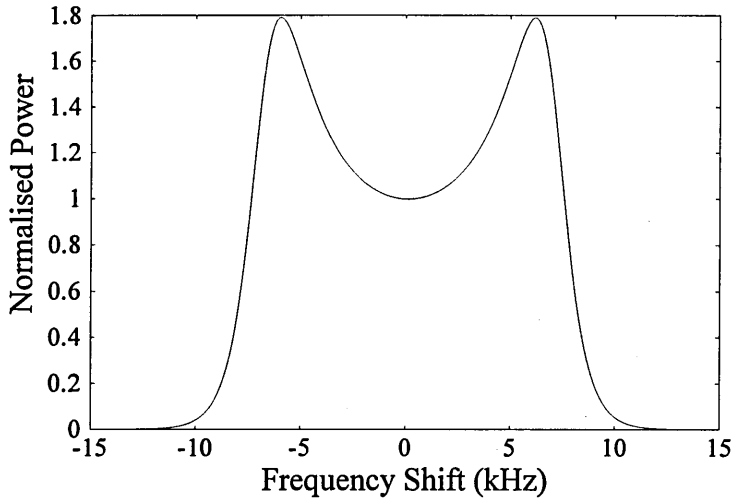

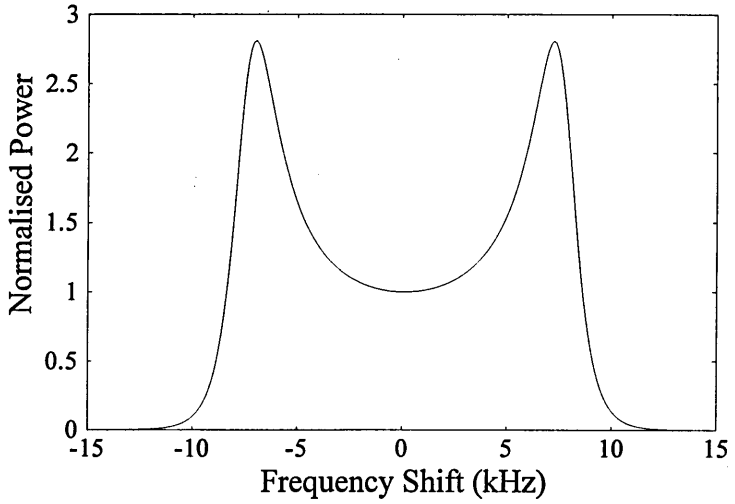

Figure 3.3: Theoretical spectra obtained using the 'iaspec' program with radio frequency = 500 MHz, electron temperature = 3000 K and 4500 K respectively, electron density = 1.5e11 m^{-3}, ion temperature = 1500 K and parallel drift = 0 km/sec.

3. Counterstreams of thermal electrons do not lead to ion line spectra having both the upshifted and the downshifted ion acoustic peaks simultaneously. Hence when both peaks are enhanced simultaneously there is either a temporal feature (a short period of upward moving electrons followed or preceded by another short period of downward moving electrons) or an occurrence of spatial structures which are very narrow in latitude.

3.2 Millstone Hill Radar

Many strong enhancements have been reported in high-latitude radar data since the late 1980's. The first reported instances of naturally enhanced ion acoustic spectra occurring in the topside ionosphere were observed by Foster *et al.* (1988), using the Millstone Hill radar. The Millstone Hill radar (latitude 42.5° N, longitude 75° W) is ideally positioned for observing the ionospheric trough and any related phenomena. The ionospheric trough is the region in which the electron density is reduced compared to that at higher and lower latitudes.

It had been observed that in the region of the ionospheric trough an unusually large number of echoes were returned from the topside F region. These returns had previously been discarded as echoes resulting from satellites and space debris.

In the cases investigated by Foster *et al.* (1988) the observed spectra were a result of integration of the received signal over 30-second time intervals.

In the first instance, on 23rd July 1983, when the antenna was pointing towards the zenith, there was a clear growth of the downshifted ion-acoustic line as the altitude increased above 800 km.

In the second case, on 9th November 1987 at 05:15 UT, the antenna scanned across an ionospheric trough. The trough was between 50° and 55° latitude (62° to 67° magnetic). On the equatorward edge of the trough, near 48° latitude (61.5° magnetic), an enhanced, downshifted ion acoustic line was observed. On the poleward edge, near 58° latitude (69.5° magnetic), spectral enhancement at the ion acoustic frequency was seen at 495 km and intense backscatter was seen at the ion plasma frequency above 600 km.

It was decided that these observations were unlikely to be caused by satellites since:

1. the enhanced returns continued in a given region with varying intensity for up to 1 hour,

2. the strong backscatter was noted to last for a fraction of the time it would take a satellite to cross the radar beam, and

3. there was no record in the catalogue of space objects (maintained and updated by the M.I.T. Lincoln Laboratory Millstone satellite tracking facility) which could be associated with these strong returns.

Although these topside ionospheric radar observations did not observe the earthward directed current directly they are shown to be consistent with backscatter from a field-aligned current.

Foster *et al.* (1988) suggested that these observations of spectral enhancements at the ion acoustic frequency were indicative of the ion acoustic mode tending towards instability as the altitude increased. The ion acoustic wave is a sound wave which becomes unstable in the presence of field-aligned currents similar to those which are expected in the region of the aurora (Kindel and Kennel, 1971). Foster *et al.* (1988)

observed enhanced backscatter at the plasma frequency in the higher altitudes which was consistent with the unstable growth of the ion acoustic mode when $\frac{T_e}{T_i} >> 1$.

It was thus realised that radar observations clearly provide a powerful diagnostic technique with which to study the occurrence and characteristics of high latitude field-aligned current filaments and the processes associated with them.

3.3 EISCAT VHF (933 MHz) and UHF (224 MHz) Radars

Rietveld *et al.* (1991) reported observations obtained with good altitude resolution from the EISCAT incoherent scatter radar using the UHF (933 MHz) radar at Tromsø. They showed intense, short-lived enhancements of the ion acoustic shoulders in the incoherent scatter spectrum from 138 to 586 km in altitude. These occurred both along the magnetic field-aligned direction and at angles within 15° of this direction. The echoes appeared to be similar to those at 440 MHz reported by Foster *et al.* (1988), but they were seen simultaneously over a height range of at least 400 km with better time (10 sec data intervals) and height resolution.

On 14th February 1990 at 05:16:00 UT a large peak on the upshifted ion acoustic shoulder was clearly visible from 146 km to about 500 km, and an enhanced downshifted peak was visible from 300 to 587 km in the long pulse spectra. The frequency of these enhanced spectra increased smoothly with height. This suggested that the ion temperature was increasing with height. The enhanced spectra were often much weaker and were seen over a more limited region than was the case in this particular example.

Five other data intervals were found on 25th October 1989, from 02:49:30 to 02:50:10 UT, in which a different antenna-scanning pattern was used. Two occurred when the antenna was field-aligned, one when the antenna was vertical (12.5° magnetic) and two when the antenna was at an elevation of 62.9° (14.6° magnetic). When the echoes were along the field line the range extent was small (about three gates) and the enhanced spectra were narrower than for the off-field echoes. If the excitation were being caused by spatially localised field-aligned currents this would explain the smaller range extent.

A statistical survey of the occurrence of these unusual echoes as a function of height showed that they appeared in two preferred regions, below 200 km and above about 300 km. They could vary on a time scale of less than 10 sec, with the longest continuous sequence to be found being 50 sec followed by 10 sec of normal spectra then another 10 sec of enhanced spectra.

Satellites were excluded as an explanation of the data discussed by Rietveld *et al.* (1991) since the enhancement occurred at the ion acoustic frequency and this frequency varied slowly with altitude. Neither the large height range over which the echoes occurred, nor the occasional enhancement of both shoulders could be explained by satellite echoes. Similarly, plasma line contamination could be eliminated.

Though these observations showed some similarities to those of Foster *et al.* (1988):

- intermittency, and
- enhanced ion acoustic shoulders

there were some important differences:

- observations over a greater range of angles,

- some echoes were identified below 300 km altitude,
- change from upshifted to downshifted enhancement at higher altitudes were identified,
- occasionally both shoulders were equally enhanced, and
- the observations were not associated with the ionospheric trough.

Although enhanced spectra are generally considered to be rare, they are more common above 300 km than they are below 200 km. Rietveld *et al.* (1991) suggested that they are associated with disturbed magnetic conditions, auroral electron precipitation, red aurora in the F region and high electron temperatures. Before the occurrence of the echoes the electron to ion temperature ratio was seen to be about 2 to 3.

Because of the excessively high thermal electron fluxes ($\geq$1000 μAm^{-2}) over very short time periods, which theoretically seem to be implied by these conditions, it is tempting to draw an analogy with lightening. It is however suggested that parallel electric fields are created in the ionosphere by field-aligned flows of soft electrons which deposit their energy in the horizontally poor conducting F region. It is these fields which are thought to be responsible for the production of the thermal flows which cause the observations of the enhanced spectra.

Rietveld *et al.* (1991) indicated that more cases needed to be found to see if the characteristic features found in this study were generally true. An increase in data would provide a strong stimulus to further experimental and theoretical work on the instabilities and physics of auroral processes.

On the evening of 11th January 1989 (1525–2128 UT), Collis *et al.* (1991) reported that about 40 intervals of 10 sec averaged spectra with enhanced ion acoustic peaks were observed with the UHF (933 MHz) field-aligned radar. On this same evening a

display of red aurora was seen in Scandinavia. The earliest all-sky image from Kiruna, at 15:00:00 UT (16:00:00 LT), showed a red auroral arc near the northern horizon. The arc moved south and broke up in the region of the radar beam at 15:38:00 UT. This coincided with the time of the most intense anomalous radar returns. A scanning photometer was used to measure the intensity of the 6300Å (red oxygen) emissions. This instrument can only be used during typical night-time conditions, i.e. during the winter months when the sun does not rise in Scandinavia, and the use of the photometer gives no indications of the height at which the emissions occur. Further details of the photometer data are explained later in Chapter 6. Any errors which were introduced as a result of having to assume the altitude of the emissions were reduced by considering the 6300Å emission intensity when the arc passed through the zenith of the photometer data. Using both the all-sky TV and the scanning photometer data it was possible to track the motion of optical features with time. A comparison was then made with the radar data. This showed that active, red aurora were always present when enhanced spectra were detected. In particular, in the time interval from 17:14:10 to 17:14:20 UT the radar spectra showed an enhanced upshifted peak, whilst from 17:15:00 to 17:15:10 UT it showed an enhanced downshifted peak. These enhancements occurred just before and after the time when the arc crossed the field line along which the radar was pointing. This would seem to imply downward streaming electrons equatorward of the maximum luminosity and upward streaming electrons on the poleward side.

In the same paper, Collis *et al.* (1991) also reported that on the evening of 20th February 1990 several periods of enhanced echoes were observed by both the 933 MHz and the 224 MHz radars. The all-sky camera images showed active auroral forms with red upper borders present at around 18:00:00 UT. At the same time the scanning photometer measurements detected a single feature in each scan which allowed the location of the red arc to be tracked. This same time interval, just after 18:00:00 UT coincided with the observation of a 4 min sequence of VHF radar spectra with enhanced ion acoustic shoulders. These enhanced spectra initially appeared at 1350 km altitude and gradually descended to 675 km altitude. Since the radar beam was vertical, this suggested an equatorward motion of a field-aligned

structure. Throughout this period the downshifted peak was always the stronger, although there were occasions when the upshifted peak was simultaneously enhanced. An asymmetry between the ion acoustic peaks has been predicted to occur in the presence of relatively strong differential flows between thermal ions and thermal electrons (Evans, 1969). The side of the spectrum which is enhanced gives an indication of the direction in which the thermal electrons are moving (relative to the ions). An enhancement of the downshifted peak would indicate that the electrons are moving away from the observer, i.e. an upward field-aligned motion of thermal electrons. This means that within a 10-second data dump, upward moving electrons may have been observed for a small part of the time whilst this was either preceded or followed by a short time of downward moving electrons. Alternatively, it may have been that two regions, which were in close proximity, carrying intense currents in opposite directions were being observed. Simultaneous enhancements of both shoulders of the spectra cannot be the result of counterstreams of thermal electrons. When both shoulders were enhanced simultaneously then either a temporal feature or a narrow spatial structure in latitude was being observed as indicated by Rietveld *et al.* (1991).

An analysis of the spectra, carried out by Collis *et al.* (1991), gave estimates of the field-aligned current densities causing the enhancements to be in the range of several mAm^{-2}. However fitting techniques failed for severely distorted spectra when it was presumed that an unstable growth of ion acoustic waves occurred (possibly when the electron drift speed exceeded $0.3\times$ the electron thermal speed).

Collis *et al.* (1991) indicated that all cases of enhanced spectra that had been found, for which optical data exists, were accompanied by red aurora. This is not so surprising since intense fluxes of electrons are known to cause both effects, though the occurrences of enhanced spectra appear to be rare. Field-aligned measurements allow the simultaneous detection of spectra over a large altitude range, so dismissing the possibility of satellite echoes.

Wahlund *et al.* (1992b) identified two different types of ion outflows. A specially designed EISCAT experiment was run for 8 days in September 1989 and February 1990. It used both the UHF radar pointing along the magnetic field and the VHF radar pointing vertically. Large field-aligned ion outflows from the topside ionosphere were observed during auroral activity.

The first type (Type 1) of ion outflow occurred with enhanced and anisotropic ion temperatures, strong perpendicular electric fields and hardly any auroral precipitation (as indicated by the low electron densities below 300 km altitude).

The second type (Type 2) of ion outflow occurred with an extreme enhancement of electron temperature and only a slight increase in ion temperature (the ion temperature perpendicular to the magnetic field line was equal to the ion temperature parallel to it). It was associated with auroral arcs and weak to moderate perpendicular electric field strengths. Unlike the Type 1 outflow the F region did not seem to be displaced upwards in altitude.

Both these types of ion outflow occurred above 500 km altitude. However Type 2 events were more frequent and resulted in larger values of ion fluxes than Type 1 events. It was also noticed that not all auroral arcs were accompanied by ion outflows. An analysis of the ion composition showed it to be mainly O^+, with less than 10% H^+ below 900 km altitude.

Jones *et al.* (1988) found it was possible to explain Type 1 events as bulk plasma outflows with both ions and electrons moving upward. Jones *et al.* (1988, 1990) pointed out that four factors determined the value of the ionospheric plasma velocity parallel to the magnetic field lines in the auroral zone:

1. the meridional component of the neutral wind,
2. the vertical upwelling of the neutral wind,

3. the gradient of the plasma pressure in the topside ionosphere, and
4. gravity.

According to Jones *et al.* (1988), under quiet conditions 1, 2 and 4 combine to drive a low flux (~ 10^{12} $m^{-2}s^{-1}$) of light ions from the top of the ionosphere. A large electric field can cause strong Joule heating of the neutral atmosphere in the upper E region. As a result the plasma is driven upwards with velocity 50–100 ms^{-1}, but this does not explain velocities of 500 ms^{-1}.

Jones *et al.* (1990) indicated that large upward flows of plasma had been observed under trough conditions where large electric fields, strong Joule heating and enhanced ion temperature gradients occurred. The Joule heating is a local phenomenon, due to the enhanced collisions between the neutrals and the ions. This occurs whenever there is a relative velocity between the ion and neutral gases. Such a situation arises at high latitudes where the magnetospheric electric field can rapidly produce ion velocities that greatly exceed the neutral gas velocity (Kelley, 1989). Jones *et al.* (1990) shows that correlation between the strong perpendicular plasma flows, which cause the trough, and the large upward field-aligned velocities were clearly seen on $19^{th}/20^{th}$ May 1987.

With sufficiently strong electric fields the plasma is driven perpendicular to the magnetic field line at a speed which is greater than the ion acoustic speed. Then the resonant charge exchange between oxygen atoms and oxygen ions, and to a lesser extent other collisions, transfer energy to the ion population by frictional heating Buonsanto *et al.* (1997). Thus the ion velocity distribution is changed from a Maxwellian distribution, which is isotropic, to a bi-Maxwellian distribution (Jones *et al.*, 1990) in which there is a temperature anisotropy, or even a toroidal form (Jones *et al.*, 1988, 1990), which is 3-dimensional and also indicates anisotropy. A review of such distributions is recorded by St-Maurice and Schunk (1979). Once the ion velocity distribution is anisotropic the plasma becomes subject to both a force resulting from the divergence of the magnetic field lines with increasing height and

the enhancement in the upward pressure gradient from the increase in the ion temperature parallel to the magnetic field line.

Jones *et al.* (1988) concluded that in addition to a strong electric field, a soft particle precipitation (<1 keV) was needed to create enough conductivity in the upper E region for intense Joule heating. This was indicated by an increased ionisation (~150 km) at 21:00:00 UT on 6th May 1987 and an equally sharp cut-off at 21:48:00 UT. Frictional heating is much greater if the neutral velocity is in the opposite direction to the plasma velocity. These conditions occur in the region of the Harang discontinuity, which is that part of the auroral oval around the midnight sector where an upward field-aligned current is sandwiched between two downward ones.

The Type 2 events observed by Wahlund *et al.* (1993), however, seemed to be related to field-aligned currents with the bulk ion population moving upward and the bulk electron population moving downward.

During short intervals of auroral precipitation and Type 2 ion outflows naturally enhanced ion acoustic spectral lines similar to those observed by Foster *et al.* (1988) and Rietveld *et al.* (1991) were observed. These were not included in the analysis carried out by Wahlund *et al.* (1992b) which was over 60 sec time intervals.

According to Wahlund *et al.* (1992b), further analysis of naturally enhanced ion lines, with shorter integration periods than 60 sec was needed in order to reveal the importance of plasma turbulence with respect to the causes of observed ion outflows. It was stated that the exact mechanism causing the ion outflow was not yet understood, but more than thermal expansion was certainly required.

Wahlund *et al.* (1993), using EISCAT data, presented some observations of high

latitude topside ionospheric electron temperature enhancements during auroral active conditions. At an altitude of about 200 km they showed the enhancement of the electron temperature to be associated with the electron density enhancement which could be produced by soft energy electron precipitation of a few hundred eV. In addition they presented simultaneous observations of ion acoustic turbulence in the form of enhanced spectral ion-line shoulders of the otherwise incoherent scatter radar return signal. It is suggested that these observations are unlikely to be a result of the current-driven instability model previously proposed by Collis *et al.* (1991) and other authors, who unlike Wahlund *et al.* (1992a, 1993), were forced to infer unrealistically high field-aligned current densities (~1 mAm^{-2}). Instead it is indicated that such observations could be interpreted as being produced by an ion-ion two-stream instability, which arises as the result of a relative drift between two ion populations.

Wahlund *et al.* (1993) concluded that the energy dissipation into the background plasma largely occurred through Joule heating as a result of the simultaneous presence of ion acoustic turbulence and field-aligned currents. This was a major contributor for the large electron temperature enhancements observed in the auroral active topside ionosphere.

Wahlund *et al.* (1992a) concluded an ion-ion two-stream instability could explain the observed enhanced ion acoustic lines. However some caution was needed, since:

- the fit was not unique, and
- non linear terms may become increasingly important and a turbulence description was needed.

Forme (1993) suggested that the enhanced ion acoustic fluctuations observed in the upper ionosphere could be due to the Langmuir wave decay. A possible theory for the production of Langmuir waves is given by Cairns (1987). Forme (1993) indicates that a high energy electron precipitation is not able to destabilise the ion-acoustic waves

directly, as the energetic electrons are too few in number to affect the velocity distributions of the ions and electrons near the ion thermal speeds. However, streaming electrons with energies of 10–500 eV can stimulate large amplitude Langmuir oscillations near the electron plasma frequency. As these Langmuir waves decay they produce a backscattered Langmuir wave and an ion acoustic wave. A quantitative explanation of this process is given in Chen (1984). However the mechanism explained by Forme (1993) can only excite downgoing ion waves.

A further study by Forme (1999) which modelled the decay of the beam-generated Langmuir waves into ion acoustic waves using the wave kinetic equations within the framework of weak turbulence approximation showed that the parametric decay of such Langmuir waves could lead to up-going ion acoustic waves, propagating separately or simultaneously.

Forme *et al.* (1995) indicated that two types of mechanisms may exist for the origin of the enhanced ion acoustic lines in the upper ionosphere since ion outflows were not always observed when the instability occurred. Whilst Forme and Fontaine (1999) indicated that the spectral asymmetry and intensity of the received signal in a region of ion acoustic turbulence could not be resolved by the standard analysis procedure and indeed often caused its failure.

One case has been reported by Cabrit and Opgenoorth (1996) where the UHF and VHF radars were looking in the same direction. At the two frequencies observed there was a large difference between the backscattered powers. As a result the authors ruled out the possibility of large relative drifts between different ion populations. They suggest that the volume covered by the radar beam may not be completely filled by the scattering irregularities, i.e. the width of these discrete scattering structures may be smaller than that of the radar beam. The small perpendicular electric field magnitudes which had been reported earlier may be the result of time and spatial averaging.

3.4 EISCAT Svalbard Radar

More recently, examples of naturally enhanced ion acoustic lines have been reported using the data from the EISCAT Svalbard Radar (ESR).

Buchert *et al.* (1999) discussed such an event which showed naturally enhanced ion acoustic lines in the GUP0 experiment on 15th July 1997. During this event, when the received power reached a maximum, a significant difference was noted in the scattered power received in two channels which were separated by only 2 MHz. Physical explanations for the observed frequency-dependence of the power led the authors to the conclusion that the ion acoustic level was strongly dependent upon the wave number, k. This in turn led them to conclude that of the previously suggested models the only one which agrees with these observations is that of the parametric decay of the Langmuir wave suggested by Forme (1993).

The second report of observed enhanced incoherent scatter spectra was by Sedgemore-Schulthess *et al.* (1999). In this paper the enhanced spectra which occurred were seen in the GUP0 data on 24th January 1998 between 07:00:30 and 07:00:50 UT. They are from the dayside cusp/cleft region and are shown to have been observed around the time at which the meridian scanning photometer data showed a series of poleward moving auroral transients. It was also noticed that at this time a narrow-angle TV imager designed for high-resolution optical measurements of auroral phenomena showed there to be considerable change in the aurora on timescales shorter than the 10-second radar integration period. This latter point could explain the observation of spectra with both ion lines enhanced simultaneously. The bright patches of luminosity, showing small-scale auroral forms of order 100 m and less in width, which are seen in the narrow-angle images indicate that there was precipitation both on the field lines probed by the radar and on those adjacent to the beam. Sedgemore-Schulthess *et al.* (1999) assumed a current-driven instability model, with plasma turbulence due to current densities of the order of 1 mAm^{-2}. They explain that

they were able to show that large-magnitude filamentary field-aligned currents can exist in the ionosphere in response to plasma velocity shears associated with magnetic reconnection. Additionally, they indicate that the energetic auroral precipitation can further constrain the width of these current layers.

Forme *et al.* (2001) conclude that the events of naturally enhanced ion acoustic lines which they considered on 6th July 1998 between 07:00:00 and 11:00:00 UT show similar features to those studied previously. Their study confirmed the initial findings that:

1. the naturally enhanced ion acoustic lines sometimes show asymmetric power profiles, and
2. the amplitude enhancement of upgoing and downgoing ion acoustic waves occurs at different altitudes and different power levels.

The observed facts were modelled using the parametric decay of beam driven Langmuir waves, as proposed by Forme (1993), in an inhomogeneous medium. The underlying theory for this process can be found in Fejer (1979). The model shows that the power radiated by enhanced spectra does vary with the wavelength and the power difference between two wavelengths received by the ESR varies with the altitude, typically being a few kilometres apart.

However, the study also indicates that most of the time the power differences are within the noise level and that a study of the wavelength dependence of the naturally enhanced ion acoustic lines will require a large statistical database as well as experimental modes using a wider frequency spacing between channels.

In a more recent study Grydeland *et al.* (2003) shows evidence of filamented structures in the auroral ionosphere observed through enhanced radar echoes produced by plasma instabilities in the filaments. Using an interferometric technique has enabled the confirmation of the existence of filamentary structures. These structures

have been found to be of the order of 100 km long, aligned with the Earth's magnetic field and having scale sizes in the perpendicular direction of a few hundred metres or less.

Chapter 4

Program Techniques

4.1 Searching for Enhanced Spectra in the Data

Many of the reported cases of enhanced spectra have been found in the EISCAT UHF and VHF mainland radar data, whilst more recent cases have been reported upon in the Svalbard (ESR) data. ESR started to run GUP0 experiments in 1996. The data collected from these experiments were all field-aligned. The number of experiment modes was gradually increased to include GUP1, which included alternating codes, and GUP2, which was optimised for the topside. The first reported observations of enhanced ion acoustic spectra seen in the ESR data were made by Sedgemore-Schulthess *et al.* (1999) using the GUP0 experiment.

When the reported results of the GUP0 experiment were first checked using the real time graphics program, rtg, it was found that the images of the spectra obtained were mirror images of those which appeared in the paper by Sedgemore-Schulthess *et al.* (1999). This aspect of the program was checked and found to be due to an error

relating to the direction of the ion velocity being measured in the opposite sense to that of the radar beam. A correction was made to the program being used so that the spectra obtained were correct. It was then possible to proceed with further investigation of the data.

By August 1998 the GUP3 experiment was being used at the ESR site on Svalbard. This experiment makes use of both plain, long pulses (LP) and alternating codes (AC), which are binary codes based on phase-coded long pulses. The use of two different modulations with overlapping range coverage is important, as it allows the presence of anomalies to be confirmed by comparing the data from the two pulse schemes.The experiment makes use of two long pulse channels, LP1 and LP2, and two channels for alternating code data, AC1 and AC2. In this study, we discuss results from the comparison of the data from LP2 and AC2, although LP1 and AC1 were also checked to ensure that the results are consistent. Much of what follows in this chapter and chapter 5 is my own work, recorded in our paper, Porteous *et al.* (2003). The range covered by the LP2 data is 229.5–859.5 km, whilst that covered by the AC2 data is 228–732 km.

Initially, the data from one of the long pulse channels, LP2, was examined. It soon became clear that checking each file manually was going to be extremely time-consuming. The reported cases when enhanced spectra occurred in the EISCAT UHF and VHF mainland experiments were somewhat infrequent and rarely in two or more consecutive ten-second dumps. Looking at a sample of the data was therefore going to be inadequate since it would be too easy to miss the very cases which we were looking for. It was clearly going to mean checking every ten-second dump of data available. This required an automated search method similar to that used by Rietveld *et al.* (1996) to search the mainland data. In these mainland experiments most of the echoes found by Rietveld's automated search were, in order of frequency, caused by:

1 noisy spectra,
2 satellites,
3 enhanced ion acoustic shoulders, and

4 interference.

Having identified the times of such events a manual search could then be performed on the smaller set of data to identify the enhanced ion acoustic shoulders which occurred as a result of geophysical events.

4.2 The Software

The ESR GUP3 data is studied using a real time graphics program, rtg. The rtg program is a Matlab program which uses the raw ESR GUP3 data as input. A typical rtg plot window output from the program is shown in Figure 4.1.

The left hand panel shows a contour plot of the normalised spectra, whilst the right hand panel shows the same spectra as a stacked plot. The spectra shown in Figure 4.1 are the typical two-humped spectra we would expect to obtain according to the theory of incoherent scatter. The horizontal axis shows the Doppler shift from the transmitted frequency and the vertical axis shows the altitude above the Earth's surface from which the data is received.

Figure 4.1: Typical rtg program output showing, on the left, a contour plot of the normalised spectra and, on the right, the same spectra shown as a stacked plot for the LP2 channel at 10:53:59 UT on 1st December 1999.

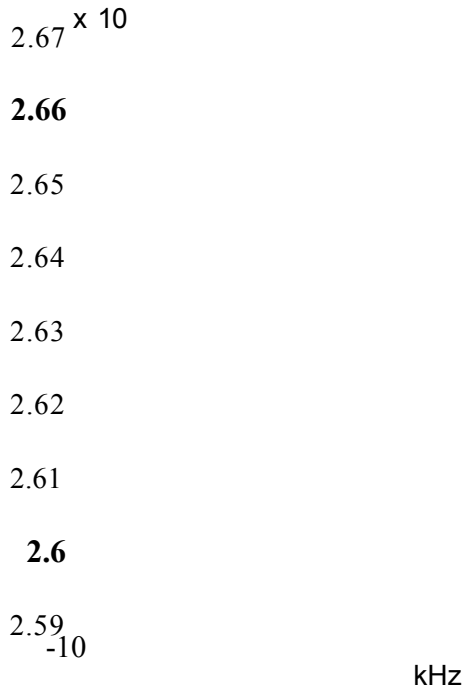

Figure 4.2: A typical spectrum from the right hand panel of the rtg plot window with an indication of the region which was omitted from the search for the secondary peak.

By highlighting one of the spectra shown in the right hand panel of the rtg plot window shown in Figure 4.1 it is possible to view that particular spectrum individually as in Figure 4.2. In this latter figure the horizontal axis again shows the Doppler shift from the transmitted frequency. However, the numbers shown on the vertical axis are related to the position of the spectrum in the stacked plot, i.e. the lower the spectrum in the stack the lower the values of the numbers on the vertical axis. The spectrum shown in Figure 4.2 is the 17^{th} from the bottom of the stack in Figure 4.1.

Although it is possible to obtain an insight into the size of any enhancement of the shoulders by observing the spectra in this manner it would be a tedious process especially as these spectra are normalised within each ten-second dump of data.

As previously stated, the process of checking the data manually for each individual spectrum would be too time consuming, so initially a subroutine, which made use of similar techniques to those used by Rietveld *et al.* (1996), was added to the rtg program.

This additional subroutine was called 'test_asymm', since it involved testing each spectrum for asymmetric shoulders. For each individual spectrum the subroutine first finds the height of the primary peak, P, and its position. It then looks for a secondary peak, S. This is done by finding the maximum height of the spectrum in the region a specified frequency, $\left(w/2\right)$ kHz, from the main peak as shown by the unshaded area in Figure 4.2. The ratio of the heights of the two peaks is then calculated. This ratio is then used to determine whether there is an asymmetry.

Two parameters need to be input at the commencement of the program. The first of these is the required peak width (w kHz). This ensures the two peaks of the spectrum

are $\frac{w}{2}$ kHz apart. After some trial and error testing, the value 5 was used for w so that the two peaks would be separated by at least 2.5 kHz. This was intended to ensure that in the cases when a standard double-humped spectrum was considered the secondary peak identified by the program would indeed be the secondary peak and not just the shoulder of the primary peak. However, when the secondary peak is much lower than the primary one, the program will not identify the secondary peak. Instead, it identifies a point on a shoulder of the primary peak.

The second parameter is the limiting ratio between the peaks. This is the ratio of the height of the lower peak to the higher peak and is therefore a value between 0.0 and 1.0. If the program finds the calculated peak ratio to be less than or equal to the input value the details for that spectrum are output to a text file for later examination. The choice of the value of this second parameter was based on the fact that it needed to be sufficiently smaller than 1.0 to avoid identifying minor variations between the heights of the two peaks, but not so small as to miss any interesting cases.

After some trial runs of the program, it was clear that a suitable value to use for the peak ratio was going to be close to 0.8. A manual inspection of the data did appear to identify the same times as the program on a number of test runs. The cases when a peak ratio of over 0.8 was found in the data were considered at this stage and the spectra found in such situations did not look sufficiently different from the standard spectra to be of interest. It was therefore decided that at this stage the value of 0.82 should be used as the second input parameter. This would ensure that, although some identified spectra would not appear to be significantly enhanced, we would definitely identify all the times at which any anomalous spectra did occur in the data being checked.

After using the program to check for anomalous spectra in several hours of data an up-dated version of the rtg graphics program became available. The up-dated version, rtg3, could be used to observe the data from a more recent experiment, TAU0, as well

as the GUP3 data. Appropriate changes were made to the rtg3 program so that the 'test_asymm' subroutine could be run within this version. However, as the TAU0 experiment uses only AC channels and we have been mainly working with the LP data then we have continued to use only the GUP3 data. On comparing the results from the two versions of the program within the same range interval, then we found that, although the asymmetric spectra appeared at the same times (i.e. in the same ten-second data dumps) in both versions, the ranges at which the most asymmetric spectra occurred were consistently higher in the rtg3 version than they had been in the earlier rtg version. There was an apparent difference in range of about 40 km. Since the data were being averaged over 7 gates each of width 3 km then the spectra were given for ranges which were 21 km apart. As a result a difference in the region of 40 km was not that great. The rtg3 version of the program gave better agreement between the AC and LP data in that the most asymmetric spectra were seen to be at similar ranges within a ten-second data dump for this version, whereas they were seen to be lower for the LP data but similar for the AC data in the rtg version. The rtg3 version of the program was now used to check the data.

The critical value of 0.82 used to identify the asymmetric spectra has been challenged in some quarters. A study was therefore carried out to analyse the full set of peak ratios obtained over a period of four days in December 1999. A total of 10078 ten-second data dumps were included in the study. The distribution of peak ratios is shown in Figure 4.3. Note that the vertical scale is logarithmic. The number of occurrences drops rapidly as the peak ratio decreases from 1.0 to 0.85. It then levels off until 0.75 is reached. At this stage there appears to be another slight drop. The numbers then remain fairly constant until a peak ratio of 0.2 is reached. This suggests that the interesting data corresponds to a peak ratio of between 0.2 and 0.75 and the inclusion of the range from 0.75 to 0.82 has confirmed this view.

960
: 060
980
080
- 9A0
oz/o
: s9 o
090
990
090
9K0
ovo
seo
oeo
930
030
910

vo <ai ^ ro cs

(OIJBJ jo souaxinooo) §0{

4.3 Identification of Enhanced Spectra

During the 10th EISCAT Workshop held in Tokyo in 2001, we presented a poster showing some typical spectra obtained in the July and December 1999 data. As a result, we followed up the suggestion, which was made whilst at this event, that it might be worthwhile looking at the power profiles as well as the spectra.

The situations when the rtg3 program identified anomalous spectra in the data for 1st December 1999 were studied manually. The data set consists of 1011 ten-second dumps recorded between 10:11:30 UT and 13:00:00 UT. The automated routine described above is used to examine the data from the LP2 long-pulse channel. The times at which anomalous spectra are identified by the program are recorded for subsequent manual examination. In some cases, it transpires that the spectra identified as being anomalous contain essentially no backscattered signal and any such noisy spectra are eliminated. This leaves a number of spectra where the program suggests the presence of a satellite. Typical enhanced spectra from such a case are shown in Figure 4.4(a).

In this set of over 2 hours of data there were 40 occurrences of enhanced spectra. The power profiles of each of these situations were considered as a means of distinguishing between cases of naturally enhanced spectra and probable satellites.

When the returned signal was thought to be the result of a reflection from a satellite or item of space debris the power profile measured on the LP2 channel shows a sudden sharp increase followed by a similarly sudden sharp decrease approximately 100 km further along the beam, as shown in Figure 4.4(b). The spacing between these steps in the power is related to the range ambiguity of the sounding pulse, so a satellite large enough to cause a significant change in the returned power is detected in several range gates. This explains why the power increase is visible over 100 km range.

(a).

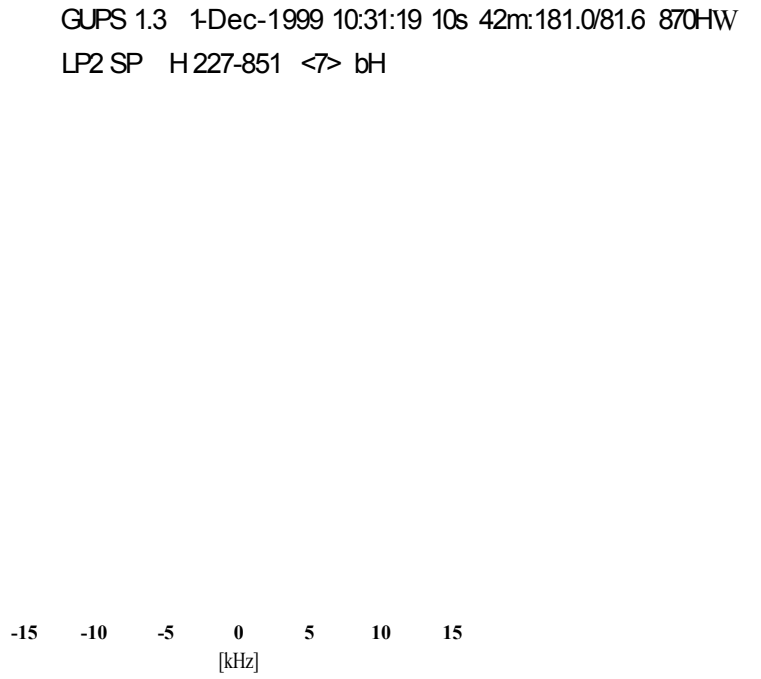

(b).

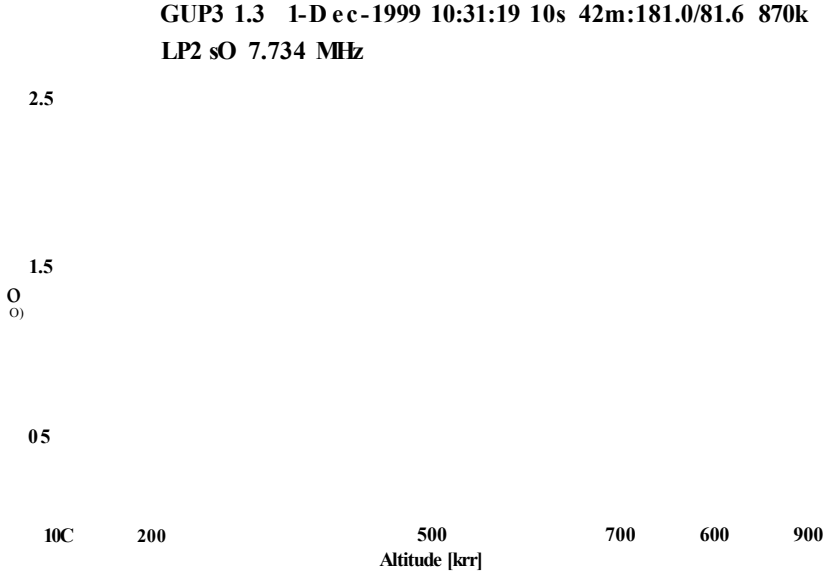

Figure 4.4: Results showing (a) spectra and (b) power profile for LP2 data at 10:31:19 UT, 1st December 1999, using EISCAT rtg3 program when a probable satellite was seen in the beam.

Sometimes the object detected is at a sufficiently high altitude for only the increase in power, but not the subsequent decrease, to be within the range coverage of the recorded data. These situations are classified as possible satellites.

In contrast to these examples, there are times when enhanced spectra are present in the data but the power profile shows no significant change, as shown in Figure 4.5. The spectra obtained at these times can, therefore, be the result of a geophysical phenomenon. In a situation where the enhancements in one ion line switch to the other (Sedgemore-Schulthess *et al.*,1999), the enhancements are thought to be short-lived as are those for satellites. However any increase in power which occurs is likely to be gradual rather than sudden, so it takes several range gates for the full increase to show in such geophysical situations. The example shown in Figure 4.5 needs further consideration if it is to be identified definitely, either as a geophysical phenomenon or as one or more satellites passing through the beam.

As a result of this study it was decided that a modification could be made to the subroutine used in the rtg3 program so that at each range the power could be calculated from the spectrum values. The power is given by calculating the area under the spectrum. Since the program finds points on the spectrum at discrete frequency intervals it was possible to obtain values which would be representative of the power profile by summing the spectral values.

Initially the subroutine was modified to:

1. find the difference between adjacent pairs of powers,
2. divide this difference by the smaller of the two power values, and
3. send an indication of the size of the resulting ratio to the output text file.

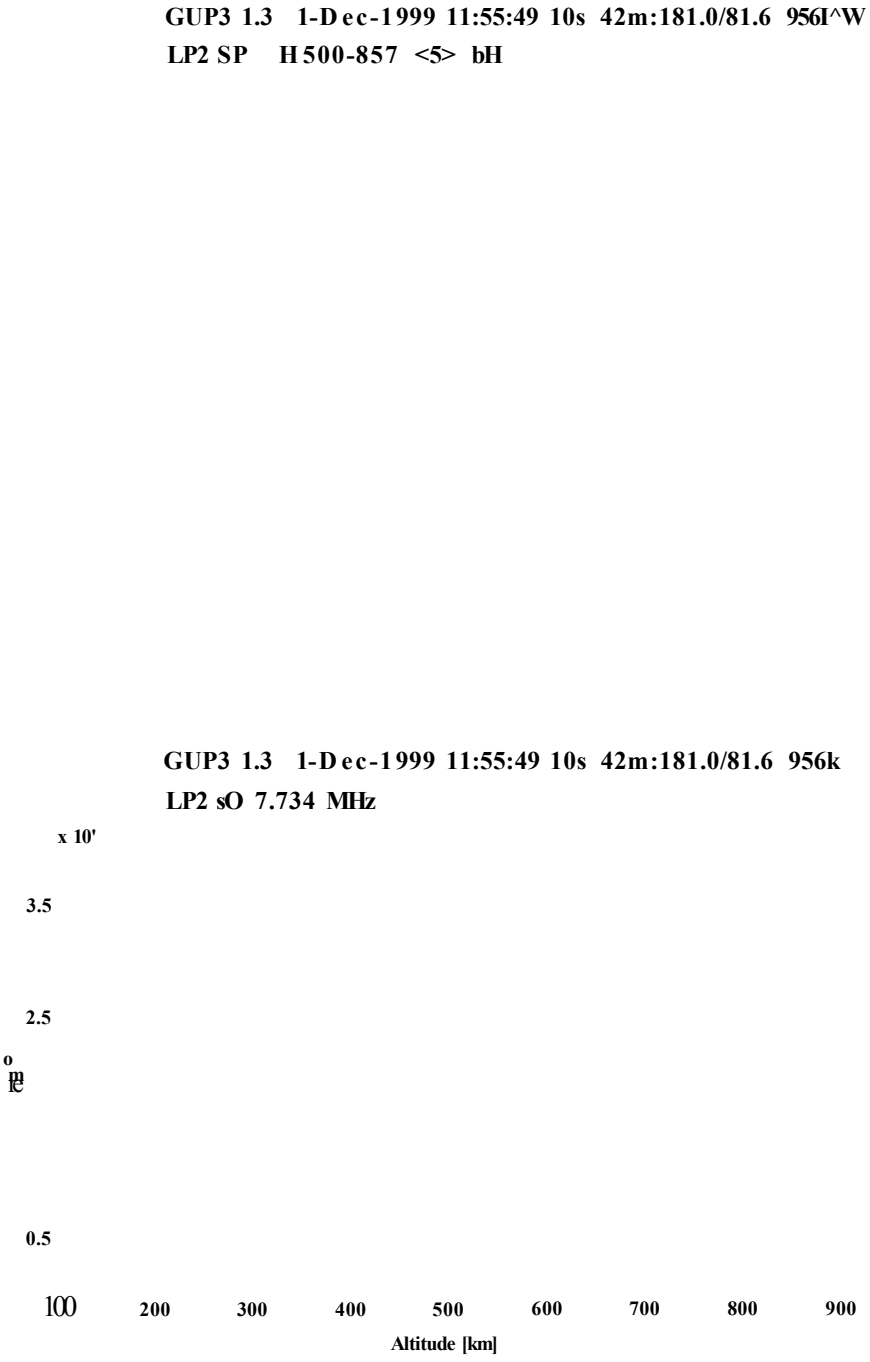

Figure 4.5. Results showing (a) spectra and (b) power profile for LP2 data at 11:55:49 UT, 1st December 1999, using EISCAT rtg3 program when enhanced spectra probably due to geophysical causes were seen in the beam.

At the start of the program a third parameter, the critical ratio, needed to be input. Three cases were then identified:

1. **The output file would return 0** at the times when the absolute values of the ratio were smaller than the critical ratio for all ranges. These were cases which may be of some geophysical interest, though the possibility of them arising as a result of the radar beam detecting a small item of space debris could not be neglected.

2. **The output file would return 1** if there were ranges for which either the ratio exceeded the critical ratio or if it were less than minus the critical ratio, but not both. In particular, this would locate those cases where the radar beam had apparently identified a hard target, but so near to the extreme limit of its range that the power was not seen to fall off.

3. **The output file would return 2** if there were ranges where the ratio exceeded the critical ratio in addition to some where it was less than minus the critical ratio within the same ten-second dump. These were the cases where the power clearly showed a sudden increase followed by a sudden decrease. They were the cases when the radar beam could be considered to have definitely detected a hard target such as a satellite or item of space debris.

This version of the subroutine was tested using the data for 1st December 1999 by comparing the results obtained using the program with those expected as a result of doing a manual check. After running the program with several different ratios it was decided that further modifications needed to be made as explained in the following paragraphs.

The values of the powers used by the program to calculate the ratios were exported into an EXCEL file. Some examples of the results for 1st December 1999 are shown in Figure 4.6.

(a).

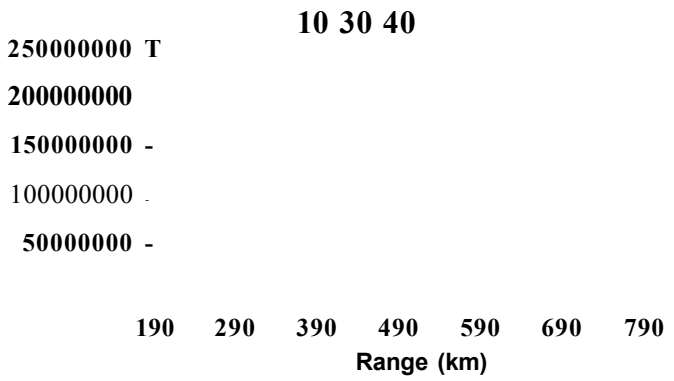

(b).

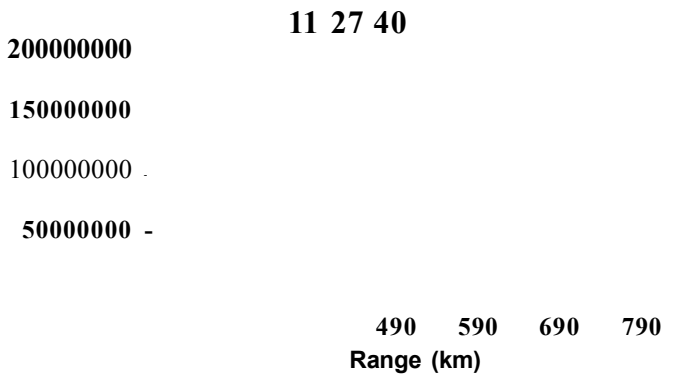

(c).

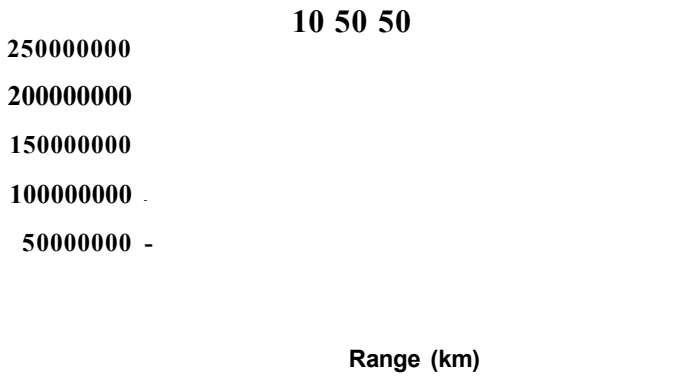

Figure 4.6: EXCEL charts showing the rtg3 subroutine's calculated values for the power using the LP2 data of 1st December 1999. The charts shown were considered to be typical of (a) a probable satellite, (b) a possible satellite and (c) a possible enhancement due to a geophysical phenomenon.

These charts vary slightly from those obtained for the power profile using the rtg3 plot window. This is a result of summing over discrete points of the spectrum. However, the overall shape is sufficiently similar to that obtained by using the raw data as in the rtg3 plots. This can be seen by comparing the charts in Figure 4.6 with those obtained in rtg3 for the same time periods as shown in Figure 4.7. Hence they could be used to give an indication of the behaviour of the power profile.

As a result of plotting the calculated powers for each ten-second dump showing asymmetric spectra in the 1st December 1999 data, it can be seen, from the charts in Figure 4.6, that to obtain the maximum size of the power increase and decrease when a probable satellite was detected, would mean considering the values of the power which were three apart. Hence the program was altered to use powers obtained from spectra which were three apart rather than adjacent ones when calculating the power ratio. It was also realised that it was only necessary to check for the sudden decrease in power if there had already been a sudden increase at a smaller range within the ten-second data dump. Using the results obtained earlier, the required calculations were performed in the spreadsheet for the test data. Since this was seen to be successful, the subroutine was altered accordingly. Using the results from the EXCEL file it was decided that a suitable value to enter for the critical ratio in order to test for a satellite was in the region of 0.2.

A detailed study of the power profiles using the data from 1st and 2nd December 1999 reveals that a few very large power variations are seen, which are clearly attributable to satellites. Excluding these, the remaining variations show a continuous distribution, rather than being sharply divided between large and small changes. The distribution is shown in the histogram in Figure 4.8. In order to accommodate the full range of power variations on the same graph, the natural logarithm of the power variation has been plotted.

(a).

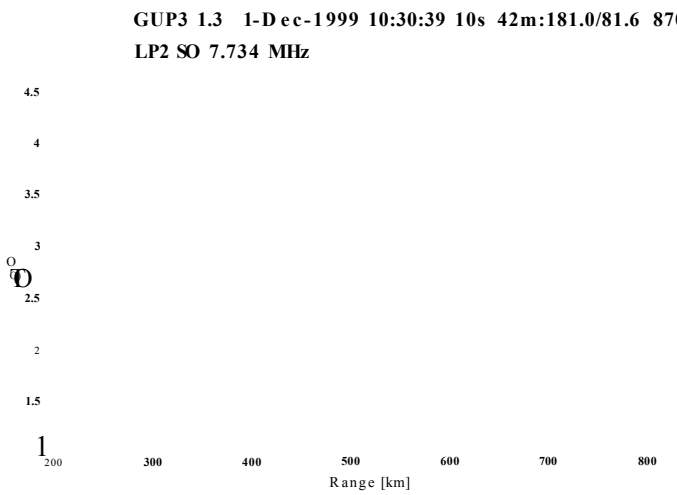

(b).

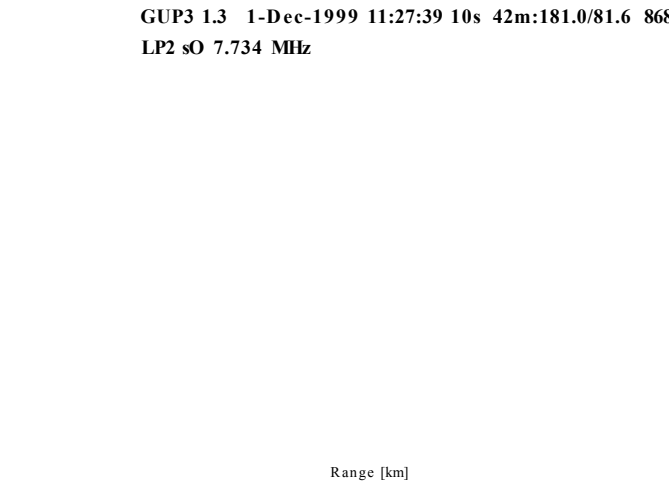

(c).

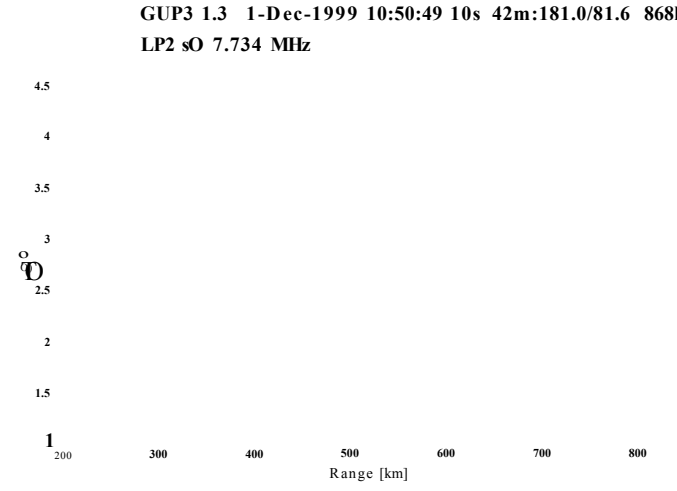

Figure 4.7: Power profiles obtained using rtg3 for (a) a probable satellite, (b) a possible satellite and (c) a possible enhancement due to a geophysical phenomenon.

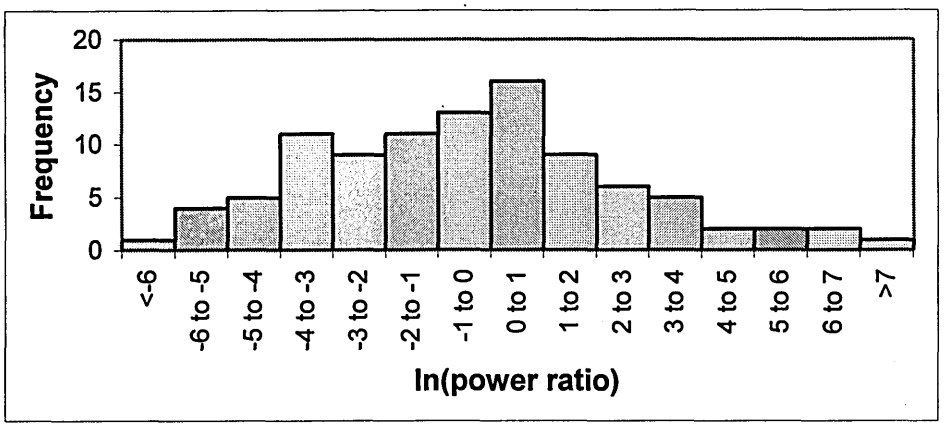

Figure 4.8: Histogram showing frequency of occurrence of ln of power ratios obtained when enhanced spectra occurred in the 1st and 2nd December 1999 ESR, GUP3 data.

Considering the histogram in Figure 4.8, the cases at the left-hand extreme of the *x*-axis are highly likely to be due to geophysical conditions, whilst those at the right-hand extreme are highly likely to be due to satellites. This leaves a large number of intermediate points, many of which could also be due to satellites, either of varying cross-section, or passing through the side lobes rather than the main beam.

4.4 Long Pulse and Alternating Code Comparisons

To progress further a comparison was made between the long pulse (LP2) results and those from the alternating code (AC2) data. The LP1 and AC1 results were also checked to ensure that they were consistent. The range extent of the LP2 long pulse data is 229.5–859.5 km whilst for the AC2 alternating code data it is only 228–732 km. Hence the LP and AC data overlap within a region whose range extent is about 500 km. Within this region, full measurements of the shape of the backscattered spectrum can be obtained from both schemes, along with "power profiles", representing the variation in the backscattered power as a function of range. As a

consequence, only a subset of the anomalous spectra identified in the LP2 data could be checked using the AC2 data.

By examining the power profile from the AC2 data at the relevant times it soon became clear that similar characteristics could be seen, as are shown in the Figure 4.9. When the enhanced spectra are probably due to a satellite passing through the beam the AC2 power profile shows a steep pointed peak; otherwise there is no significant change. The smaller extent of the peak in the power profile response arises because the range resolution is better for the alternating code data than it is for the long pulse data. At these times the peak of the AC power is confined to a very narrow range and is within the region in which the step occurs in the LP data. Thus good agreement is shown between the two pulse schemes. In addition, the use of the AC data helps to clarify a number of cases where the LP data alone does not provide an unambiguous identification of a satellite.

In order to classify the data the threshold ratio of 0.2 for the LP power increases between range gates, as described earlier in this chapter, was considered. Above this ratio, it is possible to be reasonably sure that a satellite has been detected, rather than anomalous spectra due to geophysical conditions. Below this ratio geophysical causes are more likely but there is a possibility that the anomaly is caused by very small items of space debris or a satellite being detected in the far side lobes of the radar beam. For the data considered here the threshold value of 0.2 was seen to be acceptable for this ratio when the power profiles could be checked in both the AC and the LP data. This represents a 20% increase in the returned power. Since the output from the program only records the value of the greatest ratio found in a 10 second dump, any examples which are close to this threshold need to be checked manually.

In order to verify that satellites or their debris did indeed passed through the beam at the identified times another source of independent evidence needed to be considered.

(a).

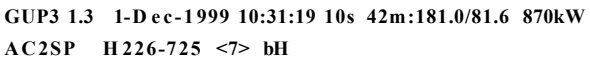

(b).

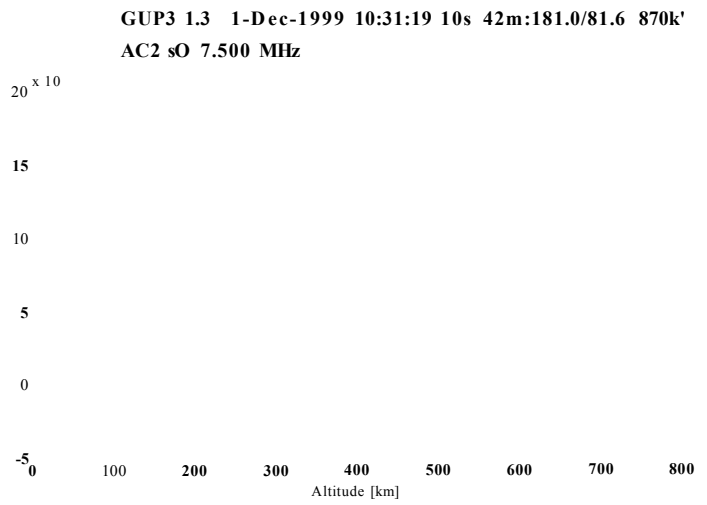

Figure 4.9: Results showing (a) spectra and (b) power profile for AC2 data at 10:31:19 UT, 1st December 1999, using EISCAT rtg3 program when a probable satellite was seen in the beam.

Chapter 5

Satellites

5.1 Satellite Contamination

Although the purpose of this research is to study the naturally enhanced anomalous spectra, it is now clear that it will be necessary to be extremely careful since some of the anomalous spectra caused by satellite contamination may easily be mistaken as being of geophysical origin. In order to avoid this happening some further work needs to be done with regard to the satellite contamination.

This work continues to use the GUP3 data, from 1st December 1999 as was used in Chapter 4. The data set consists of 1011 ten-second dumps recorded between 10:11:30 UT and 13:00:00 UT. The radar beam was set at an elevation of 81.6° and an azimuth of 181.0°. Hence it was aligned with the Earth's geomagnetic field. The automated subroutine, "test_asymm", described in Chapter 4 is used to examine the data from the LP2 long pulse channel.

The times at which anomalous spectra in the LP2 data are identified by the program are recorded for subsequent manual examination. After eliminating the noise we are left with a number of spectra where the program suggests the presence of a satellite. Typical enhanced spectra from such a case were shown in Chapter 4, Figure 4.4.

We now consider ways of calibrating such identifications to verify that satellites or their debris have indeed passed through the beam.

5.2 Orbital Elements

The monitoring of satellites and space debris, and the determination of their orbital parameters is an important activity for the space industry. Many such objects are routinely monitored and their positions can subsequently be reconstructed. Data files are available from which it is possible to determine the position of a satellite at any time. The rules which govern the orbits of satellites were first studied by J. Kepler (1571–1630). In order to specify the particular orbit we need to know the values of six key elements. These are known as the Keplerian orbital elements. They are:

1 Inclination, i,

2 Right Ascension of Ascending Node, Ω,

3 Argument of Perigee, ω,

4 Eccentricity, e,

5 Mean Motion, T_0,

6 Mean Anomaly at epoch, ψ_τ.

(a).

(b).

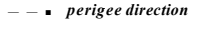

Figure 5.1: Diagrams to show the orbital elements used to describe the motion of a satellite (a) with respect to the Earth and (b) within an orbit. (http://spaceflight.nasa.gov/realdata/elements/graphs.html).

In Figure 5.1(a), the plane of the Earth's equator is shown as the $\overline{XY}$ plane. The satellite travels around the Earth in an elliptical orbit. (In reality, the motion is more complex than this and small corrections need to be made for perturbations which add extra parameters). The centre of the Earth is positioned at one of the focal points of the ellipse.

5.2.1 Inclination

The inclination, *i*, is the angle between the plane of the equator and the plane of the elliptical orbit. So satellites in equatorial orbits will have inclinations around 0° whilst those in polar orbits will have inclinations around 90°. By convention, if the satellite rotates in the same direction as the Earth, i.e. anti-clockwise when viewed from above, then it has an inclination of 0° – 90° whereas if it rotates in the opposite sense to that of the Earth then it has an inclination over 90°. A satellite which is likely to pass over the ESR site is therefore in a near polar orbit and may have an inclination in the region between 75° and 105°.

5.2.2 Right Ascension of Ascending Node

The line along which the satellite's orbital plane intersects the Earth's equatorial plane is called the line of nodes as shown in Figure 5.1. The point at which the satellite crosses this line when travelling from the Southern Hemisphere to the Northern Hemisphere is called the ascending node, whilst the corresponding point on the opposite side of the line of nodes where the satellite is travelling from the Northern Hemisphere to the Southern Hemisphere is called the descending node.

As the orbit of a satellite is fixed relative to the stars and not the Earth's surface, an astronomical co-ordinate system is needed to measure the position of the ascending node. Such a system uses the first point of Aries as its reference point. This point is the same as the vernal equinox, which is where the Sun crosses the Earth's equator in the spring. The right ascension of the ascending node, Ω, is thus the angle, measured in the equatorial plane, from the first point of Aries (the $\overline{X}$-axis in Figure 5.1) to the line of nodes. This describes the position of the orbital plane in space.

5.2.3 Argument of Perigee

Next it is necessary to determine the position of the orbital ellipse within the orbital plane. To do this we use the argument of perigee. The perigee is the point on the ellipse which is closest to the Earth. Similarly the apogee is the point on the opposite side of the ellipse which is furthest away from the Earth. The line joining the perigee and the apogee is called the major axis of the ellipse. It has a length of $2a$ in Figure 5.1(b). The angle, measured in the plane of the orbit, between the major axis and the line of nodes is referred to as the argument of perigee, ω. The angle can take values ranging from 0° to 360°. It is 0° when the perigee and the ascending node coincide and 180° when the apogee and the ascending node coincide. It is between 0° and 180° when the perigee is North of the equator.

5.2.4 Eccentricity

The eccentricity, e, determines the shape of the ellipse. It is defined as the ratio of the distance from the centre of the ellipse to the focus and half the length of the major axis, otherwise known as the semi-major axis, which has length a. If the eccentricity were 0 then the distance from the centre of the ellipse to the focus would be 0, so the

shape would in fact be a circle. As the eccentricity increases the ellipse becomes longer and thinner.

5.2.5 Mean Motion

We have already mentioned the semi-major axis, *a*, which determines the size of the elliptical orbit. However, it is common practice when giving the elements of the orbit to use a different but related parameter called the mean motion. This is the mean angular rotation of the satellite. The speed of the satellite is related to the semi-major axis by Kepler's Third Law which gives the square of the period of the orbit, T_o, as being proportional to the cube of the semi-major axis, *a*, i.e. $T_o^2 \propto a^3$, or $KT_o^2 = a^3$, where *K* is a constant of proportionality. This result shows that a satellite which is further from the Earth will move slower than one which is closer to the Earth.

Since a satellite in an elliptical orbit, according to Kepler's Second Law, will sweep out the same area in the same time interval no matter where in the orbit it is, then it will move faster at perigee and slower at apogee. The mean motion is the average rate of the satellite motion and is usually given as the number of revolutions per day. The period is the reciprocal of the mean motion. So, for example, a satellite with a mean motion of 16 revolutions per day will have a period of $\frac{24}{16} = 1.5$ hours.

5.2.6 Mean Anomaly at Epoch

The final element required to define the position of a satellite relative to the Earth is where in its orbit the satellite is at some specific time. To specify this we choose a

time, close to the required time, at which the satellite passes its ascending node. This time will be referred to as the epoch, τ. The position of the satellite in the orbit is specified by giving the angle between its position and its perigee. This is called the true anomaly, v_0. However, since the satellite does not travel in a circular orbit this is complicated to calculate. Therefore it is usual to use instead the mean anomaly which is the position that a satellite travelling in a circular orbit would have if it had the same period (and therefore mean motion) as that of the satellite travelling in an elliptical orbit. This is easily calculated as

the time since epoch × the mean motion + mean anomaly at epoch.

5.3 Two-Line Element Files

It is possible to obtain files containing the key elements for many satellites and items of space debris. They are usually described as two-line element sets (TLEs) and are updated approximately weekly. For the purpose of tracking the satellites or their debris it is best to obtain such a file which has been updated as close as possible to the day of interest in order to minimise the errors in calculating the satellite positions. A two-line element file which had been updated on 2nd December 1999 was obtained from the web site

ftp://seds.lpl.arizona.edu/pub/sat/satelem/el-1999

The file contains the details for 8132 items. The details for each item are recorded on three lines of the file, contrary to what the file name suggests. However, the initial line simply provides the NORAD (North American Air Defense) Catalogue number and/or other information such as the common name assigned to the satellite. The following two lines are the standard Two-Line Orbital Element Set Format identical to that used by NORAD and NASA (National Aeronautics and Space Administration). In particular the first of these two lines contains details of the epoch

and drag terms, whilst the second line has details of the inclination, right ascension of the ascending node, eccentricity, argument of perigee, mean anomaly at epoch and mean motion. Used along with the satellite tracking programme "Element Manager for Windows" by Rick von Glahn, which was downloaded from the web site

http://www.elementmanager.com/

it is possible to select a particular satellite and find its position relative to the ESR site at some particular time.

5.4 Tracking Satellites

A satellite can gain an advantage during launch if it is to traverse its orbit in the same sense as the Earth's rotation. The advantage will be greater the closer the plane of the satellite orbit is to the Earth's equatorial plane. As a result many of the satellites are travelling in near equatorial orbits. However, if a satellite is likely to pass through the ESR beam it must be travelling in a near polar orbit. It is reasonable, therefore, to restrict the set of items being considered to those whose inclination is between 75° and 105°. Additionally, the range of the ESR beam is limited, so a further restriction to the set of items being considered is to restrict the value of the perigee to a maximum of 900 km. The effect of these restrictions is to reduce the number of items to be checked from 8132 to 1695.

The "Element Manager" program used to track the satellites is capable of finding the position of a given satellite or item of space debris at a particular time, but does not allow a search to be made to identify which items in the set are in a specific region at a given time. So it is necessary to find some other means to restrict the number of items which need to be checked. To achieve this, the details of the orbital elements for

Column	Description	Units
A	Satellite number	
B	Inclination, i	degrees
C	Eccentricity $\times 10^7$	
D	Epoch date, τ	
E	Right ascension of ascending node, Ω	degrees
F	Eccentricity, e [=C4*10^(-7)]	
G	Argument of perigee, ω	degrees
H	Mean anomaly at epoch, ψ_τ	degrees
I	Mean motion, T_0	revolutions per day

Table 5.1: The satellite parameters as entered in the fourth and following rows of the EXCEL spreadsheet used to identify the items whose positions needed to be checked at a specified time.

the 1695 identified items were loaded from the two-line element set into an EXCEL spreadsheet as shown in Table 5.1. An excerpt from the spreadsheet is reproduced as Appendix B,

The satellite number in column A is needed to help identify the items. The orbital parameters are recorded in columns B–I. The two-line element file does not record the position of the decimal point in the value for the eccentricity. This is taken into account in column F where the actual value of the eccentricity is calculated by multiplying the value in column C by 10^{-7}. The formula for e which is entered into row four of the spreadsheet is shown in Table 5.1.

Cell	Contents	Units
B1	Radius of the Earth, R_E [=6.379*10^6]	m
G1	Mass of the Earth, M_E [=5.975*10^24]	kg
J1	Gravitational constant, G [=6.673*10^(-11)]	$N\,m^2\,kg^{-2}$
M1	Constant of proportionality, $K = \frac{M_E G}{4\pi^2}$ [=G1*J1/(4*(PI()^2))]	$N\,m^2\,kg^{-1}$
S1	Time [=62840+T1+U1]	
T1	Date	dd/mm/yy
U1	Time	hh:mm:ss
Z1	Longitude of the first point of Aries [=MOD(-(S1-99081.5)*366.25*360/365.25,360)]	degrees

Table 5.2: The entries in the first row of the EXCEL spreadsheet used to identify the items whose positions needed to be checked at a specified time.

In order to calculate an approximate position for a satellite some additional constants are required. These are entered in the first row of the spreadsheet as shown in Table 5.2. Where formulae are given in square brackets in Tables 5.1 and 5.2 they are the actual formulae as they appear in the spreadsheet.

The remaining entries in the spreadsheet are shown in Table 5.3. The formulae in square brackets are those which actually appear in the fourth row of the spreadsheet. This is the first row of the data. These formulae were then copied down the rest of the rows of data.

Column	Contents
J	a^3 [=$M$1*(3600^2)*((24/I4)^2)]
K	Semi-major axis, a [=J4^(1/3)]
L	Perigee [=(K4-K4*F4-$B$1)/1000]
M	Apogee [=(K4+K4*F4-$B$1)/1000]
N	Altitude [=(K4*(1-F4*COS(RADIANS(Q4)))-$B$1)/1000]
O	Mean anomaly [=MOD(MOD(I4*($S$1-D4),1)*360+H4,360)]
P	Mean anomaly (radians) [=RADIANS(MOD(O4,360))]
Q	True anomaly [=DEGREES(P4+((24*F4-3*F4^3)*SIN(P4) +15*F4^2*SIN(2*P4)+13*F4^3*SIN(3*P4))/12)]
R	Semi-minor axis, b [=K4*SQRT(1-F4^2)]
S	Distance from line of nodes to satellite, d [=MOD(Q4+G4,360)]
T	Latitude [=DEGREES(ASIN(SIN(RADIANS(S4))*SIN(RADIANS(B4))))]
U	cos η [=COS(RADIANS(S4))/COS(RADIANS(T4))]
V	sin η [=SIN(RADIANS(S4))*COS(RADIANS(B4))/COS(RADIANS(T4))]
W	η [=IF(U4>0,DEGREES(ASIN(V4)),180-DEGREES(ASIN(V4)))]
X	Right ascension of satellite [=W4+E4]
Y	Longitude [=MOD(X4+$Z$1,360)]
Z	Test [=IF(AND(N4<900,AND(T4>65,AND(Y4>-10,Y4<40))),1,"")]
AA	Test eccentricity [=IF(F4>0.2,1,"")]
AB	Test epoch date [=IF($S$1-D4>6,1,"")]

Table 5.3: The entries, containing formulae to estimate the positions of the items needed to be checked at a specified time, taken from the fourth row of the EXCEL spreadsheet.

The motion of a satellite about the Earth obeys Kepler's three laws, which were originally deduced to describe the motion of the planets about the Sun. However these laws do not take account of any external perturbations, e.g. air resistance, asymmetrical gravitational field, the gravitational attraction of the moon, etc. They were later shown by Sir Isaac Newton (1642–1727) to be deducible from the law of universal gravitation.

The law of universal gravitation states that every particle of matter attracts every other particle of matter with a force which is proportional to the product of the masses of the two particles and inversely proportional to the square of the distance between them.

In the case of a satellite orbiting the Earth, the Earth can be considered to be a particle whose mass is concentrated at its centre. The mass of the satellite is negligible compared with the mass of the Earth.

According to Kepler's third law, we have:

$$T_o^{\,2} = \frac{4\pi^2 a^3}{GM_E}$$

for a body moving in a circular orbit of radius a.

So,

$$a^3 = \frac{GM_E}{4\pi^2} \times T_o^{\,2}$$ (calculated in column J)

Hence,

$$a = \sqrt[3]{\frac{GM_E}{4\pi^2} \times T_o^{\,2}}$$ (calculated in column K)

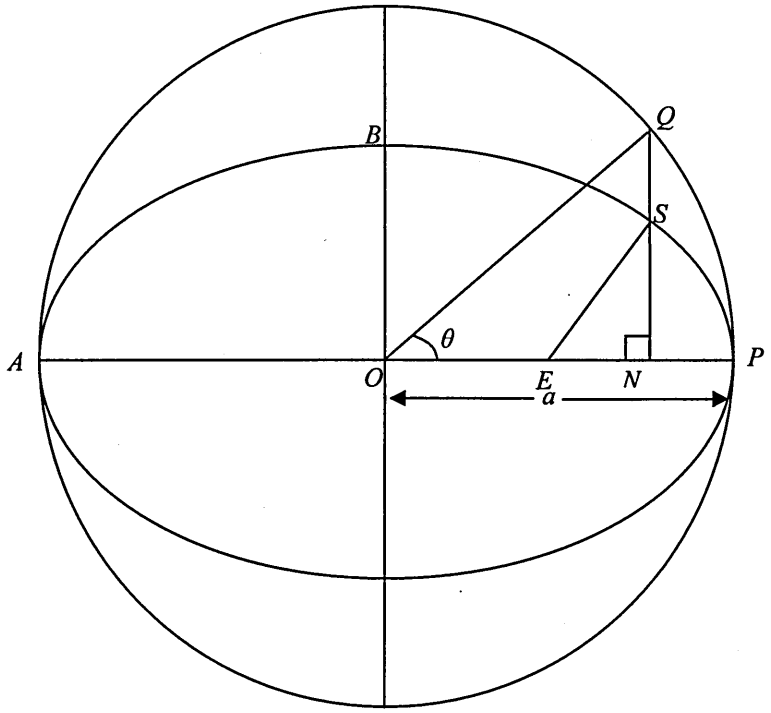

Figure 5.2: Geometric showing the elliptical orbit of a satellite, *S*, and its encircling circular orbit.

Although the value *a* just calculated is the radius of a circular orbit it will be equal to the semi-major axis of the elliptical orbit of the satellite as shown in Figure 5.2, (Smart, 1960).

Kepler's first law states that the path, or orbit, of the planet around the Sun is an ellipse, with the Sun being positioned at a focus of the ellipse. Using the standard properties of an ellipse and applying the law to a satellite, *S*, moving around the Earth, *E*, gives:

$$OE = ae$$
$$EP = a - ae$$
$$AE = a + ae$$

Since EP and AE are measured from the centre of the Earth then the distance from the Earth's surface to perigee is given by:

$$a - ae - R_E \qquad \text{(calculated in column L)}$$

Similarly the distance from the Earth's surface to apogee is:

$$a + ae - R_E \qquad \text{(calculated in column M)}$$

Now it is also possible to obtain the length of the semi-major axis using the relationship:

$$\text{Semi-minor axis} = OB = b = a\sqrt{(1-e^2)} \qquad \text{(calculated in column R)}$$

To calculate the altitude of a satellite at some specific time it is necessary to find the distance ES when the satellite is in the position S on its elliptical path. To help achieve this, once again the circle with diameter equal to the major axis of the elliptical orbit is considered. The perpendicular, SN, is drawn from S to the major axis, AP. The line NS is produced to meet the circle at Q as in Figure 5.2.

Then $QN = QO\sin\theta = a\sin\theta$

Using the well-known relationship for an ellipse:

$$\frac{SN}{QN} = \frac{b}{a}$$

gives $$SN = \frac{b}{a} \times QN = \frac{b}{a} \times a\sin\theta = b\sin\theta$$

Since,
$$\begin{aligned} EN &= ON - OE \\ &= a\cos\theta - ae \\ &= a(\cos\theta - e) \end{aligned}$$

By Pythagoras,

$$\begin{aligned} ES^2 &= EN^2 + SN^2 \\ &= a^2(\cos^2\theta - 2e\cos\theta + e^2) + b^2\sin^2\theta \\ &= a^2(\cos^2\theta - 2e\cos\theta + e^2) + a^2(1-e^2)\sin^2\theta \\ &= a^2(\cos^2\theta - 2e\cos\theta + e^2 + \sin^2\theta - e^2\sin^2\theta) \\ &= a^2((\cos^2\theta + \sin^2\theta) - 2e\cos\theta + e^2(1-\sin^2\theta)) \\ &= a^2(1 - 2e\cos\theta + e^2\cos^2\theta) \\ &= a^2(1-e\cos\theta)^2 \end{aligned}$$

So $ES = a(1-e\cos\theta)$

This is the distance of the satellite from the centre of the Earth. Therefore the altitude of the satellite is given by:

$a(1-e\cos\theta) - R_E$ (calculated in column N)

It now remains to find the true anomaly. To do this we must first find the mean anomaly. This involves adding the product of the mean motion, T_o, and the time after the epoch to the mean anomaly at epoch.

Let the time we are interested in finding a satellite be *t*. This is entered in cell S1 of the EXCEL spreadsheet. The epoch, τ, and the mean anomaly at epoch, ψ_τ, for each satellite are given in columns D and H respectively of the spreadsheet. So the mean anomaly, ψ_t, is given by:

$\psi_t = T(t-\tau) + \psi_\tau$ (calculated in column O in degrees, and converted to radians in column P)

In order to calculate the true anomaly we need to make use of Kepler's second law which states that the vector from the centre of the Earth to the satellite sweeps out equal areas in equal time intervals as the satellite moves around the Earth.

Unfortunately there is no simple formula which relates the two anomalies for all values of the eccentricity. However for small values of the eccentricity the following power series expansion is valid:

$$\nu_o = \psi_t + ((24e - 6e^3)\sin\psi_t + 15e^2 \sin 2\psi_t + 13e^3 \sin 3\psi_t)/12$$

(Smart, 1960)

(calculated in column Q)

We now have sufficient information to be able to calculate the latitude of the satellite at a specific time. To find the latitude we use the spherical triangle NSL_N shown in Figure 5.3, in which the position of the satellite has been projected up onto the celestial sphere. Here N is the North Pole and L_N is the point at which the line of nodes intersects the Earth's equator. Now,

SL_N = argument of perigee + true anomaly

i.e. $d = \omega + \nu_o$ (calculated in column S)

Using spherical trigonometry, the cosine rule gives:

$$\cos(90° - \lambda_S) = \cos 90° \cos d + \sin 90° \sin d \cos(90° - i)$$

Hence,

$$\sin\lambda_S = \sin d \sin i$$

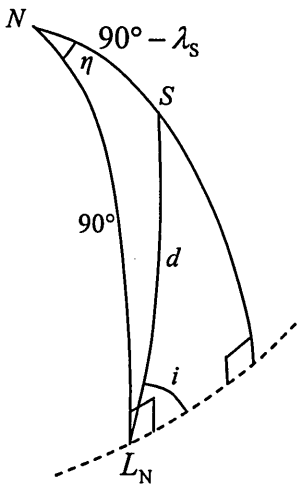

Figure 5.3: Geometric showing the measurements required to calculate the geographical latitude of a satellite, *S*.

So the latitude of the satellite is given by:

$$\lambda_S = \sin^{-1}(\sin d \sin i) \qquad \text{(calculated in column T)}$$

To calculate the longitude of the satellite we need to know the longitude of the first point of Aries. This will depend upon the time in which we are interested. The date is entered in cell T1 and the time in cell U1 of the spreadsheet. This is converted in cell S1 to a format which is compatible with that used for the epoch date in the two-line element file. The longitude of the first point of Aries is 0° at noon on the Vernal Equinox and moves in a Westerly direction around the Earth's equator once in every stellar day. Therefore its longitude at *D* solar days after the Vernal Equinox is given by:

$$\theta_\gamma = -D \times \frac{366.25}{365.25} \times 360°$$

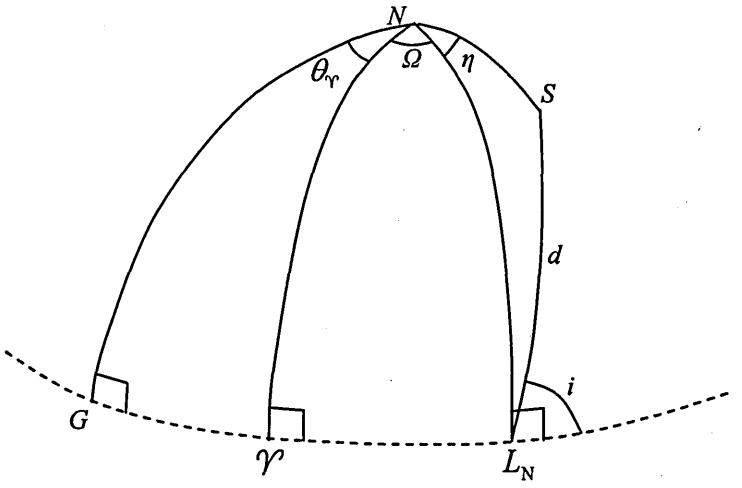

Figure 5.4 Geometric showing the measurements required to calculate the geographical latitude of a satellite, *S*.

It can be seen using Figure 5.4 that the longitude of the satellite is given by:

$$\theta_S = \theta_\gamma + \Omega + \eta \qquad \text{(calculated in column X)}$$

where η is the angle $L_N NS$.

Since η can take any value between 0° and 360° we need to calculate both its sine and cosine.

Using the spherical triangle NSL_N

$$\cos d = \cos 90° \cos(90° - \lambda) + \sin 90° \sin(90° - \lambda) \cos \eta$$

So,

$$\cos\eta = \frac{\cos d}{\cos\lambda} \qquad \text{(calculated in column U)}$$

Using the sine rule,

$$\frac{\sin\eta}{\sin d} = \frac{\sin(90° - i)}{\sin(90° - \lambda)}$$

So,

$$\sin\eta = \frac{\sin d \cos i}{\cos\lambda} \qquad \text{(calculated in column V)}$$

If $\cos\eta$ is positive, then

$$\eta = \sin^{-1}(\sin\eta),$$

otherwise,

$$\eta = 180° - \sin^{-1}(\sin\eta). \qquad \text{(calculated in column W)}$$

It now remains to apply some tests to identify satellites which are worth checking using the tracking program. The first test determines whether the satellite is somewhere near the beam, using the calculated values for the altitude, latitude and longitude. This is carried out in column Z of the spreadsheet. The second test picks out eccentricities which are greater than 0.2 as the power series expansion above is unreliable in that case. This is in column AA. The third test checks whether the epoch date is too long ago for the calculations to be unaffected by perturbations in the orbit. This is shown in column AB. When these tests were carried out the number of satellites identified which needed to be checked was of the order of 150.

5.5 Checking for Satellites

The spreadsheet can now be used as a filter to identify those items in the two-line element file whose position it is reasonable to consider checking at a particular time using the "Element Manager" program. This program gives a more accurate position for the satellite than the spreadsheet since it accounts for small perturbations in the orbit and makes use of the first and second time derivatives of the Mean Motion as well as a drag term or radiation pressure coefficient.

As a result it was reported by Porteous *et al.* (2003), that at 10:31:13 UT an object with catalogue number 24134-94029GH is found to have an azimuth of 179.88°, an elevation of 81.63° and a range of 652 km relative to the EISCAT Svalbard Radar, as shown in the following Figure 5.5.

The radar data indicates that at 10:31:19 UT (i.e. the ten-second dump starting at 10:31:10 UT) there is a probable satellite visible in the beam. The range of the observed anomalous echo is in good agreement with the predicted position of the object.

Using spherical trigonometry, the distance of the object from the centre of the radar beam can be calculated. In Figure 5.6:

Z is the position of the zenith as seen from the ground station (ESR),
R is the position of the radar beam, and
S is the position of the satellite.

The radar beam has an elevation of 81.6°, so is 8.4° from the zenith.
Similarly, the satellite has an elevation of 81.63°, so is 8.37° from the zenith.

01/12/99 10:31 Local 24134 34029GH 01/12/9910:31 UTC

Figure 5.5: Path of space debris, NORAD number 24134-94029GH, showing its position relative to the radar at ESR at 10:31:13 UT on 1st December 1999.

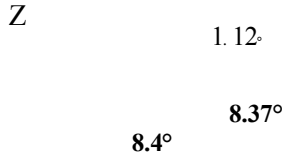

Figure 5.6: Geometrical construct to find z, the distance between the centre of the radar beam (*R*) and the object *(S)* from the angles given relative to the zenith (Z).

The radar has an azimuth of 181.0°, whilst the satellite has an azimuth of 179.88°, so, at the zenith, the angle between the radar and the object is 1.12° (= 181.0° − 179.88°).

Using the cosine rule,

$$\cos z = \cos 8.4° \cos 8.37° + \sin 8.4° \sin 8.37° \cos 1.12°$$

So,

$$\begin{aligned}\cos z &= 0.98927 \times 0.98935 + 0.14608 \times 0.14556 \times 0.99981 \\ &= 0.97873 + 0.02126 \\ &= 0.99999\end{aligned}$$

Therefore,

$$z = \cos^{-1} 0.99999 = 0.1660° = 0.002898 \text{ radians},$$

At an altitude of 652 km, this is equivalent to a distance of $0.002898 \times 652 \cong 1.9$ km.

Hence the object was less than 2 km from the centre of the beam.

This is well within the limits of the expected lateral extent (~6.5 km) of the main beam at a range of ~650 km.

This example, together with five other times at which the prediction software successfully confirms the presence of a satellite or item of space debris within the range of the beam, are shown in Table 5.4. The examples identified at 10:31:13 UT and 12:04:10 UT are likely to have been detected within the main beam, whilst the rest are more likely to have been detected in the side lobes. At each of these times the power profiles for both the LP2 and the AC2 returned signal show the typical characteristics described earlier, suggesting that the sounding pulses were being reflected from a hard target. The object detected at 11:36:35 UT is likely to have been quite large, hence, the high value obtained for the power ratio.

Time (UT) on 1st Dec 1999	NORAD Cat. No.	Angle from centre of radar beam (°)	Range (km)	Power Ratio
10:30:36	24149-94029GY	1.400	629	1.796
10:31:13	24134-94029GH	0.166	652	4.788
11:36:35	25919-99051A	0.310	706	733.497
12:04:10	12760-81053DD	0.195	762	4.467
12:06:32	25941-99057B	0.278	771	0.462
12:16:27	20466-90010B	1.394	641	2.906

Table 5.4: A sample of times at which a satellite or item of space debris appeared within the ESR beam on 1st December 1999.

At 12:07:32 UT a satellite is noticed to be 3.210° from the centre of the radar beam and at 834 km along its range. This is too great a range to enable it to be visible in the AC2 data. However, the LP2 data does show enhanced spectra around this range as well as the expected increase in power. The increase in power, though significant, is not as great as in the earlier examples. This is possibly a result of the larger distance from the beam centre, suggesting that the satellite passed through the side lobes rather than the main beam. A further satellite at 12:08:21 UT is identified to be 2.849° from the centre of the beam, but at a range of 871 km. This is not detected in either the AC2 or the LP2 data. Additionally, at 11:55:30 UT a satellite 6.319° from the centre of the radar beam and at a range of 815 km is not detected in the LP2 data.

The satellite tracking program gives the position of the satellite at one second intervals. In Table 5.4 the second when the satellite was closest to the radar beam is used. A more accurate result is obtained by considering the two seconds when the satellite passes from one side of the radar beam, S_1, to the other, S_2, as shown in Figure 5.7. We can now calculate the distance RN perpendicular to the path S_1S_2 as follows:

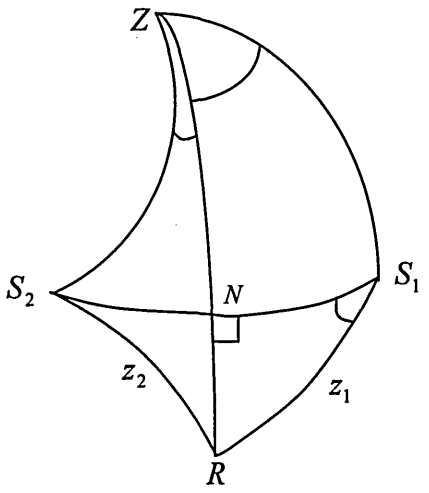

Figure 5.7: Geometric to find the closest distance between the radar beam (R) and the orbital object as it travels from position S_1 to position S_2.

Using the cosine rule,

ΔRZS_1 gives

$$\cos(z_1) = \cos(ZR)\cos(ZS_1) + \sin(ZR)\sin(ZS_1)\cos(R\hat{Z}S_1)$$

ΔRZS_2 gives

$$\cos(z_2) = \cos(ZR)\cos(ZS_2) + \sin(ZR)\sin(ZS_2)\cos(R\hat{Z}S_2)$$

whilst ΔS_1ZS_2 gives

$$\cos(S_2S_1) = \cos(ZS_1)\cos(ZS_2) + \sin(ZS_1)\sin(ZS_2)\cos(S_1\hat{Z}S_2)$$

Hence the values of z_1, z_2 and S_1S_2 can be obtained.

Using $\Delta S_1 S_2 R$, we see that

$$\cos(S_2\hat{S}_1 R) = \frac{\cos(z_2) - \cos(z_1)\cos(S_1 S_2)}{\sin(z_1)\sin(S_1 S_2)}$$

Hence the angle $S_2 S_1 R$ can be found. The arc of the great circle perpendicular to $S_1 S_2$ and passing through Z and R can be constructed. Let this arc cross $S_1 S_2$ at N. Then using ΔRNS and the sin rule gives

$$RN = \frac{z_1}{\sin(90°)} \times \sin(N\hat{S}_1 R)$$

Hence the distance $RN = z_1 \sin(S_2 S_1 R)$ can be calculated.

These calculations were carried out in an EXCEL spreadsheet for satellites found close to the beam on 1st and 2nd December 1999. A sample of the results is reproduced in Appendix C.

5.6 Comparison with Known Events

It would seem that we now have a method for determining the presence of satellite contamination in the GUP3 data. This shows that many of the cases identified by the automated rtg3 program are actually satellites, with a smaller number being of possible geophysical interest. Of the latter cases, some may still be caused by small items of space debris, or even satellites passing through the side lobes of the radar beam. Further work is still needed to identify those cases which are most likely to be of geophysical interest within this later group.

To help to refine the method for identifying those anomalous spectra of geophysical interest further, the cases which had been recorded in the paper by Sedgemore-Schulthess *et al.* (1999) were considered. There are two cases identified in this paper which are found to coincide with inferred field-aligned current bursts and energetic auroral precipitation. They are present in the GUP0 data of 24th January 1998 and occur around 07:00:40 UT and 07:06:40 UT. The two relevant times are observed using the rtg program, paying particular attention to the power profiles at these times. They do not show the sudden increase or decrease in the returned power as would be expected when there is contamination due to a satellite as at 05:35:00 UT, the time shown in Figure 5.8(a). Instead they show a slight, gentle increase and decrease (a smooth curve rather than a square pulse). The power profile observed at 07:06:40 UT, during the one of the reported geophysical events is as shown in Figure 5.8(b). That of the other reported event shows similar characteristics.

In order to compare the results found at the two noted times in the GUP0 data with the results which have been obtained in the GUP3 data appropriate changes are made to the rtg program used to observe the GUP0 data. The changes involved enabling the automated subroutine to be used in the same way as it is when observing the GUP3 data using the rtg3 program. The result of checking the two events in the GUP0 data showed that these enhancements occurred at frequencies which were at least as large as the ion acoustic frequency. Most of the satellite contamination (though not all) causes an enhanced shoulder near to the zero frequency value i.e. there is little Doppler shift. A manual check of the text files which had been output for the GUP3 data was performed and this did appear to be true for the majority of the cases when a satellite was observed.

(a).

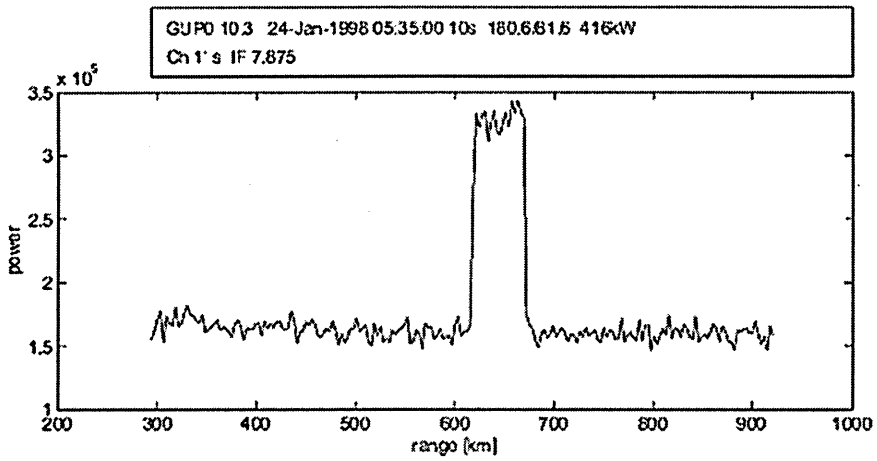

(b)

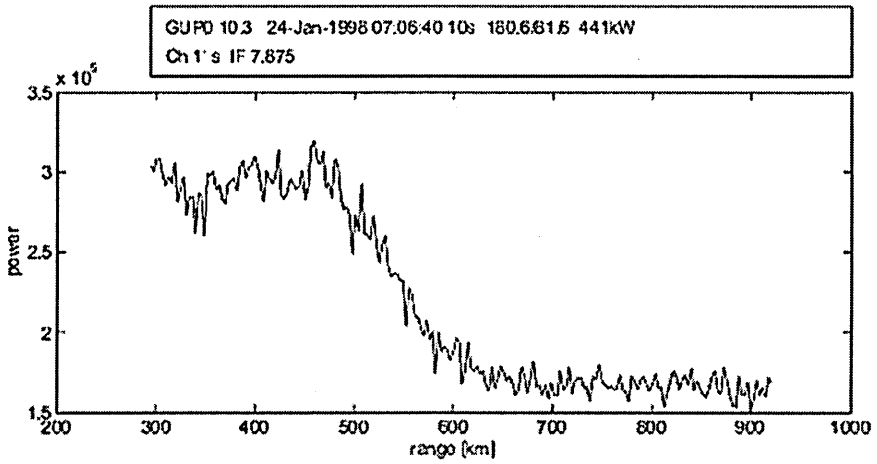

Figure 5.8: (a) Power profile for a probable satellite passing through the beam in the GUP0 data and (b) for a geophysical incident in the GUP0 data of 28th January 1998.

5.7 Further Modifications to the Subroutine

In order to help identify the events most likely to be of geophysical interest using an automated program it would appear that not only using the power profile is useful, but also the frequency at which the highest peak occurs can provide further filtering of the data. It is noted that the satellites are the most common cause of the enhanced spectra and many of these spectra have enhancements close to the normalised mean value of zero. However, some satellite contamination does result in an enhanced shoulder which is Doppler shifted by more than the ion acoustic frequency. In order to eliminate the majority of the satellite contamination it is reasonable to remove those cases of enhanced spectra in which the enhanced shoulders occur within the ion acoustic frequencies. So it is necessary to consider what the most likely values are for the Doppler shifts of the two shoulders of the spectra. Observation of the naturally enhanced spectra obtained in the GUP3 data sets suggest that the shoulders usually occur somewhere outside ± 4.5 kHz.

From the theory, the peaks of the spectra will receive a Doppler shift of

$$F(\Lambda) = \pm \frac{2}{\lambda} \sqrt{\frac{k(T_i + T_e)}{m_i}}$$

as was noted in Chapter 2.

For the ESR beam, the frequency of the wave, f, is 500 MHz, so the wavelength is given by

$$\lambda = \frac{c}{f} = \frac{3 \times 10^8}{500 \times 10^6} = 0.6 \text{ metres},$$

whilst k is Boltzmann's constant, so

$$k = 1.380 \times 10^{-23} \text{ J/°K.}$$

Assuming an O^+ ionosphere

$$m_i = 16 \text{ a.m.u.} = 16 \times 1.660 \times 10^{-27} \text{ kg.}$$

Reasonable values of the ion and electron temperatures are

$$T_i = 1000°\text{K}, \text{ and } T_e = 2500°\text{K}$$

Hence,

$$\begin{aligned} F(\Lambda) &= \pm\frac{2}{0.6}\sqrt{\frac{1.380 \times 10^{-23} \times (1000 + 2500)}{16 \times 1.660 \times 10^{-27}}} \\ &= \pm 4495.089 \text{ Hz} \\ &\approx \pm 4.5 \text{ kHz} \end{aligned}$$

As the altitude increases, the values of T_i and T_e increase. So the Doppler shift of the shoulders of the spectra will be greater at greater altitudes. In order to reduce the number of situations in which the program identifies enhanced spectra caused by satellite contamination, the program is altered in such a way that only those cases where the frequency of the highest peak is outside the region from -4.5 to +4.5 kHz are identified. This final version of the subroutine is reproduced in Appendix D. A manual check is still required to eliminate the events which were now identified as containing enhanced spectra but which are adjacent to a 10-second dump in which a satellite has probably passed through the beam at the appropriate altitude. Such enhancements may still be due to the satellite contamination in the side lobes. However this results in far fewer cases being identified by the program and a manual check of the events is therefore more feasible. Typical results showing a geophysical event and a satellite found by this search method are shown in Figure 5.9.

(a)

GUP3 1.3 3-Dec-1999 09:46:49 10s 42m: 181.0/81.6 553k|W
LP2 SP H 402-860 <7> bH

(b)

GUP3 1.3 7-Dec-199912:20:39 1Os 42m:181.0/81.6 730k|W
LP2 SP H 352-679 <5> bH

Figure 5.9: Examples of (a) a geophysical event and (b) a satellite contamination event found in the GUP3 December 1999 data using the automated subroutine.

Chapter 6

Research Outcomes: Space Storms

6.1 Classification of Data

The common programme GUP3 data available on the catalogue at RAL (Rutherford Appleton Laboratory) is now examined using the modified rtg3 program. For consistency only the situations in which the radar beam is pointing at an azimuth of 181° and an elevation of 81.6° are considered. This is when the beam is essentially field-aligned. As a consequence 404 hours of data between August 1998 and March 2000 are observed.

A record is made of each of the anomalous spectra identified by the program. These cases are then checked manually to ensure that all four channels are showing the same features.

There are only 33 ten-second dumps where the results varied in the different channels, of which 30 occurred in the December 1999 data. These cases may have been the result of technical problems within the relevant channel, or a satellite just being visible in the side lobes in one channel but not in the other channels as a result of the slight difference in the time at which the pulses are transmitted. Since there are so few of these cases they were not considered further.

There are clearly events where satellites or small items of space debris are not identified by the program since they have not caused enhanced spectra with a Doppler shift of more than 4.5 kHz.

Some of the data dumps identified by the program could clearly be classified as being due to noise in the system. Figure 6.1 shows a typical example of such a situation. This usually occurs when the radar power is being reduced or increased. These cases are not considered further.

In addition there are some instances when a satellite or item of space debris is detected in the background signal, but not in the LP2 pulse. The lower two panels of Figure 6.2 show the power profile, on the left, which has become negative as a result of the contamination seen in the background signal shown on the right. This situation is recorded as being due to noise in the background signal and therefore is not considered further.

The program helps to eliminate other situations from consideration by identifying them as probable or possible satellites or items of space debris. In such instances, a manual check of the power profile confirms the elimination.

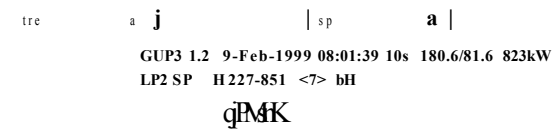

Figure 6.1: Example of data dump classified as being due to noise when spectra in adjacent ten-second data dumps appear to be normal.

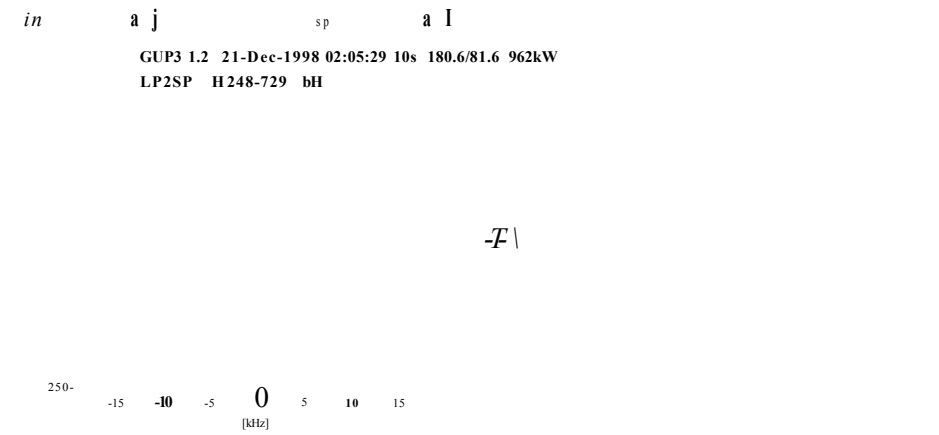

Figure 6.2: Example of ten-second data dump classified as being noise in the background signal.

The remaining occurrences of enhanced spectra are divided into two groups. They are classified as being of geophysical origin if they extend over an altitude of more than 100 km in the LP2 data and the power profile does not show a sudden increase, though a gradual increase and decrease in power is possible. Figure 6.3 shows the observed spectra and the associated power profile for such a situation. It is clear that this is not showing the same characteristics as a hard target.

The remaining group contains those which have not been clearly identified as satellites or as being of geophysical origin. A typical example is shown in Figure 6.4. Here we see no significant change in the power profile and there is only a slight suggestion of enhancement over a restricted altitude between 700 and 800 km. Although such cases may be attributable to satellite contamination the methods employed here do not clearly classify them as such. Further work would therefore be needed to identify whether these are due to satellite contamination or are caused by geophysical phenomena. As they appear to be fairly randomly spread throughout the data dumps, with no bunching at any specific times, they are not considered further here.

At this stage our interest is focused on those times at which spectra are found which can be considered to be the result of some geophysical phenomenon, i.e. the data remaining after all cases due to noise or any possible satellite contamination and any for which a cause is not clearly distinguishable at this stage have been excluded.

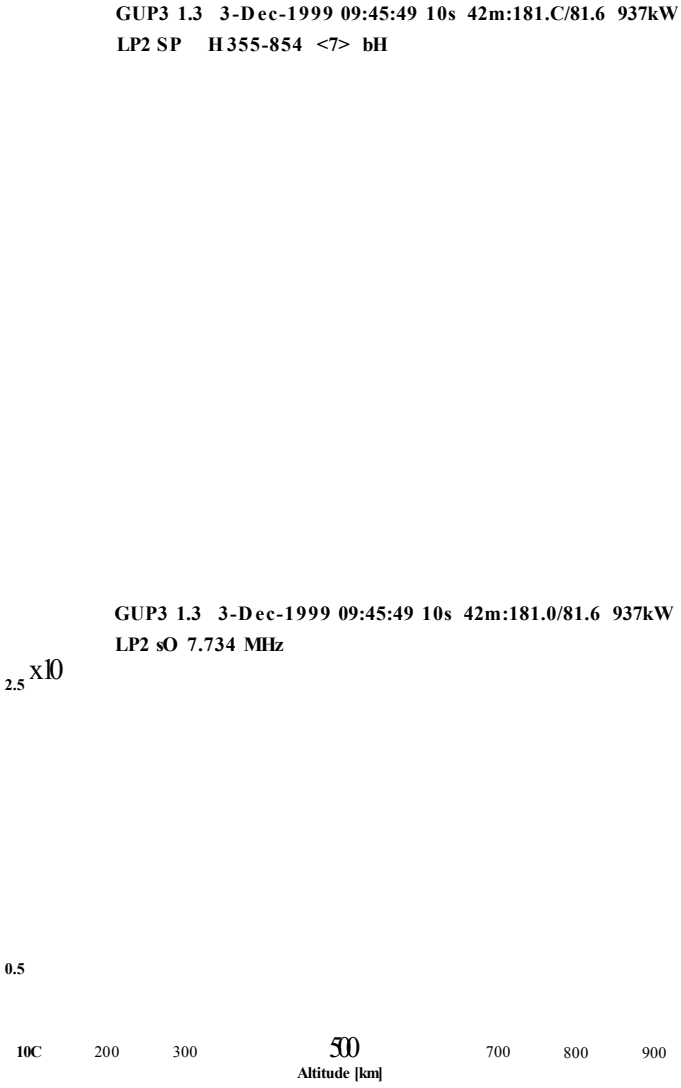

Figure 6.3: (a) Typical spectra identified as being of geophysical origin in the GUP3 data and (b) the corresponding power profile.

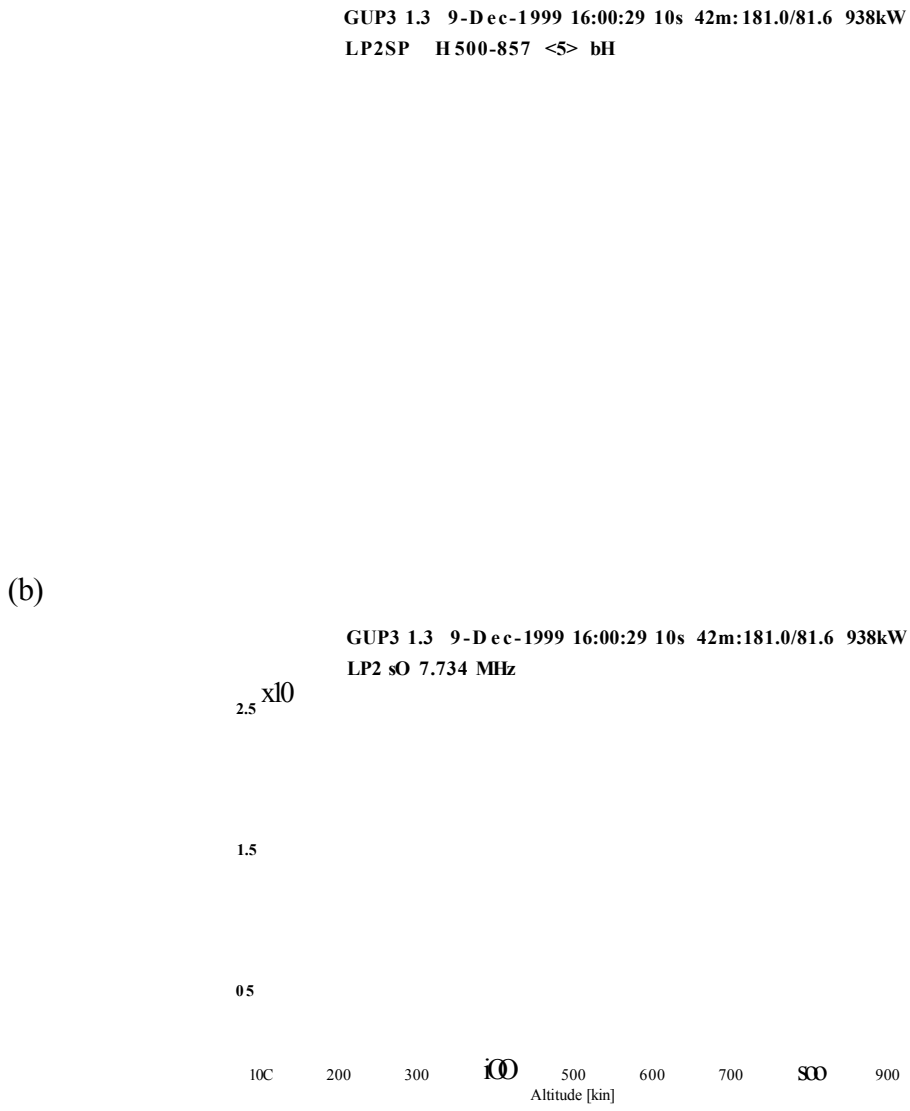

Figure 6.4: Typical example (a) showing spectra with similar features as those of a satellite with a Doppler shift greater than 4.5 and (b) the corresponding power profile which does not show any evidence of a significant change.

Year	No. of ten-sec. dumps	NEIAS	NEIAS/ Space debris
1998	53290	133	78
1999	82912	56	86
2000	9369	0	4
Total	145571	189	168

Table 6.1: Details of naturally enhanced ion-acoustic spectra (NEIAS) identified in the Common Program GUP3 data between August 1998 and March 2000.

The results in Table 6.1 clarify that only a small proportion of the ESR spectra are actually identified as being naturally enhanced spectra. This is in close agreement with the results reported by Rietveld *et al.* (1996) using data for the years 1987–1993 from the mainland site, Tromsø. The table shows that in the test data set of 145,571 data dumps 189 are identified as containing anomalous echoes (of the order of 1 in 770). A further 168 data dumps are not clearly identified as containing either satellites or anomalous echoes and require further study to clarify which category they should be placed in. It is highly likely that the majority of these 168 data dumps are due to small space debris passing through the beam or the side lobes since they appear to be randomly scattered throughout the data.

It must be noted that the data included in this study is not evenly spread over the time period, August 1998 to March 2000, so it is not advisable to place too much weight on the statistics so obtained. However, with respect to the 189 events identified as being of geophysical origin, it is clear that:

- the number of ten-second dumps in which naturally enhanced ion acoustic spectra occur is rare, as can be seen in Table 6.1,

No. of consecutive ten-sec dumps	1	2	3	4	5
No. of occurrences	54	39	13	2	2

Table 6.2 Details of lifetimes of occurrences of naturally enhanced ion-acoustic spectra.

- any geophysical cause is short-lived within the narrow beam of the radar. This explains that the reason they are not persistent could be because they move fast within a radar beam. They tend to occur in isolated ten-second dumps, as shown in Table 6.2,

- most occurrences of enhanced spectra are above 400 km altitude.

On examination of the data it is clear that the majority of the 189 events identified as being of geophysical interest are concentrated on eight days. There are three easily identifiable days in the 1998 data when there are a large number of naturally enhanced anomalous spectra compared with the other times. In the 1999 data there are five days when there are a significant number of occurrences of naturally enhanced anomalous spectra. At all other times any occurrences of such anomalous spectra are extremely rare i.e. no more than 2 occurrences in any day's data set which contains more than 2 hours of data. In the 2000 data there were only a few days in January when the radar beam was pointing in the field-aligned direction and none of these days showed a significant number of anomalous spectra which could clearly be assigned to be of geophysical interest at this stage.

The three times of interest in the 1998 data occur on 26th August and 24th and 25th September, whilst the five times in the 1999 data occur on 11th and 12th February, 2nd September and 3rd and 4th December. We now look at some of these in more detail.

6.2 Case Studies

6.2.1 Magnetic Storm of 26th August 1998

The Disturbance Storm-Time (Dst) Index is a useful means of observing magnetic storm behaviour. It is constructed by averaging the horizontal North/South (H) component of the geomagnetic field from mid-latitude and equatorial magnetograms. At these latitudes the magnetometer stations are not so close to the equator that the magnetic perturbations observed on the ground are dominated by the E-region equatorial electrojet. Hence the H component is dominated by the intensity of the magnetospheric ring current, which is directed westward and so produces a negative H perturbation at low latitude magnetometer stations (Kelley, 1989). The onset (or initial phase) of a storm is usually indicated by a sudden increase in the Dst index which is caused by the compression of the magnetosphere as a result of the arrival of a burst of solar plasma. This stage is followed by the main phase indicated by a large decrease in the Dst index due to the ring current. This phase may last up to a maximum of a day. It is then followed by the recovery stage in which the Dst index gradually returns to its normal level. This may last a few days.

We note the storm type behaviour of the Dst index in Figure 6.5 for 26th August 1998. This indicates that the storm started after 05:00:00 UT. On this day the anomalous echoes mainly occur from 03:40:00 to 03:53:00 UT, from 05:38:00 to 06:09:00 UT, from 07:10:00 to 08:03:00 UT and just before 10:00:00 UT which is before and during the onset and just before the main phase of the storm. We can see from the magnetogram data shown in Figure 6.6 that this coincides with an active period at Longyearbyen.

Figure 6.7 shows some typical spectra which were obtained on the morning of 26th August 1998. Where it was thought to be helpful, the power profile is also shown.

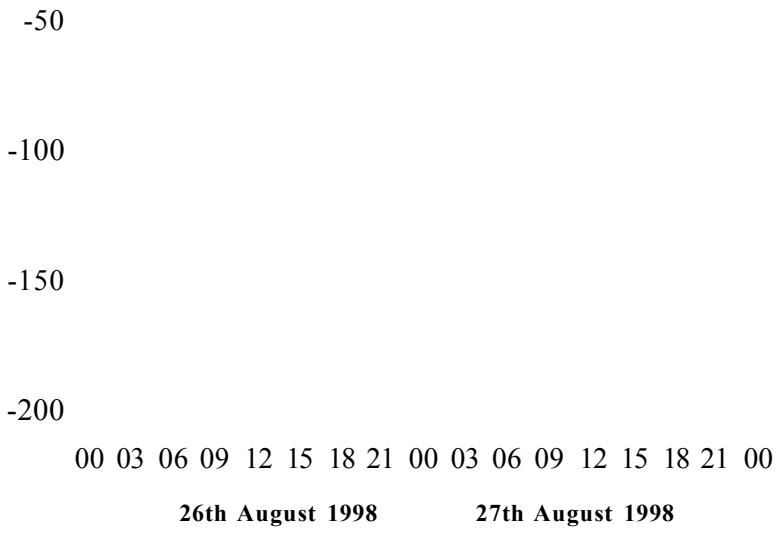

Figure 6.5: Dst indices for 26th and 27th August 1998.

26augl998

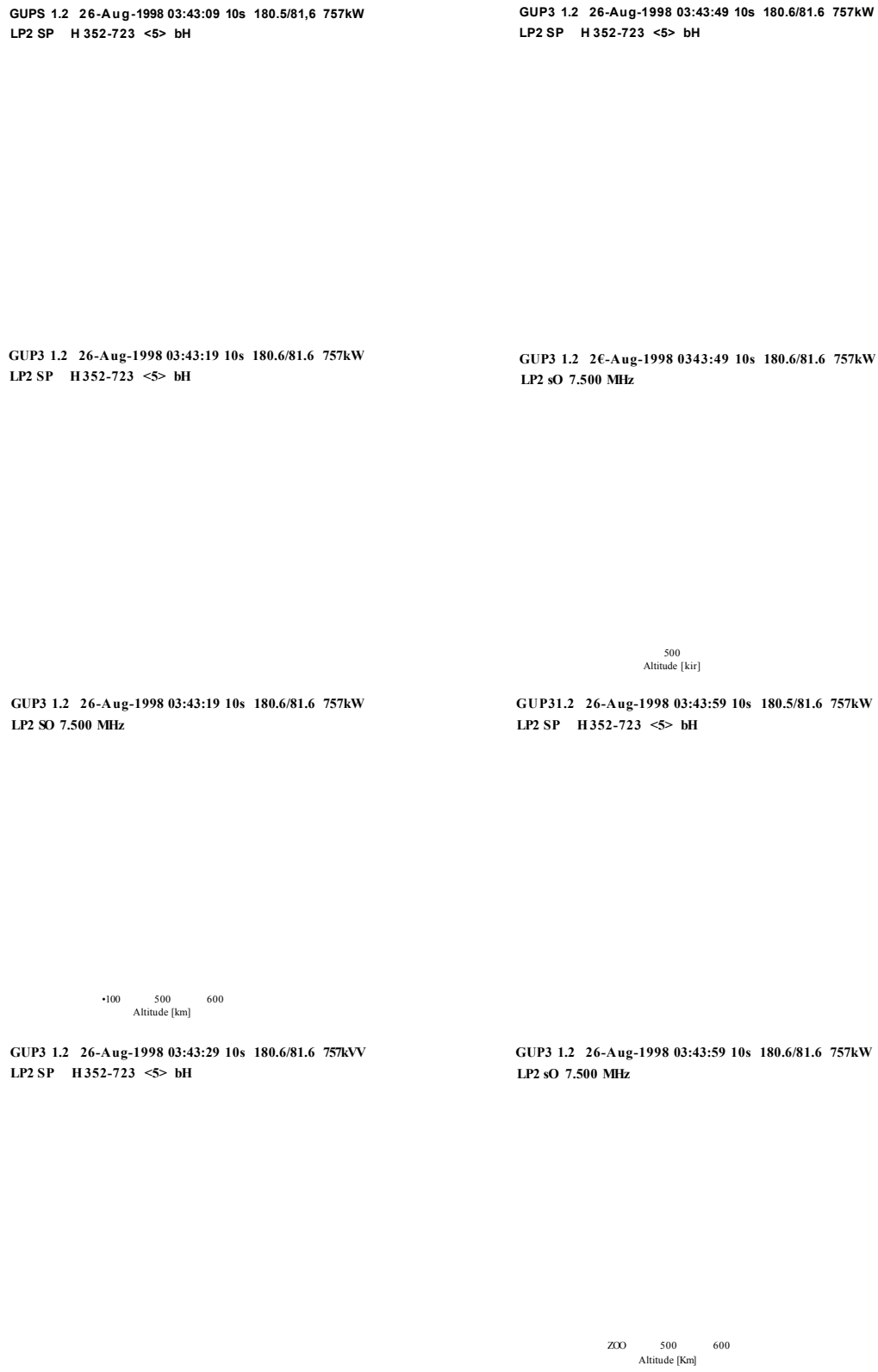

Figure 6.7: Two sequences of spectra which include examples of anomalous spectra which occur in the data of 26 August 1998.

We see quite dramatic changes in the appearance of the spectra over a period of less than one minute. Unfortunately, the simultaneous data from other instruments is limited for this event, so it is difficult to understand why the anomalous spectra should occur before the onset of the storm.

6.2.2 Magnetic Storm of 24th–25th September 1998

The September 25th 1998 event is a well-known storm about which a number of papers have already been published (Russell *et al.*, 1999; Moore *et al.*, 1999; Chi *et al.*, 2000; Strangeway *et al.*, 2000). However the papers concentrate on the measurements obtained by satellites and ground based magnetometers. They do not consider the effects, if any, that show in the radar spectra. The GUP3 ESR data shows there to be an unusually high number of asymmetric spectra between 18:24:00 and 19:17:00 UT on the 24th September and again between 00:00:00 and 00:10:00 on the 25th September. Some examples are shown in the Figures 6.8 and 6.9. We notice that most of the time it is the downshifted shoulder which is enhanced. Additionally the whole spectra tend to be displaced negatively from the mean, which indicates an ion outflow from the ionosphere.

The Dst index data is shown in Figure 6.10. Here we see evidence of the commencement of the magnetic storm as the Dst index increases just before midnight on the 24th September followed by the main phase of the storm during the early hours of 25th September. It is slightly surprising that many of the anomalous spectra occur in the data a few hours before the onset of the storm. However when we consider the H component of the magnetic field as shown in the two stack-plots in Figure 6.11 we see that there is some activity at Longyearbyen after 18:00:00 UT and again around midnight.

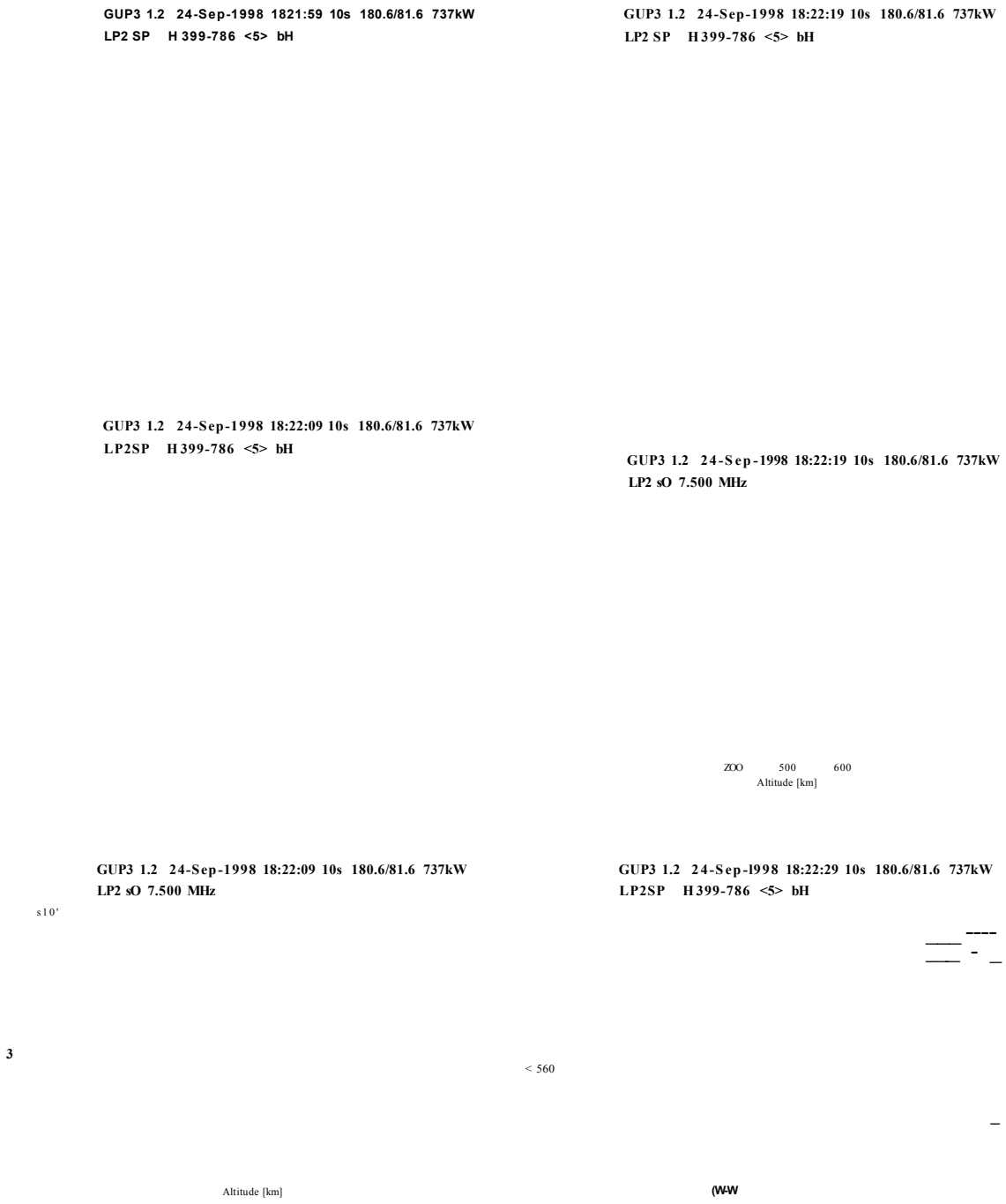

Figure 6.8: Examples of typical anomalous spectra which occur in the data dumps of 24th September 1998.

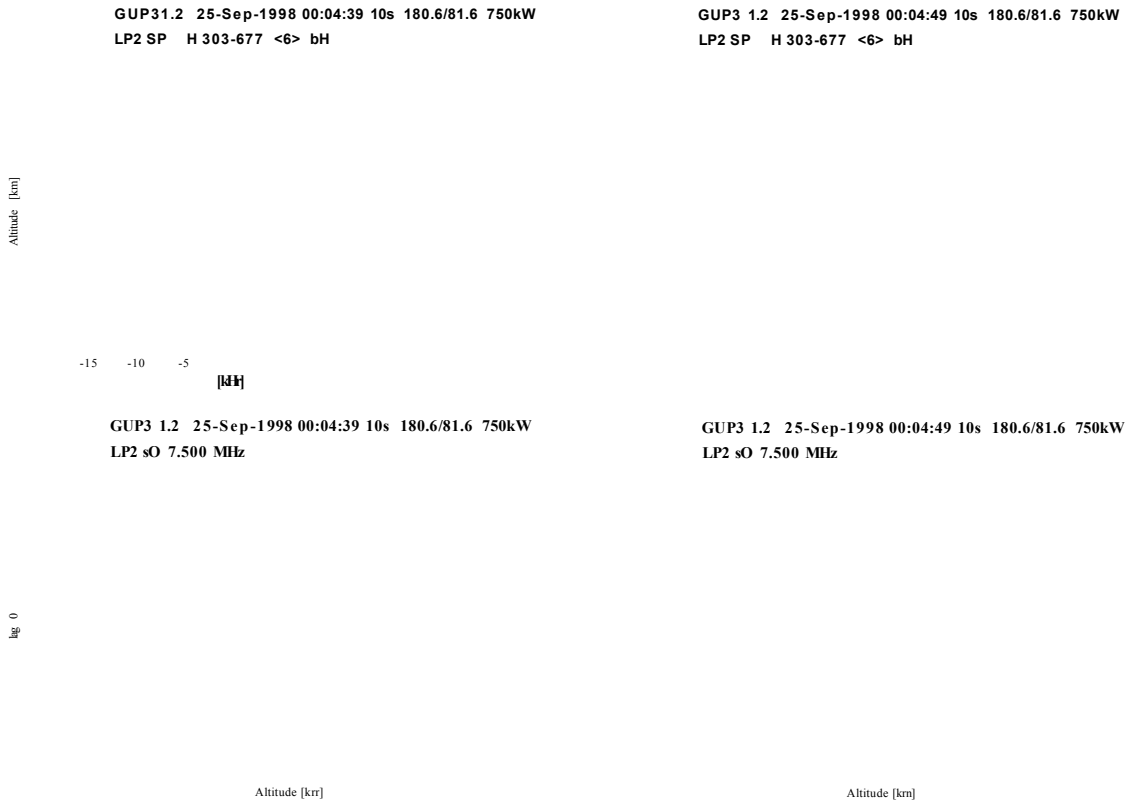

Figure 6.9: Examples of typical anomalous spectra which occur in the data dumps of 25th September 1998.

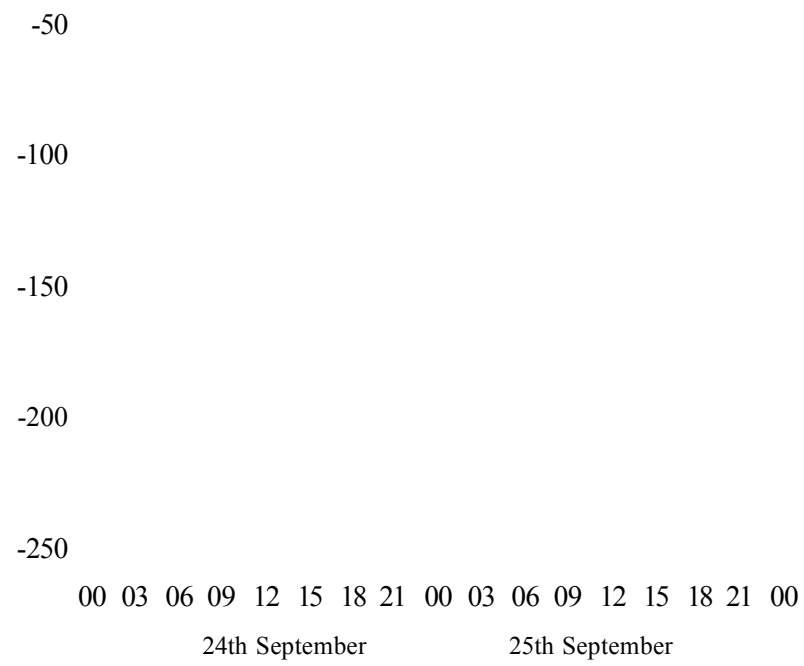

Figure 6.10: Dst indices for 24th and 25th September 1998.

24sep1998

t

24sep1998

The K-indices for 3-hour intervals, measured at Longyearbyen, are observed to be increasing from 5 to 7 for both of these events in August and September 1998. The anomalous spectra occur before the K-indices reach the peak average of 7, though care must be taken in using this information as the K-indices are averaged over 3 hourly intervals. Hence there may clearly be times within an interval when the value is significantly higher than the average value recorded.

The fact that the anomalous echoes occur at times of high magnetic activity is in agreement with the report by Rietveld *et al.* (1991).

We are now going to concentrate on three of the events from the 1999 data for which good simultaneous data exists from the meridian scanning photometer in Adventdalen. These are 11th and 12th February and 3rd December.

6.2.3 11th February 1999

Figure 6.12 shows examples of anomalous spectra found in two consecutive ten-second dumps on 11th February 1999. In these spectra we notice that although both shoulders are enhanced, the downshifted one is more prominent. The corresponding power profiles obtained show a lack of a sudden increase and decrease in power over a restricted 100 km range, making it clear that these events could not be due to satellites.

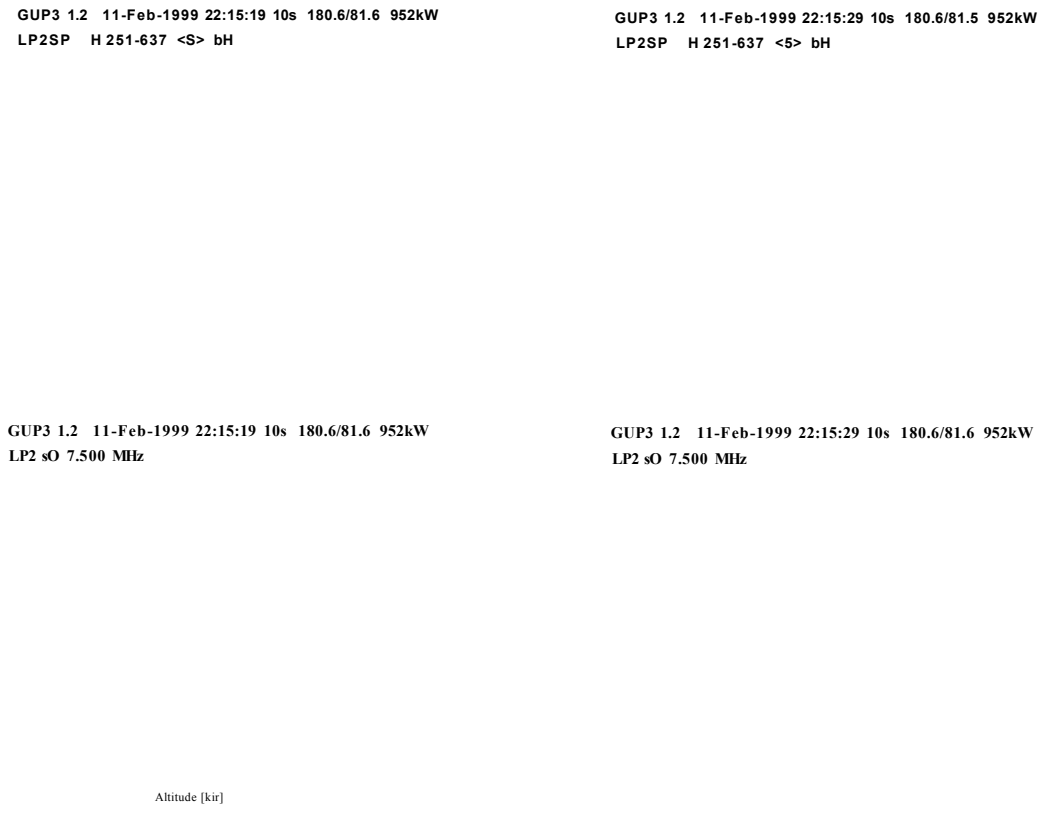

Figure 6.12: Examples of typical anomalous spectra which occur in the data dumps of 11th February 1999.

The meridian scanning photometer data for the day, 11th February 1999, is shown in the Figure 6.13. The panels show five different wavelengths of auroral emission. The top one is that of the red line (6300Å) oxygen emission arising primarily from precipitation of soft particles with energies around 500 eV. The second panel shows the blue line (4278Å) nitrogen emission, corresponding to energetic precipitation of at least 5 keV. The third panel shows the green line (5577Å) oxygen emission, again arising from relatively energetic precipitation of at least 2 keV. The fourth panel shows the emission at 4861Å, arising from proton precipitation. The bottom panel shows the 7320Å oxygen emission, which arises from soft particles with energies around 200 eV. Time runs along the x-axis. For each of the five panels, the y-axis is the elevation running from the southern to the northern horizon. As the ESR beam is pointing southward at an elevation of 81.6° during this experiment, the horizontal white lines shown in each of the panels represent a time history of the emission in the ESR field-of-view. The times at which the anomalous echoes appear correspond to the region indicated by the vertical white line around 22:15:00 UT.

We look at the detailed interpretation of the photometer data, in terms of the physics involved, later in section 6.3. Other anomalous spectra occur between 09:00:00 and 10:00:00 UT and between 11:30:00 and 11:35:00 UT, but unfortunately there is no meridian scanning photometer data available from Longyearbyen at this time.

During the event shown the echoes coincide with a particularly striking event, characterised by auroral emission at all of the wavelengths represented. We notice, however, that the emissions from the lower energy precipitation are much the strongest, while the emissions from the high energy precipitations are relatively weak.

The magnetometer data is shown in Figure 6.14. Here we notice that once again the anomalous spectra occur at times which are magnetically active at Longyearbyen.

LXR M5P, February 11 1999, Peak-Base

11feb1999

6.2.4 12th February 1999

The next example is from the following day, 12th February 1999. Figure 6.15 shows typical anomalous spectra measured in consecutive ten-second dumps which were seen in this set of data. Here we notice that the initial data dump shows the upshifted shoulder enhanced more strongly whilst the following data dump shows the downshifted shoulder to be the more prominent. The results in the two data dumps being so different from each other may be due to there being more than one event causing the anomalous spectra. These events may last for a shorter time period than the ten seconds and only occur in part of the radar beam's cross-section as suggested by Grydeland *et al.* (2003).

In the meridian scanning photometer data for this day shown in Figure 6.16 we notice the series of poleward-moving events. Once again the horizontal white lines represent a time history of the emission in the ESR field-of view. The first set of anomalous spectra are seen during the interval of time between the first two vertical white lines on the left, i.e. between 04:02:00 and 04:30:00 UT. Other times at which similar spectra are seen to occur are around the periods shown by the next two vertical white lines, i.e. 05:00:00 and 06:30:00 UT. Interestingly the anomalous spectra seem not to occur at the peaks of emission in these events. Other times at which anomalous spectra occur in this day's data set are 07:46:20 and 08:35:40 UT. Unfortunately the photometer data is not available at these times.

The magnetometer data shown in Figure 6.17 indicates that these are again magnetically active times at Longyearbyen. However, the Dst indices are plotted for both 11th and 12th February 1999 in Figure 6.18. The anomalous spectra for 11th February 1999 occur during the first significant rise in the Dst index and at the peak of the second rise in its value. On 12th February 1999 the anomalous spectra occur during the two occasions when the Dst index is changing from decreasing to increasing before the steady return to its normal value.

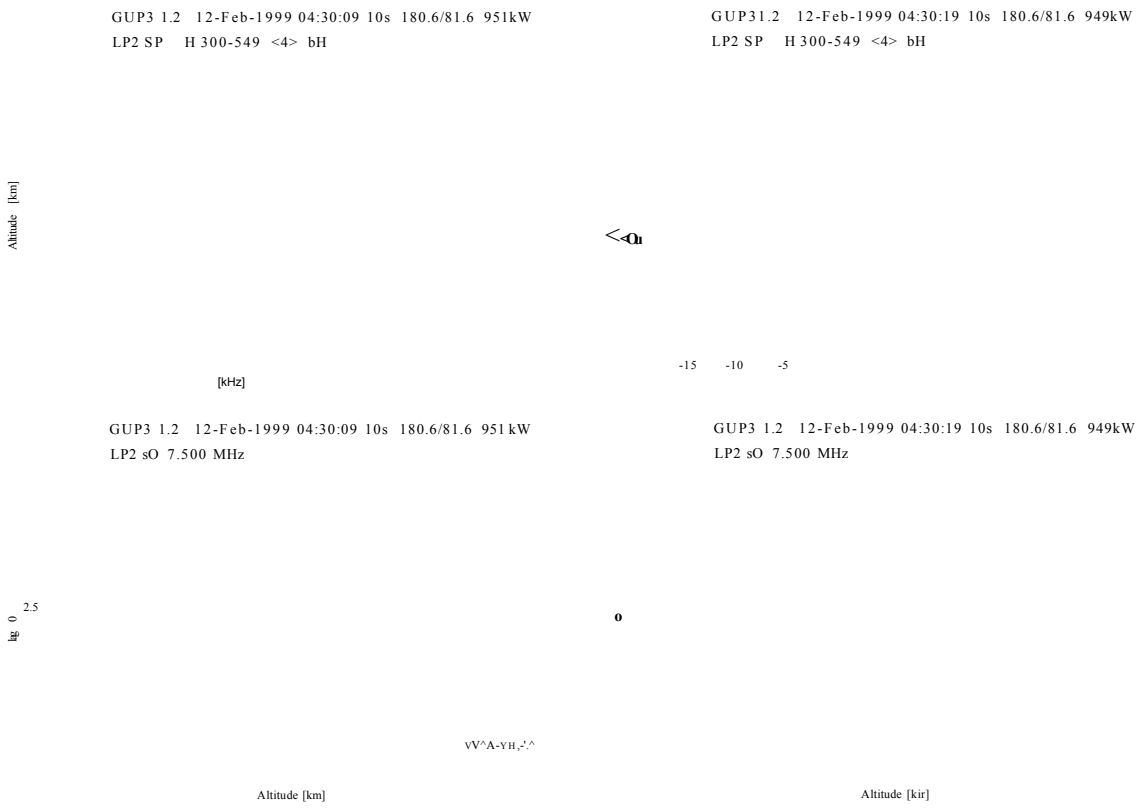

Figure 6.15: Examples of typical anomalous spectra which occur in the data dumps of 12th February 1999.

LYR MSP, February 12 1999, Peak-Base

OKI

12feb1999

12feb1999

Figure 6.18: Dst indices for 11th and 12th February 1999.

6.2.5 3rd December 1999

The anomalous spectra on 3rd December 1999 occur during the time intervals 09:42:00 to 10:03:00 UT and 10:55:00 to 11:00:00 UT. Some typical examples, which are not taken from consecutive data dumps, are shown in Figure 6.19. This time we notice that although both examples show spectra which have both shoulders enhanced it is the upshifted shoulder which is the more prominent in both cases. In addition the spectra are displaced negatively from the mean, as is the case with the spectra from the 25th September 1998 data, indicating an ion outflow.

The meridian scanning photometer data is shown in Figure 6.20. The anomalous echoes occur at times between the first two vertical white lines on the left and during the time period around the vertical white line on the right. These seem to be periods of enhanced 6300Å emission, but there is no strong association with periods of enhanced 5577Å emission, for example, even though this corresponds to more energetic precipitation.

The magnetometer data shown in Figure 6.21 again shows the relevant periods to be magnetically active, though there are other magnetically active periods when no anomalous spectra occur.

The Dst indices for this period are somewhat unusual in that they maintain a positive value throughout the previous day, 2nd December 1999, in spite of there being a tendency for the values to decrease from 13:00:00 UT onwards as seen in Figure 6.22. The anomalous spectra of 3rd December occur at the same time as the decrease in the Dst value.

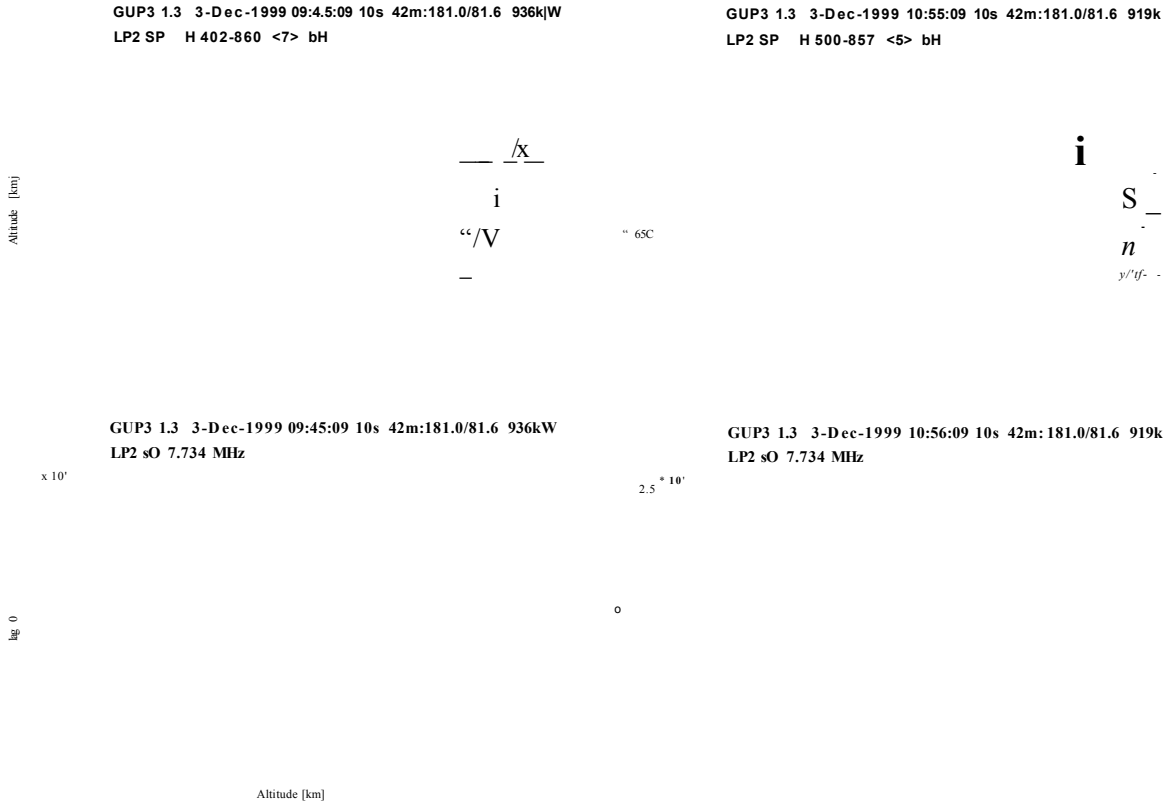

Figure 6.19: Examples of typical anomalous spectra which occur in the data dumps of 3rd December 1999.

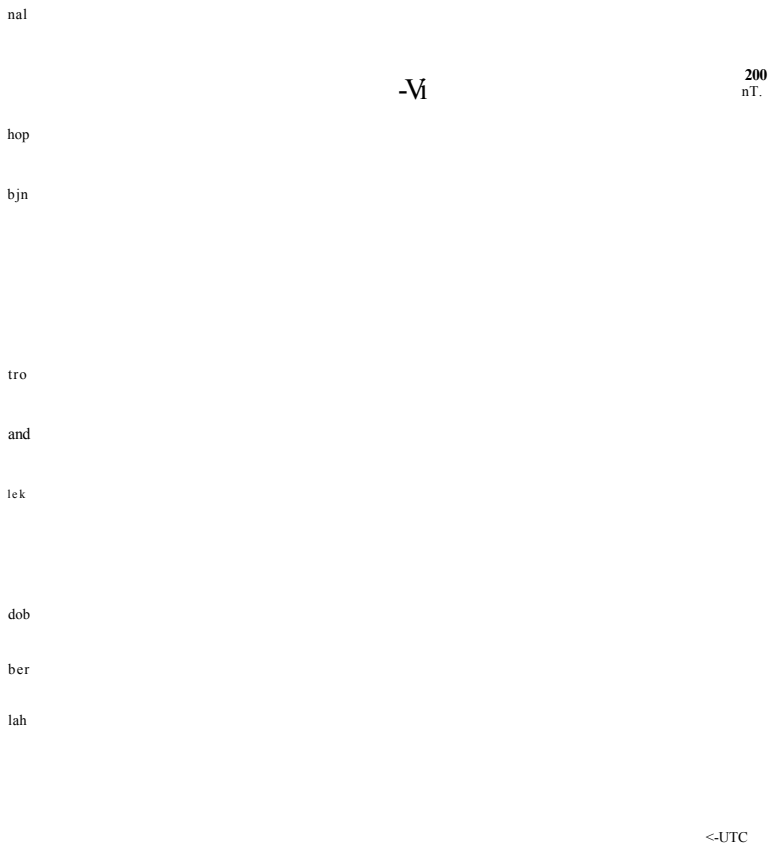

Figure 6.21: Magnetogram showing stack-plot of the H component of the magnetic field at various stations including Longyearbyen (lyb) on 3rd December 1999 obtained from http://geo.phys.uit.no/geomag.html

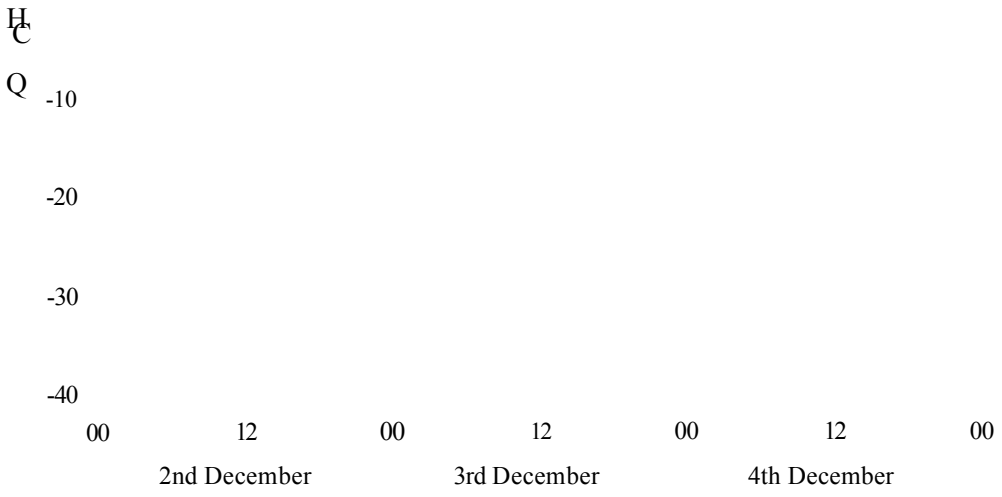

Figure 6.22: Dst indices for 2nd, 3rd and 4th December 1999.

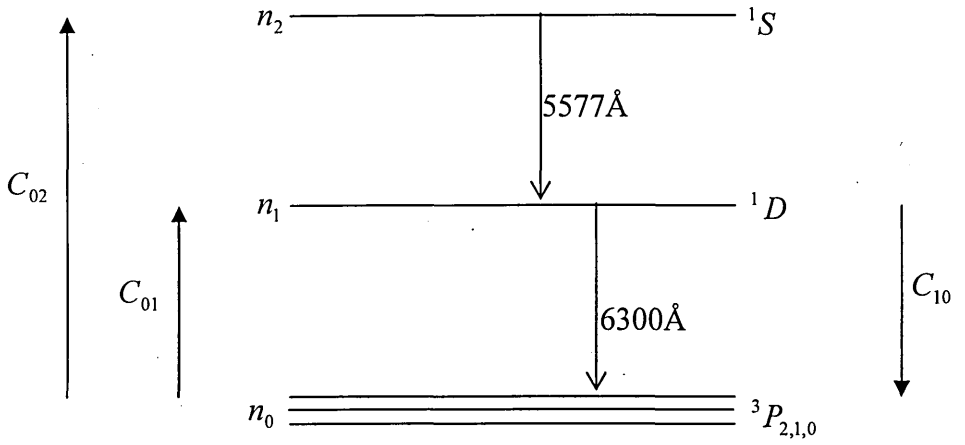

Figure 6.23: Schematic diagram of excitation levels of oxygen.

6.3 Proposed Atomic Model

Once we have identified the times at which the anomalous spectra occur in the data some attempt has been made to consider the geophysical conditions at these times. In particular the Dst indices, the H component of the magnetic field and, if available, the photometer data have been observed. The anomalous spectra seem to coincide with times of magnetic activity. They are most abundant in the hours before and during the onset of a magnetic storm.

Apart from the interest of matching up the anomalous echoes with the emission signatures in the photometer data, we have tried to use the photometer data in a quantitative way to tell us something about the ionospheric conditions under which these events occur. We look at the simplest possible model, that of excitation and decay of oxygen assuming thermal excitation. This gives a predicted "thermal" line intensity ratio which we can use as a benchmark for interpreting the observation. The model is therefore going to involve using the excitation levels of oxygen. These are shown as $^3P_{2,1,0}$, ^1D and ^1S in Figure 6.23.

We concentrate on the levels of oxygen emissions at 5577Å and 6300Å. The 6300Å emission arises from the decay of an oxygen electron excited onto the ^1D shell. The 5577Å emission arises from the decay of an electron from the more excited ^1S state. Information about the mechanisms involved can be found in Rees (1989). The emission intensity from each of these lines is proportional to the populations, n_1 and n_2, of electrons in these two excited states.

Let A_{ij} be the radiative decay rates from state *i* to state *j*. We are assuming that we only need to consider the values of A_{ij} for $i > j$, thus we are ignoring all photo-absorption processes such as sunlight, since the cases in which we are interested occur during the winter months at Longyearbyen. The values of A_{ij} used in our model are those from Galavis *et al.* (1997).

We also let $C_{ij}(T_e)$ be the collisional excitation or de-excitation rates from state *i* to state *j*. Here we also assume a linear combination of temperatures, so we have:

$$C_{ij} = rC_{ij}(T_{\text{thermal}}) + (1-r)C_{ij}(T_{\text{huge}})$$

where r = the fraction of the electron population, N_e, which is thermal,

T_{huge} = temperature representing the energy of incoming energetic particles.

The values of C_{ij} are calculated using the R-matrix method from Thomas *et al.* (1997).

Then,
the rate of change of population in each of the excited states = production – loss

This can be expressed in terms of a few important production/loss mechanisms for a collisionally dominated plasma as

$$\frac{dn_1}{dt} = n_0 N_e C_{01} + P^I + n_2(N_e C_{21} + A_{21}) - n_1\left[N_e(C_{10} + C_{12}) + A_{10} + L^I\right] \qquad (6.1)$$

and

$$\frac{dn_2}{dt} = n_0 N_e C_{02} + n_1 N_e C_{12} + P^{II} - n_2\left[N_e(C_{20} + C_{21}) + A_{21} + A_{20} + L^{II}\right] \qquad (6.2)$$

where P^I, P^{II}, L^I and L^{II} are other production and loss rates such as dissociative recombination and quenching as mentioned in Witasse *et al.* (1999).

For the ^1D level we have

$$P^I = N_e k_3[O_2^+] + k_6[N^*][O_2] + k_7[N^+][O_2]$$

and

$$L^I = l_1[N_2] + l_2[O_2] + l_3[O]$$

where

k_3 arises from the reaction	$O_2^+ + e_{th} \rightarrow O + O(^1D)$
k_6 arises from the reaction	$N(^2D) + O_2 \rightarrow NO + O(^1D)$
k_7 arises from the reaction	$N^+ + O_2 \rightarrow NO^+ + O(^1D)$
l_1 arises from the reaction	$O(^1D) + N_2 \rightarrow O + N_2$
l_2 arises from the reaction	$O(^1D) + O_2 \rightarrow O + O_2$
l_3 arises from the reaction	$O(^1D) + O \rightarrow O + O$

For the ^1S level we have

$$P^{II} = N_e k_{3'}[O_2^+] + k_{2'}[N_2][O]$$

and

$$L^{II} = l_{1'}[O_2] + l_{2'}[O]$$

where

k_3, arises from the reaction $O_2^+ + e_{th} \rightarrow O + O(^1S)$

k_2, arises from the reaction $N_2(A^3\Sigma_u^+) + O \rightarrow N_2 + O(^1S)$

l_1, arises from the reaction $O(^1S) + O_2 \rightarrow O + O_2$

l_2, arises from the reaction $O(^1S) + O \rightarrow O + O$

We now assume that there are no populations in higher states which could cascade downwards, so

$$n_0 = 1 - n_1 - n_2$$

We also assume that it is a steady state situation, so

$$\frac{dn_1}{dt} = \frac{dn_2}{dt} = 0$$

Hence equation (6.1) becomes

$$-n_1[N_e(C_{01} + C_{10} + C_{12}) + A_{10} + L^I] + n_2[N_e(C_{21} - C_{01}) + A_{21}] + N_e C_{01} + P^I = 0$$

which can be written as

$$-n_1 L_1 + n_2 Q_1 + P_1 = 0 \qquad (6.3)$$

where

$$L_1 = N_e(C_{01} + C_{10} + C_{12}) + A_{10} + L^I$$

$$P_1 = N_e C_{01} + P^I$$

and

$$Q_1 = N_e(C_{21} - C_{01}) + A_{21}$$

Similarly equation (6.2) becomes

$$n_1 N_e (C_{12} - C_{02}) - n_2 [N_e (C_{20} + C_{21} + C_{02}) + A_{21} + A_{20} + L^{II}] + N_e C_{02} + P^{II} = 0$$

which can be written as

$$n_1 Q_2 - n_2 L_2 + P_2 = 0 \qquad (6.4)$$

where

$$L_2 = N_e (C_{20} + C_{21} + C_{02}) + A_{21} + A_{20} + L^{II}$$

$$P_2 = N_e C_{02} + P^{II}$$

and

$$Q_2 = N_e (C_{12} - C_{02})$$

Eliminating n_2 from equations (6.3) and (6.4) we have

$$-n_1 (L_1 L_2 - Q_1 Q_2) + L_2 P_1 + P_2 Q_1 = 0$$

From which we obtain

$$n_1 = \frac{L_2 P_1 + P_2 Q_1}{L_1 L_2 - Q_1 Q_2} \quad \text{and} \quad n_2 = \frac{L_1 P_2 + P_1 Q_2}{L_1 L_2 - Q_1 Q_2}$$

Hence

$$\frac{n_1}{n_2} = \frac{L_2 P_1 + P_2 Q_1}{L_1 P_2 + P_1 Q_2}$$

Now the emission intensity of the 6300Å line, $I_{630.0} = A_{630.0} [O] n_1$

and the emission intensity of the 5577Å line, $I_{557.7} = A_{557.7} [O] n_2$

So the intensity ratio $\frac{I_{630.0}}{I_{557.7}} = \frac{A_{630.0}}{A_{557.7}} \frac{n_1}{n_2} = \frac{A_{630.0}}{A_{557.7}} \frac{L_2 P_1 + P_2 Q_1}{L_1 P_2 + P_1 Q_2}$

The model has been set up in an EXCEL spreadsheet (see Appendix E). Using parameters (N_e, T_e, T_i) from the analysed data for 3rd December 1999 about 20 minutes before the occurrence of the anomalous spectra the value for the intensity ratio obtained is 30.3. The digital photometer data was also obtained (Deehr, 2003) in the form of line intensities as a function of wavelength, time and angle from which we calculated the intensity ratio for the 98° scan. This is in approximately the same direction as that of the radar beam during the GUP3 experiment on the same day. The graph of these results is plotted in Figure 6.24. This suggests that the anomalous spectra have occurred in this set of data at the time when the intensity ratio has increased significantly. It can be seen that during most of the day the ratio was in the region of 1 or less but around 09:45:00 UT it increased to almost 6.

We predicted an intensity ratio of about 30 from the model, but the observations show a much lower figure. This suggests that either $O(^1S)$ is over-populated or $O(^1D)$ is under-populated according to our simple model. We cannot easily choose between these: our atomic model can predict the absolute intensity of each line as photons $m^{-3}\ s^{-1}$, but the photometer data comes from a ground-based vertical slice, so cannot compare absolute intensity as it would vary with height. Most likely the highest state $O(^1S)$ is being excited by non-thermal high energy electrons or ions not accounted for in our simple model. However, during an event the observed ratio rises an order of magnitude due to $I_{630.0}$ rising more than $I_{557.7}$. Curiously this enhanced ratio tends towards our modelled prediction, indicating perhaps that thermal collisional processes may start to play a greater role in the oxygen excited state population.

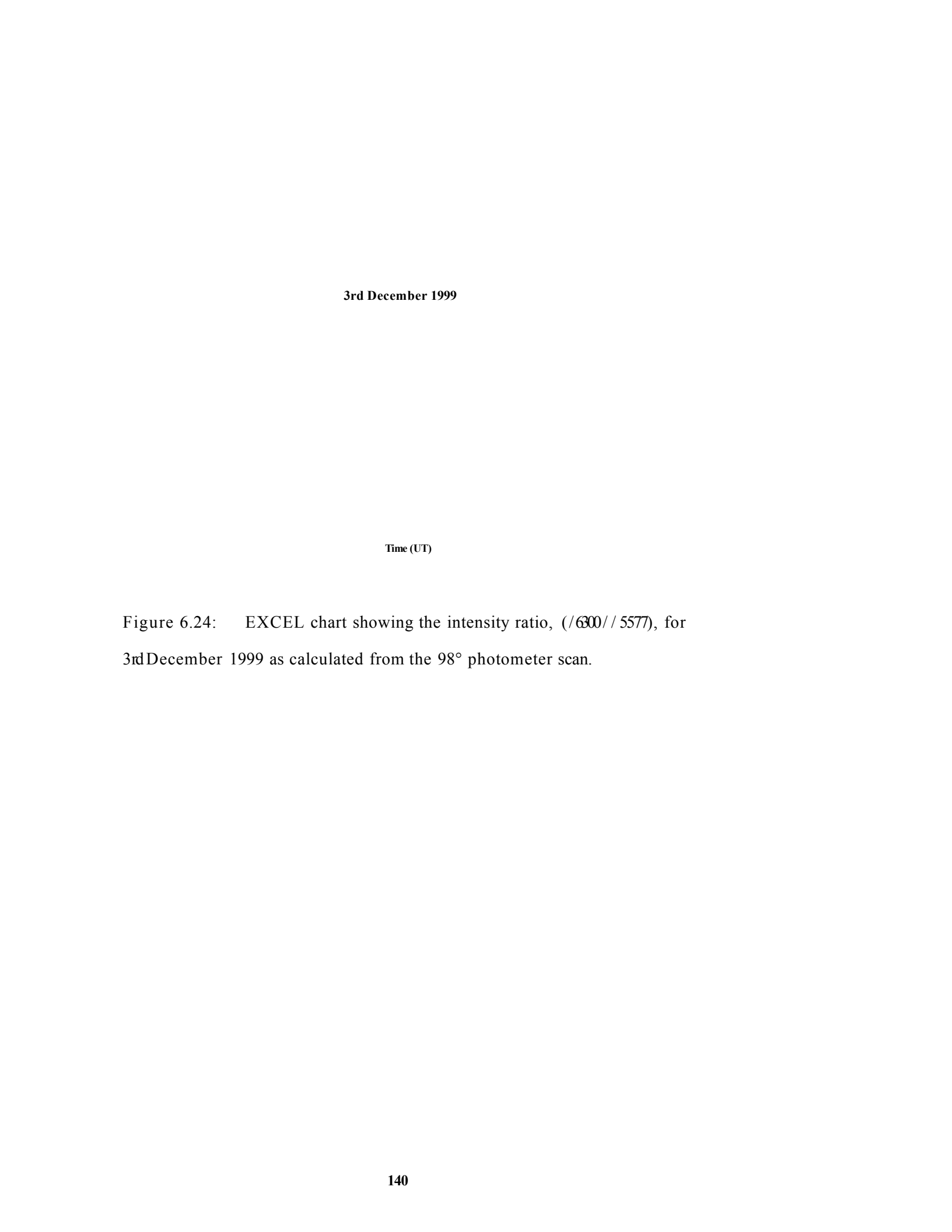

Figure 6.24: EXCEL chart showing the intensity ratio, (/6300//5577), for 3rd December 1999 as calculated from the 98° photometer scan.

So the model could not be tested against this data. The data for 12th February shows the intensity ratio has increased at the times of the anomalous spectra, but not as much as is the case with the 3rd December data.

The data for 11th and 12th February 1999 have also been obtained. The EXCEL charts showing the intensity ratios are shown in Figures 6.25 and 6.26. Unfortunately the data obtained for 11th February 1999 did not cover the period of interest when a particularly striking event appears to have occurred in the colour plots in Figure 6.13.

At present this is a simplified model containing many assumptions. It is still in its early stages, and more work needs to be done to improve its reliability before we are able to state any conclusions with confidence.

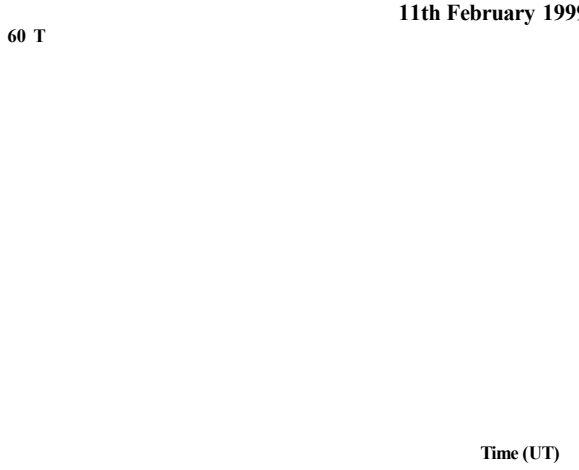

Figure 6.25: EXCEL chart showing the intensity ratio, (/6300/15577), for 11th February 1999 as calculated from the 98° photometer scan.

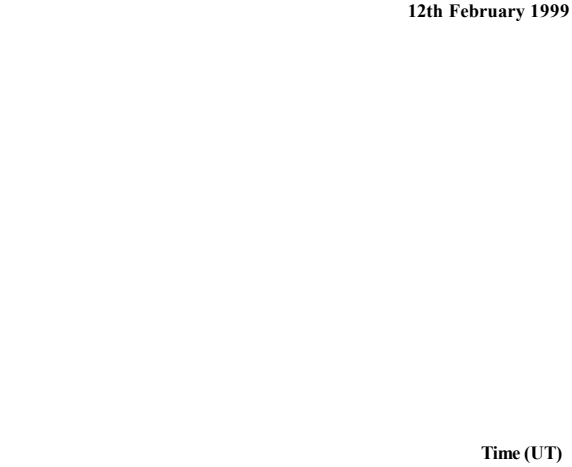

Figure 6.26: EXCEL chart showing the intensity ratio, (/6300//5577), for 12th February 1999 as calculated from the 98° photometer scan.

Chapter 7

Conclusions

7.1 Satellites

As reported in Porteous *et al.* 2003, a substantial amount of raw data from the EISCAT Svalbard Radar has been studied in order to find a method for identifying likely causes of enhanced spectra. It was suspected that many of the cases found were due to satellites or space debris passing through the main beam or the side lobes. An automated routine was therefore developed and used to identify those times at which enhanced spectra occurred.

It has been shown that examining the variation of power with range can give a good indication of whether the spectra are caused by satellites or are possibly of a geophysical nature. In the ESR GUP3 experiment, which contains both long pulse and alternating code data, enhancements in the power profiles of both modulations are noted when satellites appear. A threshold increase of 20% in the returned power was used to help divide the cases into two classes. Situations in which the returned power

Range (km)	Number of satellites	Number of possibly naturally enhanced spectra
<600	2	1
600–750	7	5
>750	15	10

Table 7.1: The number of satellites and possibly naturally enhanced spectra found in the region covered by the ESR beam for 10:11:30 to 13:00:00 UT on 1st December 1999.

showed an increase of 20% or more were classed as being due to satellites or space debris whilst those which showed a smaller increase in power could be considered as possible cases for further investigation relating to a possible geophysical cause. On this basis, it is possible to use an automated program to distinguish between such cases. A small number of noisy spectra are identified by the program and have to be eliminated.

In the period 10:11:30 to 13:00:00 UT on 1st December 1999 it was found that the numbers of satellites and possibly naturally enhanced spectra occurring in the region covered by the ESR radar beam were as given in Table 7.1. It can be seen from these results that there were on average about eight satellites per hour passing through the radar beam.

The routine was tested using further data from 2nd and 3rd December 1999 and similar results were obtained. It was simple to verify that satellites at too great a distance, such as that predicted at 12:08:21 UT with a range of 871 km, were not detected by the radar. Similarly, those at too large an angle from the beam centre, such as that

predicted at 11:55:30 UT at an angular distance of 6.319°, were not detected. This gives some insight into the area within which the beam at Svalbard could detect satellite contamination. Further work needs to be carried out to provide greater refinement.

Since there were a small number of times when probable satellites were detected by the automated program, but when no satellites were found using the tracking program, there is scope for further studies in this area. This may, for example, mean checking the positions of a larger number of satellites or items of space debris by including those which have a greater perigee than 900 km. Although the returned signal is interpreted as coming from a specific altitude, it is possible for the signal to be returned as a result of reflection from a hard target at a much greater range and the hardware to have interpreted it as having come for a much closer region.

Following on from the work done in identifying satellites in the radar beam, we have identified times when the anomalous spectra appear to be caused by geophysical phenomena by eliminating the enhanced spectra where the peaks occur with a Doppler shift between – 4.5 and + 4.5 kHz. This resulted in considerably fewer situations having to be manually checked. Further work could be carried out to enable some of the remaining cases to be eliminated automatically by checking the distance between the increase and decrease in power. Since only those cases where this distance is greater than 100 km need to be examined further.

Since there are a large number of satellites, or items of space debris, orbiting the earth and therefore likely to pass through the beams of incoherent scatter radars, care must be made to distinguish between the spectra caused by such objects and those arising from geophysical conditions. This applies not only to the ESR data, but for any radar data.

Further studies still need to be performed at the times of those anomalous echoes not automatically rejected as being due to satellite contamination, to determine whether or not these are genuinely of a geophysical nature. Since the occurrence of enhanced spectra due to geophysical conditions is not necessarily frequent, automated search routines of the type described here provide the scope for extracting such data from very large extended data sets and hence assisting in the investigation of naturally enhanced spectra and their causes.

It would be interesting to make appropriate changes to the automated program so that the actual frequencies at which both peaks occur are noted in all situations. This would involve using the idea of the change in sign of the gradient of the spectra when proceeding from left to right along the curve.

Further work is needed if an automated method is to be found for filtering contamination due to satellites and small items of space debris from the AC data, which is more noisy in nature, but which has a greater height resolution.

7.2 Naturally Enhanced Ion Acoustic Spectra

Using the automated program, the CP data for the GUP3 experiment during 1998–2000 has been searched for incidents of naturally enhanced ion acoustic spectra. It has been possible to identify a number of days when anomalous spectra occur. The most intense periods were two events in the 1998 data, 26th August and 24th–25th September. Both of these events occurred during and preceding the onset of a particularly impressive magnetic storm resulting from a coronal mass ejection. There were no events in the remainder of the data in which the frequency of occurrence of naturally enhanced ion acoustic spectra came close to matching that of these two events. However, there were some time periods in which these rare occurrences did

happen with increased frequency. These were all recorded in the 1999 data sets on 11th and 12th February, 2nd September, and 3rd and 4th December. Of these the graphical photometer data is available at the web site

http://haldde.unis.no/msp.htm

for 11th and 12th February and 3rd December. The enhanced spectra on these days always occurred during periods of increased magnetic activity at Longyearbyen as is shown by the magnetometer data recorded at Adventdalen close to the ESR site.

A tentative model has been used to consider the thermal energies required to generate the intensity ratio of 6300Å/5577Å emission. The spectra seem to occur when the intensity ratio is over 3. To date a ratio of 30.3 has been obtained using the model, whereas less than 6 is obtained in practice. Many of the parameters used in the model are estimates and this is clearly an area which needs further attention.

This research does seem to suggest that the anomalous spectra are not necessarily a result of collisional or Joule heating as was indicated by Jones *et al.* (1990). It is more likely that they are a response to a sudden influx of solar particles

It is important that in the future the radars provide as great a coverage of the time as possible as it is necessary to obtain simultaneous data from a range of different sources in order to obtain the required variety of parameters for a complete physical/chemical model.

Bibliography

Appleton, E.V. and Barnett, M.A.F.: "On some direct evidence for downward atmospheric reflection of electric rays", Proceedings of the Royal Society, A109, pp. 621–641, 1925.

Beynon, W.J.G. and Williams, P.J.S.: "Incoherent scatter of radio waves from the ionosphere", Reports on Progress in Physics, Vol. 41, pp. 909–955, June, 1978.

Bowles, K.L.: "Observation of vertical-incidence scatter from the ionosphere at 41 Mc/sec", Physical Review Letters, Vol. 1, pp. 454–455, 1958.

Brekke, A.: "Physics of the upper polar atmosphere", John Wiley & Sons, 1997.

Breit, G. and Tuve, M.: "A test of the existence of the conducting layer", Physical Review, Vol. 208, pp. 554–573, 1926.

Buchert, S.C., van Eyken A.P., Ogawa T. and Watanabe S.: "Naturally enhanced ion-acoustic lines seen with the EISCAT Svalbard radar", Advanced Space Research, Vol. 23, No. 10, pp.1699–1709, 1999.

Bugoslavskya, N.Ya.: "Solar activity and the ionosphere for radio communications specialists", Pergamon Press, 1962.

Buonsanto, M.J., Sipler, D.P., Davenport, G.B. and Holt, J.M.: "Estimation of the O^+, O collision frequency from radar and Fabry-Perot observations at Millstone Hill", Journal of Geophysical Research, Vol.102, No. A8, pp. 17267–17274, 1997.

Cabrit, B. and Opgenoorth H.: "Comparison between EISCAT UHF and VHF backscattering cross section", Journal of Geophysical Research, Vol.101, No. A2, pp. 2369–2374, 1996.

Cairns, I.H.: "A theory for the Langmuir Waves in the electron forshock", Journal of Geophysical Research, Vol. 92, No. A3, pp. 2329–2342, March 1, 1987.

Chen, F.F.: "Introduction to plasma physics", Plenum Press, 1984.

Chi, P.J., Russell, C.T., Musman, S., Peterson, W.K., Le, G., Angelopoulos, V., Reeves, G.D., Moldwin, M.B. and Chun, F.K.: "Plasmaspheric depletion and refilling associated with the September 25, 1998 magnetic storm observed by ground magnetometers at L = 2", Geophysical Research Letters, Vol. 27, No. 5, pp 633–636, March 1, 2000.

Collis, P.N., Häggström, I., Kaila, K. and Rietveld, M.T.: "EISCAT radar observations of enhanced incoherent scatter spectra; their relation to red aurora and field-aligned currents", Geophysical Research Letters, Vol. 18, No. 6, pp 1031–1034, June 1991.

Davies, K.: "Ionospheric radio", IEE Electromagnetic Waves Series 31, Peter Peregrinus Ltd., 1990.

Deehr, C., private communication, 2003.

Dougherty, J.P.and Farley, D.T.: "A theory of incoherent scattering of radio waves by a plasma", Proceedings of the Royal Society, A259, pp. 79–99, 1960.

Evans, J.V.: "Theory and practice of ionosphere study by Thomson scatter radar", Proc.IEEE, Vol. 57, pp. 496–530, 1969.

Fejer, J.A.: "Scattering of radio waves by an ionized gas in thermal equilibrium", Canadian Journal of Physics, Vol. 38, pp. 1114–1133, 1960.

Fejer, J.A.: "Ionospheric modification and parametric instabilities", Reviews of Geophysics and Space Physics, Vol. 17, No. 1, pp. 135–153, 1979.

Forme, F.R.E.: " A new interpretation on the origin of enhanced ion acoustic fluctuations in the upper ionosphere", Geophysical Research Letters, Vol. 20, No. 21, pp 2347–2350, November 5, 1993.

Forme, F.R.E.: "Parametric decay of beam-driven Langmuir Wave and ion-acoustic fluctuations in the ionosphere: a weak turbulence approach" Annales Geophysicae, Vol. 17, No. 9, pp. 1172–1181, 1999.

Forme, F.R.E. and Fontaine, D.: "Enhanced ion acoustic fluctuations and ion outflows", Annales Geophysicae, Vol. 17, No.2, pp. 182–189, 1999.

Forme, F.R.E., Fontaine, D. and Wahlund, J.E.: "Two different types of enhanced ion acoustic fluctuations observed in the upper ionosphere", Journal of Geophysical Research, Vol. 100, No. A8, pp. 14625–14635, August 1, 1995.

Forme, F.R.E., Ogawa, Y. and Buchert, S.C.: "Naturally enhanced ion acoustic fluctuations seen at different wavelengths", Journal of Geophysical Research, Vol. 106, No. A10, pp. 21503–21515, October 1, 2001.

Foster, J.C., del Pozo, C. and Groves, K.: "Radar observations of the onset of current driven instabilities in the topside ionosphere", Geophysical Research Letters, Vol. 15, No. 2, pp. 160–163, February, 1988.

Galavis, M.E., Mendoza, C. and Zeippen, C.J.: "Radiative rates for forbidden transitions within the ground configuration of ions in the carbon and oxygen isoelectronic sequences", Astronomy and Astrophysics Supplement Series, Vol. 123, No. 1, pp. 159–171, 1997.

Grydeland, T., La Hoz, C., Hagfors, T., Blixt, E.M., Saito, S., Strømme, A. and Brekke, A.: "Interferometric observations of filamentary structures associated with plasma instability in the auroral ionosphere", Geophysical Research Letters, Vol. 30, No. 6, 2003.

Hagfors, T.: "Density fluctuations of a plasma in a magnetic field with applications to the ionosphere,", Journal of Geophysical Research, Vol. 66, pp. 1699–1712, 1961.

Hargreaves, J.K.: "The solar-terrestrial environment", C.U.P., 1995.

Hierl, P.M., Dotan, I., Seeley, J.V., Doren, J.M., Morris, R.A. and Viggiano, A.A.: "Rate constants for the reactions of O^+ with N_2 and O_2 as a function of temperature (300–1800K)", Journal of Chemical Physics, Vol. 106, No. 9, pp. 3540–3544, March, 1997.

Jones, G.O.L., Williams, K.J. and Lockwood, M.: "Characteristics of the high-latitude trough", Advanced Space Research, Vol. 10, No. 6, pp. 191–196, 1990.

Jones, G.O.L., Williams, P.J.S., Winser, K.J., Lockwood, M. and Suvanto, K.: "Large plasma velocities along the magnetic field line in the auroral zone", Nature, Vol. 336, November 17, 1988.

Kelley, M.C., "The Earth's Ionosphere", Academic, San Diego, Calif., 1989.

Kindel, J.M. and Kennel, C.F.: "Topside Current Instabilities", Journal of Geophysical Research, Vol. 76, No. 13, pp. 3055–3078, 1971.

Moore, T.E., Peterson, W.K., Russell, C.T., Chandler, M.O., Collier, M.R., Collin, H.L., Craven, P.D., Fitzenreiter, R., Giles, B.L. and Pollock, C.J.: "Ionosphereic mass ejection in response to a coronal mass ejection", Geophysical Research Letters, Vol. 26, No. 15, pp. 2339–2342, 1999.

Porteous, J., Samson, A.M., Berrington, K.A. and McCrea, I.W.: "Automated Detection of Satellite Contamination in Incoherent Scatter Radar Spectra", Annales Geophysicae, Vol. 21, No. 5, pp. 1177–1182, 2003.

Ratcliffe, J.A. "An introduction to the ionosphere and magnetosphere", C.U.P., 1972.

Rees, M.H.: "Physics and chemistry of the upper atmosphere, C.U.P., 1989.

Rietveld, M.T., Collis, P.N., Eyken, A.P. and Lovhaug, U.P.: "Coherent echoes during EISCAT UHF Common Programmes", Journal of Atmospheric and Terrestrial Physics, Vol. 58, pp. 161–174, 1996.

Rietveld, M.T., Collis, P.N. and St.-Maurice, J.-P.: "Naturally enhanced ion acoustic waves in the auroral ionosphere observed with the EISCAT 933-MHz Radar", Journal of Geophysical Research, Vol. 96, No. A11, pp. 19291–19305, November 1, 1991.

Rishbeth, H. and Williams, P.J.S.: "The EISCAT ionospheric radar: the system and its early results", Q. JI R. astr. Soc. 26, pp. 478–512, 1985.

Rosenbluth, M.N. and Rostoker, N.: "Scattering of electromagnetic waves by a non-equilibrium plasma", Phys of Fluids, Vol. 5, pp. 776–788, 1962.

Russell, C.T., Zhou, X.W., Chi, P.J., Kawano, H., Moore, T.E., Peterson, W.K., Cladis, J.B., and Singer, H.J.: "Sudden compression of the outer magnetosphere associated with an ionospheric mass ejection", Geophysical Research Letters, Vol. 26, No. 15, pp. 2343–2346, 1999.

Salpeter, E.E.: "Electron Density Fluctuations in a Plasma", Physical Review, Vol. 120, pp. 1528–1535, 1960.

Sedgemore-Schulthess K.J.F., private communication, 2002

Sedgemore-Schulthess, K.J.F., Lockwood, M., Trondsen, T.S., Lanchester, B.S., Rees, M.H., Lorentzen, D.A. and Moen, J.: "Coherent EISCAT Svalbard Radar spectra from the dayside cusp/cleft and their implications for transient field-aligned currents", Journal of Geophysical Research, Vol. 104, No. A11, pp. 24613–24624, 1 Nov, 1999.

Sedgemore-Schulthess, K.J.F. and St-Maurice, J.-P.: "Enhanced ion-acoustic spectra and their interpretation", Surveys in Geophysics, Vol. 22, No. 1, pp. 55–92, 2001.

Smart, W.M.: "Text-book on spherical astronomy", C.U.P., 1960.

St-Maurice, J.-P. and Schunk. R.W.: "Ion velocity distributions in the high-latitude ionosphere", Reviews of Geophysics and Space Physics, Vol. 17, No. 1, pp. 99–134, 1979.

Strangeway, R.J., Russell, C.T., Carlson, C.W., McFadden, J.P., Ergun, R.E., Temerin, M., Klumpar, D.M., Peterson, W.K. and Moore, T.E.: "Cusp field-aligned currents and ion outflows", Journal of Geophysical Research, Vol. 105, No. A9, pp. 21129–21142, 1 2000.

Thomas, M.R.J., Bell, K.L. Berington, K.A.: "Electron-impact excitation of neutral atomic oxygen ($^3P - {}^1D$, $^3P - {}^1S$, $^1D - {}^1S$ transitions)", Journal of Physics B: Atomic, Molecular and Optical Physics, Vol. 30, No. 20, pp. 4599–4608, 1997.

Wahlund, J.E., Forme, F.R.E., Opgenoorth, H.J. and Persson, M.A.L.: "Scattering of electromagnetic waves from a plasma: enhanced ion acoustic fluctuations due to ion-ion two-stream instabilities", Geophysical Research Letters, Vol. 19, No. 19, pp 1919–1922, October 2, 1992a.

Wahlund, J.E., Opgenoorth, H.J., Forme, F.R.E., Persson, M.A.L., Häggström, I. and Lilensten, J.: "Electron energisation in the topside auroral ionosphere: on the importance of ion-acoustic turbulence", Journal of Atmospheric and Terrestrial Physics, Vol. 55, No. 4/5, pp. 623–645, 1993.

Wahlund, J.E., Opgenoorth, H.J., Häggström, I., Winser, K.J. and Jones, G.O.L.: "EISCAT observations of topside ion outflows during auroral activity: revisited", Journal of Geophysical Research, Vol. 97, No. A3, pp. 3019–3037, March 1, 1992b.

Wannberg, G., Wolf, I., Vanhainen, L.-G., Koskenniemi, K., Röttger, J., Postila, M., Markkanen, J., Jacobsen, R., Stenberg, A., Larsen, R., Eliassen, S., Heck, S. and Huuskonen, A.: "The EISCAT Svalbard Radar: a case study in modern incoherent scatter radar system design", Radio Science, Vol. 32, No. 6, pp. 2283–2307, November–December, 1997.

Williams, P.: "European radar unscrambles the ionosphere", New Scientist, 5 December, 1985.

Witasse, O., Lilensten, J., Lathuillère, C. and Blelly, P.-L.: "Modeling the OI 630.0 and 557.7 nm thermospheric dayglow during EISCAT-WINDII coordinated

measurements", Journal of Geophysical Research, Vol. 104, No. A11, pp. 24639–24655,November 1, 1999.

Appendix A

'iaspec' program obtained from Francis Sedgemore-Schulthess

```
      program iaspec

c Program to compute ion-acoustic spectra for drifting electrons and
two
c non-drifting ions with arbitrary ratios of Te/Ti. Uses Maxwellian
c descriptions only. Main inputs are: Ne, Te, Ti, Ve, and radio
frequency
c density. Based on an algorithm of Jean-Pierre St-Maurice (1987).
c This program conforms to at least ANSI Fortran 77 standards, and
contains
c no calls to compiler-specific functions or external libraries. It
can
c therefore be compiled simply with the following command:

c     $ f77 -o iaspec iaspec.f

c where $ is the operating system prompt. The devlopment system was a
c Pentium class processor running GNU/Linux 2.2-2.4 and the G77
compiler.

c The program prompts for, and then reads, a number of numeric input
c parameters from STDIN. When run repetively, these may be better
placed
c into a plain ASCII file, with one parameter per line. The program
would
c then be run in the following manner:

c     $ iaspec < INPUT.DAT

c where INPUT.DAT is the input parameter file.

c This program is free software; you can redistribute it and/or
c modify it under the terms of the GNU General Public License
c as published by the Free Software Foundation; either version 2
c of the License, or (at your option) any later version.

c This program is distributed in the hope that it will be useful,
c but WITHOUT ANY WARRANTY; without even the implied warranty of
c MERCHANTABILITY or FITNESS FOR A PARTICULAR PURPOSE. See the
c GNU General Public License for more details.

c You should have received a copy of the GNU General Public License
c along with this program; if not, write to the Free Software
c Foundation, Inc., 59 Temple Place - Suite 330, Boston,
c MA 02111-1307, USA.

c Copyright (c) Jean-Pierre St-Maurice, 1987; Francis Sedgemore,
1999-2001

c Contact: Dr Francis Sedgemore
c          Danish Space Research Institute
c          Juliane Maries Vej 30
c          DK-2100 København Ø
c          Denmark
c          Tel: +45 35 32 57 81 / 35 32 58 30
c          Fax: +45 35 36 24 75 (DSRI)
c          Email: ffransis@dsri.dk

c Initial edit:  Francis Sedgemore, 10/8-99
c Last revision: kjfs 13/12-01
```

```
c Parameter and array declarations.

      parameter (isiz=260)
      dimension
a1(isiz),a2(isiz),a3(isiz),b1(isiz),b2(isiz),b3(isiz),
     @          e1(isiz),e2(isiz),e3(isiz)

c Define the constants used. The calculation is done in CGS units,
for want of
c the effort required to re-work the algorithm in MKS.

c ELCH = electron charge (stat Coulombs)
c AMASE = electron mass (g)
c AMASP = proton mass (g)
c BOLTZ = Boltzmann constant (ergs/K)
c VLIGHT = light speed in vacuo (cm/s)

      data elch,amase,amasp,boltz,vlight,pi/4.810e-10,9.109e-28,
     @     1.673e-24,1.380e-16,2.998e10,3.1415927/

c Read the input parameters from STDIN. These are:

c NTOT = number of points in positive frequency range (max=isiz)
c NLIM = number of points for computation (max=isiz)
c ENDF = end frequency of spectrum (kHz)
c PHI = angle between wave vector and B field (deg)
c AMAGF = magnetic field (Gauss)
c WINC = incident radio frequency (MHz)
c TE = electron temperature (K)
c ANOMN = electron density (m^-3)
c VDPAR = parallel drift (kms^-1)
c AIMASA = normalised mass of ion species A
c AIMASB = normalised mass of ion species B
c TEMIA = temperature of ion species A (K)
c TEMIB = temperature of ion species B (K)
c FRA = fraction of ion species A

      write(*,*)
      write(*,*) 'Number of points in positive frequency range?'
      read(*,*) ntot
      write(*,*) 'Number of points for computation?'
      read(*,*) nlim
      write(*,*) 'End frequency of spectrum (kHz)?'
      read(*,*) endf
      write(*,*) 'Angle between wave vector and B field (deg)?'
      read(*,*) phi
      write(*,*) 'Magnetic field (Gauss)?'
      read(*,*) amagf
      write(*,*) 'Incident radio frequency (MHz)?'
      read(*,*) winc
      write(*,*) 'Electron temperature (K)?'
      read(*,*) te
      write(*,*) 'Electron density (m^-3)?'
      read(*,*) anomn
      write(*,*) 'Parallel drift (kms^-1)?'
      read(*,*) vdpar
      write(*,*) 'Normalised mass of ion species A?'
      read(*,*) aimasa
      write(*,*) 'Normalised mass of ion species B?'
```

```
      read(*,*) aimasb
      write(*,*) 'Temperature of ion species A (K)?'
      read(*,*) temia
      write(*,*) 'Temperature of ion species B (K)?'
      read(*,*) temib
      write(*,*) 'Fraction of ion species A (0-1)?'
      read(*,*) fra

c Convert the input parameters to archaic units for the calculation:
radio
c frequency to Hz, electron density to cm^-3, and electron drift
speed
c to cm/s.

      winc=winc*1.e6
      anomn=anomn*1.e-6
      vdpar=vdpar*1.e5

c Calculated parameters:

c PHI = angle PHI in radians
c AMASIA = mass of ion species A
c AMASIB = mass of ion species B
c VTHIA = thermal speed of species A
c VTHIB = thermal speed of species B
c WMAG = magnitude of wavenumber
c WPP = perpendicular wavenumber
c WPL = parallel wavenumber

      phi=phi*pi/180.
      amasia=aimasa*amasp
      amasib=aimasb*amasp
      vthia=sqrt(2*boltz*temia/amasia)
      vthib=sqrt(2*boltz*temib/amasib)
      wmag=4*pi*winc/vlight
      wpp=wmag*sin(phi)
      wpl=wmag*cos(phi)

c Initialise the frequency loop variables.

      fstep=endf/(ntot-1)
      nmax=2*nlim-1

c Calculate the ion functions.

      ya=1./(wmag*vthia)
      yb=1./(wmag*vthib)
      an=2000*pi*ya
      bn=2000*pi*yb

      do 10,n=1,nmax
       ff=(n-1)*fstep-endf
       wia=ff*an
       wib=ff*bn
       a1(n)=disp1(wia)+1.
       a2(n)=-disp2(wia)
       a3(n)=exp(-wia*wia)*1.772454
       b1(n)=disp1(wib)+1.
       b2(n)=-disp2(wib)
       b3(n)=exp(-wib*wib)*1.772454
10    continue
```

```
c Calculate the temperature ratios.

      tra=te/temia
      trb=te/temib

c Calculate the electron parameters:

c VTHE = thermal speed
c OM = gyrofrequency
c WPE = plasma frequency
c DBLH = Debye length

      vthe=sqrt(2*boltz*te/amase)
      om=elch*amagf/(amase*vlight)
      wpe=sqrt(anomn*elch*elch/amase/pi)
      dblh=sqrt(boltz*te/4/pi/anomn/elch/elch)
      alpha=1./wmag/dblh
      alpha2=alpha*alpha
      ae=wpl*vthe
      xe=wpp*wpp*vthe*vthe/2/om/om

c Calculate the electron functions.

      do 20,n=1,nmax
       we=n*fstep*pi*2000-wpl*vdpar-endf*2000*pi
       e1(n)=dielec1(we,ae,xe)*alpha2
       e2(n)=dielec2(we,ae,xe)*alpha2
       e3(n)=dielec3(we,ae,xe)
20    continue

c Calculate the plasma frequencies:

c WPIA = plasma frequency of species A (Hz)
c WPIB = plasma frequency of species B

      if (fra.le.1.) then
       wpia=sqrt(anomn*fra*elch*elch/amasia/pi)
       wpib=sqrt(anomn*(1-fra)*elch*elch/amasib/pi)
       aw2a=alpha2*fra*tra
       aw2b=alpha2*(1-fra)*trb
       else
        write(*,*)
        write(*,*) 'Improper ion composition fraction (FRA > 1)!'
      write(*,*)
      call exit(1)
      endif

c Calculate the zero frequency power (for normalisation).

      freq0=nlim-1
      her=e1(freq0)
      hei=e2(freq0)
      ame=e3(freq0)
      hir=a1(freq0)*aw2a+b1(freq0)*aw2b
      hii=0.
      ami=a3(freq0)*ya*fra+b3(freq0)*yb*(1-fra)
      snorm=spec(her,hei,hir,hii,ame,ami)

c Open the output file, calculate the spectrum and write the results
to file.
```

```
      open(unit=10,file='iaspec.out')
      do 30,n=1,nmax
       freq=n*fstep-endf
       her=e1(n)
       hei=e2(n)
       ame=e3(n)
       hir=a1(n)*aw2a+b1(n)*aw2b
       hii=a2(n)*aw2a+b2(n)*aw2b
       ami=a3(n)*ya*fra+b3(n)*yb*(1-fra)
       skw=spec(her,hei,hir,hii,ame,ami)/snorm
       write(10,*) freq,hir,hii,ami,skw
30    continue

      stop
      end

c Here ends the main program. There follow a few functions called by
the main
c program above.

c Function to evaluate the zeroth order modified Bessel function of
x*exp(x).
c The method uses a polynomial approximation and the results apply
only for
c positive arguments x (see, e.g., Stegun & Abramowitz).

      function beso(x)

      if (abs(x).le.3.75) then
       z=(x/3.75)**2
       beso=exp(-x)*((((((4.5813e-3*z+3.60768e-2)*z+2.659732e-1)
     @      *z+1.2067492)*z+3.0899424)*z+3.5156229)*z+1.)
       return
       else
        z=abs(3.75/x)
      beso=1./sqrt(3.75/z)*(((((((3.92377e-3*z-1.647633e-2)*z+
     @       2.635537e-2)*z-2.057706e-2)*z+9.16281e-3)*z-1.57565e-3)
     @       *z+2.25319e-3)*z+1.328592e-2)*z+3.989422e-1)
        return
      endif
      end

c Function to evaluate the spectral density function given the
electron and
c ion contributions to the longitudinal dielectric function, and the
c respective multiplying factors.

c XE = real part of the electron contribution
c YE = imaginary part
c XI = real part of ion contribution
c YI = imaginary part of ion contribution
c ZE = electron multiplying factor
c ZI = ion factor
c SE = electron contribution to spectral density function
c SI = ion contribution to spectral density function */

      function spec(xe,ye,xi,yi,ze,zi)

      xr=xe+xi
      er=1+xr
```

```
      ei=ye+yi
      ea=er*er+ei*ei
      be=((1+xi)**2+yi*yi)/ea
      bi=(xe*xe+ye*ye)/ea
      se=2*ze*be
      si=2*zi*bi
      spec=se+si
      return
      end

c Functions to evaluate Y times the Fried & Conte plasma dispersion
function
c of Y. These functions are valid only for real values of the
argument.
c DISP1 is the real part and DISP2 the imaginary.

      function disp1(y)

      nmax=4*abs(y)+4
      if (abs(y).le.4.) then
       if (abs(y).le.1.) nmax=10
       b=y/2.
       do 40,n=1,nmax
        b=b+sinh(n*y)*exp(-n*n/4.)/n
40     continue
       disp1=y*(-2/1.772454)*exp(-y*y)*b
       return
       else
        if (y*y.le.175.) then
       b=0.
       do 50,n=1,nmax
        e=n*y-n*n/4.-y*y
        if (-e.gt.175.) then
         e1=exp(e)
         else
            e1=0.
        endif
        f=-n*y-n*n/4.-y*y
        if (-f.gt.175.) then
           f1=exp(f)
         else
            f1=0.
        endif
          b=b+(e1-f1)/(2*n)
50      CONTINUE
        disp1=-2/1.772454*y*(b+exp(-y*y)*y/2.)
       return
         else
       yy=1/(2*y*y)
       disp1=-(((15*yy+3)*yy+1)*yy+1)
       return
       endif
      endif
     end

      function disp2(y)

     if (abs(y).le.4.) then
      disp2=-y*1.772454*exp(-y*y)
      return
      elseif (y*y.le.175.) then
```

```
        disp2=1.772454*y*exp(-y*y)
      return
      else
       disp2=0.
       return
      endif
      end

C Functions to evaluate the contribution to the longitudinal
dielectric
c function. DIELEC1 evaluates the real part, DIELEC2 the imaginary
part, and
c DIELEC3 the multiplying factor in the spectral density function.

c W = frequency
c A = parallel wave number * thermal speed
c X = argument of Bessel function

c To obtain the actual contribution to the longitudinal dielectric
function,
c appropriate multiplying factors must be used in the calling
program.

      function dielec1(w,a,x)

      ri=beso(x)
      b=w/a
      dielec1=1+ri*disp1(b)
      return
      end

      function dielec2(w,a,x)

      ri=beso(x)
      b=w/a
      dielec2=-ri*disp2(b)
      return
      end

      function dielec3(w,a,x)

      ri=beso(x)
      b=w/a
      dielec3=1.772454*ri*exp(-b*b)/a
      return
      end
```

Appendix B

Sample from the EXCEL spreadsheet used to identify which satellites need to be checked

Radius of Earth =	6379000				Mass of Earth =	5.975E+24		G =	6.67E-11		MG/4pi =	1.00995E+13	
Satellite No.	Inclination		Epoch Date	Right Ascension of Ascending Node	Eccentricity	Argument of Perigee	Mean Anomaly at Epoch	Mean Motion	a^3	a	Perigee	Apogee	Altitude
64026C	90.7766	46235	99329.519	148.1456	0.0046	240.9332	118.729	14.639	3.52E+20	7059407.704	647.769	713.047	712.092
65072A	98.4749	246523	99328.489	121.6841	0.0247	333.8382	25.051	14.231	3.72E+20	7193681.075	637.340	992.022	775.158
66008B	97.8765	84889	99328.730	205.6529	0.0085	342.946	16.889	14.516	3.58E+20	7099064.907	659.802	780.328	693.304
63014AD	84.3504	2751319	99331.685	239.2472	0.2751	139.6201	244.522	8.910	9.5E+20	9829635.077	746.189	6155.081	5126.016
66111A	99.1183	2320099	99335.290	58.3863	0.2320	327.0156	20.495	10.300	7.11E+20	8923735.683	474.341	4615.131	4579.027
70070A	98.8802	68651	99335.229	222.0802	0.0069	56.1946	304.575	14.308	3.68E+20	7167700.828	739.494	837.908	754.019
70070B	98.8504	71229	99333.198	238.9381	0.0071	116.2041	244.649	14.296	3.69E+20	7171819.884	741.736	843.904	741.939

			time=	99336.02	36496	0.017072				Longitude of Aries=	282.995		
											15	24	104
Mean Anomaly	Mean Anomaly (radians)	True Anomaly	b	d	Latitude	cos(theta)	sin(theta)	theta	Right Ascension	Longitude	test position relative to beam	test eccentricity	test epoch date
165.983	2.897	166.110	7059332.25	47.043	47.0378	0.9999	-0.0146	-0.8340	147.3116	70.3071			1
74.380	1.298	77.123	7191494.81	50.961	50.1956	0.9839	-0.1788	-10.3005	111.3836	34.3790			1
297.232	5.188	296.363	7098809.12	279.309	-77.8281	0.7672	0.6414	39.8954	245.5483	168.5437			1
100.655	1.757	128.279	9450274.95	267.899	-83.9736	-0.3492	-0.9371	249.5626	488.8098	51.8053		1	
196.819	3.435	190.716	8680237.50	157.731	21.9725	-0.9979	-0.0648	183.7129	242.0992	165.0947		1	
44.630	0.779	45.186	7167531.92	101.381	75.6008	-0.7935	-0.6086	217.4851	439.5653	2.5607	1		
354.955	6.195	354.883	7171637.95	111.087	67.2095	-0.9288	-0.3706	201.7520	440.6901	3.6856	1		

Appendix C

Sample output from the EXCEL spreadsheet used to identify the position of a satellite relative to the radar beam

Dec 01 99													
	Satellite											Detected	
Time 1	No.	Az S1	El S1	z1	Time 2	Az S2	El S2	z2	RN	Range	Power	by radar	Comments
10:30:35	94029GY	184.80	83.51	1.971418	10:30:36	180.86	83.00	1.400125	0.920566	629	1.7956	yes	
10:31:12	94029GH	182.95	82.13	0.597456	10:31:13	179.88	81.63	0.166053	0.144429	651	4.7880	yes	
10:31:20	79012B	179.78	85.13	3.532615	10:31:21	180.86	77.73	3.870079	0.068485	498	2.8954	yes	
10:50:01	68026C	180.54	87.44	5.840118	10:50:02	181.03	87.46	5.860000	4.328649	8846		no	too high
10:51:43	94029VR	181.18	67.72	13.880065	10:51:44	180.21	67.22	14.381240	8.336242	669		no	too wide
11:36:34	99051A	178.59	82.37	0.839966	11:36:35	181.54	81.90	0.309842	0.250519	706	733.4973	yes	
11:41:21	95046A	181.95	85.74	4.141184	11:41:22	177.26	85.24	3.663225	2.481757	686	10.2678	yes	
11:46:25	81053KU	181.40	83.24	1.640839	11:46:26	179.03	82.82	1.248702	0.906526	829		no	
11:47:10	86019NH	179.76	86.37	4.771492	11:47:11	185.70	85.93	4.356378	3.252242	739		no	too wide
11:47:21	78026AM	179.60	83.63	2.037811	11:47:22	183.49	84.02	2.439421	1.580225	755		no	
12:06:31	99057B	180.20	82.10	0.512689	12:06:32	182.83	81.68	0.277821	0.253143	770	0.4615	yes	
12:07:32	64031C	180.74	85.14	3.540118	12:07:33	185.26	84.81	3.247141	2.782831	832	0.2303	yes	
12:08:21	93050C	180.56	78.41	3.190891	12:08:22	182.32	78.76	2.848725	2.169370	870		no	too high
12:16:27	90010B	183.27	82.96	1.393505	12:16:26	180.06	83.51	1.913816	1.013881	646	2.9063	yes	
12:18:47	91050A	176.69	86.26	4.678966	12:18:48	182.23	85.88	4.281856	3.007400	805	1.5830	yes	
12:25:21	74089FE	176.32	86.06	4.484590	12:25:22	184.01	85.85	4.261261	4.027641	749		no	too wide
Dec 02 99													
	Satellite											Detected	
Time 1	No.	Az S1	El S1	z1	Time 2	Az S2	El S2	z2	RN	Range	Power	by radar	Comments
0:03:46	80069A	182.44	85.52	3.923019	0:03:47	174.05	86.09	4.543255	2.823740	518	1.7107	yes	
0:24:38	91039B	181.64	82.49	0.894383	0:24:39	178.76	82.99	1.421813	0.582369	683	7.8705	yes	
0:32:01	79017CA	179.31	75.19	6.418330	0:32:02	181.71	74.39	7.211378	4.254321	427		no	too wide
0:52:02	98042C	182.59	83.27	1.682909	0:52:03	176.56	82.89	1.421409	1.418818	526	10.2020	yes	
0:52:49	94029FV	214.77	89.23	7.771628	0:52:50	174.78	89.85	8.250899	5.513441	653		no	too wide
2:25:51	88093A	169.36	81.67	1.691957	2:25:52	167.53	81.08	2.088491	1.476150	650	6.3440	yes	
2:36:40	99011A	161.78	80.95	2.972131	2:36:41	163.52	81.62	2.540918	2.188170	596	0.5595	yes	
4:10:11	94029ER	175.71	82.41	1.093480	4:10:12	172.64	81.79	1.221283	1.078968	573	0.3574	yes	
4:34:05	83063B	183.09	81.10	0.590518	4:34:06	181.08	81.52	0.080857	0.038650	815	262.8300	yes	
4:34:09	72069A	181.90	81.63	0.134625	4:34:10	181.83	81.11	0.505621	0.130838	807	34.8665	yes	
4:38:29	90043C	148.47	81.43	4.739772	4:38:30	146.42	81.94	4.887521	4.651101	724		no	too wide
4:45:52	88020B	182.42	80.01	1.605990	4:45:53	180.29	80.54	1.065694	0.696456	662	7.2132	yes	
5:11:40	82092A	189.32	80.49	1.702962	5:11:41	186.51	79.98	1.842714	1.702951	609	0.2776	yes	

Appendix D

Final version of 'test_asymm' subroutine used to help identify anomalous spectra

```
function test_asymm(spe,freq,range)
%---------------------------------{

    global peak_width crit_ratio DMPT out_fid gflag
    global sat_ratio ELEV
%   work out the time from the last parameter block of the
%   integration period
    yyyy = round(DMPT(1));
    mm = round(DMPT(2));
    dd = round(DMPT(3));
    hh = round(DMPT(4));
    mi = round(DMPT(5));
    ss = round(DMPT(6));

%   find the frequency separation

    fre1 = freq(2)-freq(1);

%   fprintf('Testing asymmetry')
%   to work out exclusion zone, divide peak_width by width
%   of one frequency bin (fre1 = 0.763 kHz in gup3) and then divide
%   by two
    nexclude = peak_width/fre1;
    nexclude = round(nexclude/2);
    if crit_ratio > 1
      rat1 = crit_ratio;
      rat2 = 1.0/crit_ratio;
    elseif crit_ratio <= 1
      rat1 = 1.0/crit_ratio;
      rat2 = crit_ratio;
    end
    [nfreq,nrange]=size(spe);
    satprob = 0;

    for i = 1:nrange
     i1(i) = i;
     power(i) = 0.0;
     for j = 1:nfreq
%    fprintf(out_fid,'%9.2f %9.2f %e\n',range(i),freq(j),spe(j,i))
      power(i) = power(i) + spe(j,i);
     end
%    fprintf(out_fid,'%e\n',power(i))
    end
    sflag1 = 0;
    sflag2 = 0;
    srange=0.0;
    erange=0.0;
%    this section added by Joyce Porteous 07/01/02 to test for
satellites
%    using the information based on increase and decrease in power
    maxjump=-1.0;
    for i = 7:nrange-3
     diff(i) = power(i+3)-power(i);
     if power(i+3) < power(i)
       denom = power(i+3);
     elseif power(i) < power(i+3)
       denom = power(i);
     end
     ratio(i) = diff(i)/denom;
```

```
      if maxjump < ratio(i)
        maxjump = ratio(i);
      end
       if ratio(i) > sat_ratio
        srange = range(i);
        sflag1 = 1;
      end
     if sflag1 == 1
       if ratio(i)<-sat_ratio
         erange = range(i);
         sflag2 = 1;
       end
      end
     end
     if sflag1 == 1
%     figure
%     plot (i1,power)
      if sflag2 == 1
       fprintf('Probable evidence of satellite!\n')
       satprob=2;
      end
      if sflag2 == 0
       fprintf('Possible evidence of satellite!\n')
       satprob=1;
      end
     end
     if sflag2 == 1
%     figure
%     plot (i1,power)
      if sflag1 == 0
       fprintf('Possible evidence of satellite!\n')
       satprob=1;
      end
     end
     spread = 0.0;
     if srange > 0.0
      if erange > 0.0
        spread = abs(erange-srange);
      end
     end
%    sflag1
%    sflag2
%    srange
%    erange
%    spread

     for i = 1:nrange
       [pmax,ppos] = max(spe(:,i));
%      spe(1:ppos-nexclude,i)
       [p2max,p2pos] = max(spe(1:ppos-nexclude,i));
       [p3max,p3pos] = max(spe(ppos+nexclude:nfreq,i));
%      The next line changed by Ian McCrea 23/04/01 to stop possible
%      overflow in array, note that (ppos+nexclude) returns 1 for
p3pos
%      above, so need to subtract 1 from p3pos in the sum below.
%      p3pos = p3pos+ppos+nexclude;
       p3pos = p3pos+ppos+nexclude-1;
%      ppos
%      p2pos
%      p3pos
       down = 0;
```

```
      up = 0;
      unshift = 0;
      if freq(ppos) < 0
        down = 1;
      elseif freq(ppos) > 0
        up = 1;
      elseif freq(ppos) == 0
        unshift = 1;
      end
      if p2max <= p3max
        smax = p3max;
        lpos = p3pos;
      else
        smax = p2max;
        lpos = p2pos;
      end
      maxrat = smax/pmax;
%     the next line added by Joyce Porteous 28/05/02 to eliminate
%     anomalous spectra with Doppler shifts close to zero
      if abs(freq(ppos)) >=4 5
       if maxrat <= rat2
        gflag = 1;
        fprintf ('Range: ','%6.2f',range(i))
        if up == 1
          fprintf('Asymmetric spectrum - upshifted\n')
        elseif down == 1
          fprintf('Asymmetric spectrum - downshifted\n')
        elseif unshift == 1
          fprintf('Asymmetric spectrum - unshifted\n')
        end
        fprintf (out_fid, ...
         '%i %i %i %i %i %i %9.2f %9.2f %9.2f %9.2f %9.2f %i
%9.4f\n', ...
         yyyy,mm,dd,hh,mi,ss,range(i),maxrat,freq(ppos),freq(lpos),
...
         ELEV,satprob,maxjump);
       end
       if maxrat >= rat1
        gflag = 1;
        if up == 1
          fprintf('Asymmetric spectrum - upshifted\n')
        elseif down == 1
          fprintf('Asymmetric spectrum - downshifted\n')
        elseif unshift == 1
          fprintf('Asymmetric spectrum - unshifted\n')
        end
        fprintf (out_fid, ...
         '%i %i %i %i %i %i %9.2f %9.2f %9.2f %9.2f %9.2f %i
%9.4f\n', ...
         yyyy,mm,dd,hh,mi,ss,range(i),maxrat,freq(ppos),freq(lpos),
...
         ELEV,satprob,maxjump);
       end
      end
    end
%}  test_asymm
```

Appendix E

EXCEL spreadsheet used for modelling the oxygen emission ratios using analysed data

To Calculate intensity Ratio

Ne	**1.00E+05**	A630/A558	5.82E-03			**aN2**	**3.10E+06**
Ti	**1.60E+03**					**aO**	**8.70E+07**
Te	**2.00E+03**	**Numerl**	**1.2612E-05**			**a02**	**9.20E+04**
Tn	**1.30E+03**	**Numer2**	**2.42E-09**			**aN**	**3.80E+06**
		Denom	**0.01229891**			**aNO**	**0**
						aN2+	**3.10E+03**
Ttherm	**2.00E+03**	**nl**	**1.03E-03**			**aO+**	**8.70E+04**
Thuge	**5.00E+03**	**n2**	**1.97E-07**			**a02+**	**9.20E+01**
Tave	**2.50E+03**	nl/n2	5.20E+03			**aN+**	**3.80E+03**
						aNO+	**0**
Nemin	**1.00E+05**	IntRatio	3.03E+01			**aN***	**0**
Nemax	**1.20E+05**						
r	**8.33E-01**					**pn**	**0**
						Pt	**0**
		COltherm	**8.36E-15**	**C01**	**2.49369E-12**		
		C02therm	**1.606E-21**	**C02**	**1.32645E-15**		
A630	**6.54E-03**	**C12therm**	**1.11E-20**	**C12**	**8.38166E-15**		
A636	**2.11E-03**	**ClOtherm**	**1.36E-09**	**CIO**	**1.5675E-09**		
A558	**1.124**	**C20therm**	**4.850E-10**	**C20**	**5.97868E-10**		
		C21therm	**1.867E-09**	**C21**	**2.2355E-09**		
A10	**8.65E-03**	**COlhuge**	**1.492E-11**			**PI**	**9.50E-06**
A20	**0.079**	**C02huge**	**7.959E-15**			**P2**	**2.55E-07**
A21	**1.215**	**C12huge**	**5.029E-14**			**Qi**	**1.215223301**
		ClOhuge	**2.583E-09**			**Q2**	**9.70811E-10**
		C20huge	**1.162E-09**			**LI**	**9.50E-03**
		C21huge	**4.080E-09**			**L2**	**1.294285266**
		k3	**9.23E-08**	**P3**	**8.50E-06**		
		k6	**5.00E-12**	**P6**	**0.00E+00**		
Pi	**9.26E-06**	**k7**	**2.00E-10**	**P7**	**7.60E-07**		
		k3'	**1.83E-09**	**P3'**	**1.68E-07**		
Pii	**2.55E-07**	**k2'**	**2.80E-11**	**P2'**	**8.68E-08**		
		kN2	**2.17E-11**	**rN2**	**6.74E-05**		
		k02	**3.05E-11**	**r02**	**2.81E-06**		
Li	**6.95E-04**	**kO**	**7.19E-12**	**rO**	**6.25E-04**		
		k02'	**2.06E-12**	**r02'**	**1.89E-07**		
Lii	**1.93E-06**	**kO'**	**2.00E-14**	**rO'**	**1.74E-06**		

1/kb	157890					
qconst	8.62933E-06					
enat1	0		delt2	1.142E+01		
enat2	0.1446		delt3	2.424E+01		
enat3	0.307					
iw1	9					
iw2	5		hdelt2	4.566E+00		
iw3	1		hdelt3	9.694E+00		
up	2.000E+03		q	1	2	3
up01	3.536E-02		1	0	8.356E-15	1.606E-21
up02	2.513E-03		2	1.364E-09	0	1.113E-20
up12	9.673E-03		3	4.850E-10	1.867E-09	0
hup	5.000E+03		hq	1	2	3
hup01	1.058E-01		1	0	1.492E-11	7.959E-15
hup02	9.524E-03		2	2.583E-09	0	5.029E-14
hup12	3.344E-02		3	1.162E-09	4.080E-09	0

	R-Matrix								
	T	U12	U13	U23					
	0	0	0	0		2.00E+03			
2.00	1.00E+02	9.44E-03	6.29E-04	1.49E-03		14			
2.10	1.26E+02	1.00E-02	6.74E-04	1.60E-03		1995	0.03529	0.002507	0.009637
2.20	1.59E+02	1.07E-02	7.28E-04	1.73E-03		2512	0.04203	0.003167	0.01339
2.30	2.00E+02	1.16E-02	7.93E-04	1.90E-03		2000	0.0353552	0.0025134	0.0096733
2.40	2.51E+02	1.27E-02	8.72E-04	2.10E-03					
2.50	3.16E+02	1.40E-02	9.65E-04	2.34E-03					
2.60	3.98E+02	1.55E-02	1.07E-03	2.63E-03		5.00E+03			
2.70	5.01E+02	1.73E-02	1.20E-03	2.99E-03		17			
2.80	6.31E+02	1.94E-02	1.35E-03	3.42E-03		3981	0.07414	0.006412	0.02538
2.90	7.94E+02	2.18E-02	1.51E-03	3.96E-03		5012	0.1062	0.009561	0.03353
3.00	1.00E+03	2.46E-02	1.70E-03	4.65E-03		5000	0.1058268	0.0095243	0.0334351
3.10	1.26E+03	2.76E-02	1.90E-03	5.63E-03					
3.20	1.59E+03	3.10E-02	2.14E-03	7.17E-03					
3.30	2.00E+03	3.53E-02	2.51E-03	9.64E-03					
3.40	2.51E+03	4.20E-02	3.17E-03	1.34E-02					
3.50	3.16E+03	5.39E-02	4.37E-03	1.86E-02					
3.60	3.98E+03	7.41E-02	6.41E-03	2.54E-02					
3.70	5.01E+03	1.06E-01	9.56E-03	3.35E-02					
3.80	6.31E+03	1.53E-01	1.41E-02	4.30E-02					
3.90	7.94E+03	2.15E-01	2.01E-02	5.36E-02					
4.00	1.00E+04	2.93E-01	2.77E-02	6.54E-02					
4.10	1.26E+04	3.85E-01	3.68E-02	7.82E-02					
4.20	1.59E+04	4.86E-01	4.73E-02	9.19E-02					
4.30	2.00E+04	5.92E-01	5.90E-02	1.07E-01					
4.40	2.51E+04	7.00E-01	7.15E-02	1.22E-01					
4.50	3.16E+04	8.07E-01	8.45E-02	1.40E-01					
4.60	3.98E+04	9.11E-01	9.76E-02	1.59E-01					
4.70	5.01E+04	1.01E+00	1.11E-01	1.81E-01					
4.80	6.31E+04	1.11E+00	1.24E-01	2.04E-01					
4.90	7.94E+04	1.20E+00	1.36E-01	2.30E-01					
5.00	1.00E+05	1.28E+00	1.48E-01	2.58E-01					
5.10	1.26E+05	1.36E+00	1.58E-01	2.86E-01					
5.20	1.59E+05	1.42E+00	1.68E-01	3.15E-01					
5.30	2.00E+05	1.47E+00	1.75E-01	3.45E-01					
5.40	2.51E+05	1.50E+00	1.80E-01	3.74E-01					
5.50	3.16E+05	1.51E+00	1.82E-01	4.03E-01					
5.60	3.98E+05	1.49E+00	1.80E-01	4.31E-01					
5.70	5.01E+05	1.44E+00	1.74E-01	4.58E-01					
5.80	6.31E+05	1.37E+00	1.65E-01	4.83E-01					
5.90	7.94E+05	1.28E+00	1.53E-01	5.06E-01					
6.00	1.00E+06	1.17E+00	1.39E-01	5.25E-01					

Published Paper

Automated detection of satellite contamination in incoherent scatter radar spectra

J.Porteous, A.M. Samson, K.A. Berrington and I.W. McCrea

Annales Geophysicae (2003) 21: 1177–1182 © European Geosciences Union 2003

Annales Geophysicae

Automated detection of satellite contamination in incoherent scatter radar spectra

J. Porteous[1], A. M. Samson[1], K. A. Berrington[1], and I. W. McCrea[2]

[1]School of Science and Mathematics, Sheffield Hallam University, Sheffield, S1 1WB, UK
[2]Space Science Department, Rutherford Appleton Laboratory, Chilton, Oxon, OX11 0QX, UK

Received: 4 July 2002 – Revised: 4 December 2002 – Accepted: 17 January 2003

Abstract. Anomalous ion line spectra have been identified in many experiments. Such spectra are defined as deviations from the standard symmetric "double-humped" spectra derived from incoherent scatter radar echoes from the upper atmosphere. Some anomalous spectra – where there are sharp enhancements of power over restricted height ranges – have been attributed to satellite contamination in the beam path. Here we outline a method for detecting such contamination, and review in detail a few cases where the method enables the identification of anomalous spectra as satellite echoes, subsequently ascribed to specific orbital objects. The methods used here to identify such satellites provide a useful way of distinguishing anomalous spectra due to satellites from those of geophysical origin. Analysis of EISCAT Svalbard Radar data reveals that an average of 8 satellites per hour are found to cross the beam. Based on a relatively small sample of the data set, it appears that at least half of the occurrences of anomalous spectra are caused by satellite contamination rather than being of geophysical origin.

Key words. Ionosphere (auroral ionosphere, instruments and techniques) – Radio Science (signal processing)

1 Introduction

Incoherent scatter radars have been used to study the Earth's ionosphere since their introduction in 1959. The European Incoherent Scatter radar (EISCAT) in Northern Scandinavia is positioned in the auroral zone and is reviewed in Risbeth and Williams (1985). By contrast the EISCAT Svalbard radar (ESR) is positioned further north in the polar cap region (74° magnetic latitude). It first started its operations in 1996 and a detailed introduction to the system can be found in Wannberg et al. (1997). The information obtained from these radars is contained both in the spectral shape of the scattered signal and in the power returned. The majority of the ion line spectra are of the standard symmetric "double-humped" type as expected. There has been much interest in those spectra with enhanced ion-acoustic shoulders since the time when they were first identified in incoherent scatter spectra (Foster et al., 1988) using data from the Millstone Hill radar in Westford, Massachusetts. Other authors (Rietveld et al., 1991; Collis et al., 1991; Forme, 1995) have reported occurrences of anomalous spectra in the data from the Tromsø radar in Norway.

Many theories have been proposed to account for the occurrences of such spectra. The earliest of these suggests that they may be due to current-driven instabilities, but in this situation the field-aligned current densities would need to be unusually high (Collis et al., 1991; Rietveld et al., 1991). A second possibility is that they may be due to the parametric decay of Langmuir waves (Forme, 1995), whilst a third suggestion is that they are caused by ion-ion two-stream instabilities (Wahlund et al., 1992).

Many examples of naturally enhanced ion acoustic spectra have been reported in the ESR data. Recently, Buchert et al. (1999) suggest that the ion-acoustic fluctuation level seems to depend quite strongly on the wave number, k. In their review paper, Sedgemore-Schulthess et al. (1999) discuss examples of enhanced spectra in the context of small-scale aurora, transient field-aligned currents and time varying magnetic reconnection. For a detailed review of naturally-enhanced ion-acoustic spectra, see Sedgemore-Schulthess and St-Maurice (2001).

Given the large size of incoherent scatter data sets, the only acceptable method of identifying such spectra is to use an automated program to search the data. However, as the paper by Rietveld et al. (1996) indicates, there are many other causes of spectral anomalies, the most common of which is satellite contamination. The identification of anomalous echoes of geophysical interest would be greatly facilitated if a reliable algorithm could be found to identify and reject the satellite contamination. As a result, we have attempted to find a way of automatically checking the data for anomalous spectra and isolating those cases which are clearly caused by satellites.

Correspondence to: J. Porteous
(J.Porteous@shu.ac.uk)

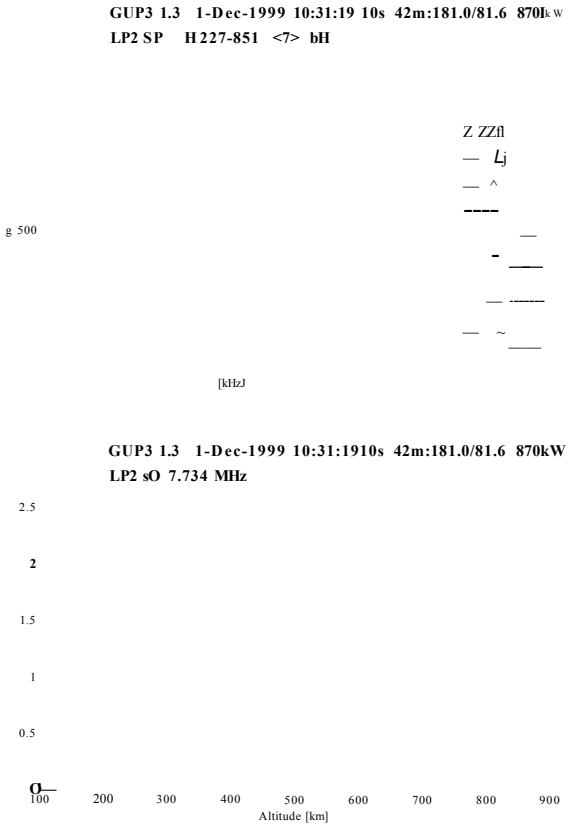

Fig. 1. Results showing **(a)** spectra, and **(b)** power profile for LP2 data at 10:31:19 UT, 1 December 1999, using EISCAT rtg3 program when a probable satellite was seen in the beam.

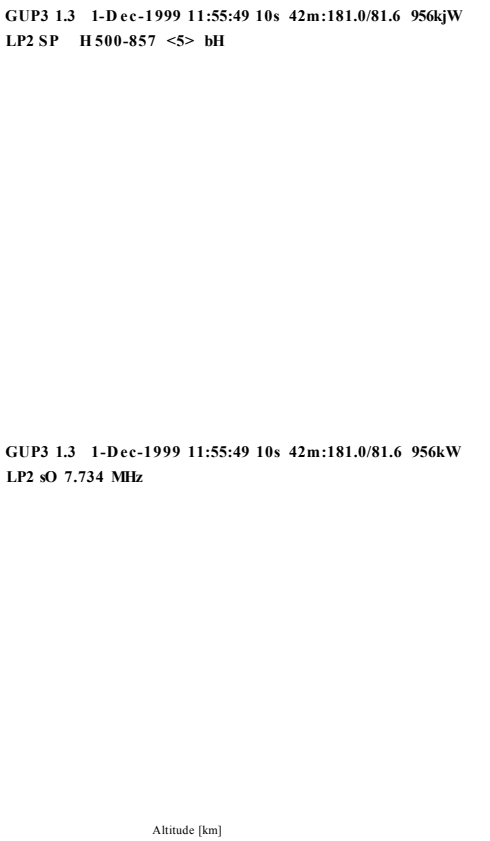

Fig. 2. Results showing **(a)** spectra, and **(b)** power profile for LP2 data at 11:55:49 UT, 1 December 1999, using EISCAT rtg3 program when enhanced spectra probably due to geophysical causes were seen in the beam.

2 Identifying enhanced spectra

The data used in this study come from the EISCAT Svalbard Radar (ESR), and are measured using the GUP3 experiment. This experiment makes use of both plain, long pulses and alternating codes, which are binary codes based on phase-coded long pulses. The use of two different modulations with overlapping range coverage is important, as it allows the presence of anomalies to be confirmed by comparing the data from the two pulse schemes. The experiment makes use of two long pulse channels, LP1 and LP2, and two channels for alternating code data, AC 1 and AC2. In this study, we discuss results from the comparison of the data from LP2 and AC2, although LP 1 and AC 1 were also checked to ensure that the results are consistent. The range covered by the LP2 data is 229.5-859.5 km, whilst that covered by the AC2 data is 228-732 km. Hence, the LP and AC data overlap within a region whose range extent is about 500 km. Within this region, full measurements of the shape of the backscattered spectrum can be obtained from both srheimes. along with "power profiles", representing the variation in the backscattered power as a function of range.

A simple method is employed to search for anomalous ion-line spectra, based on the asymmetry between the upshifted and downshifted ion-acoustic peaks. First, we obtain the frequency at which the spectrum attains its maximum value. We call this the primary peak. Finding a secondary peak, if one exists, is more difficult. Instead, we restrict attention to the data more than 2.5 kHz from the primary peak and find the frequency at which the maximum occurs in this remaining data set. On most occasions, it can be verified that these two frequencies represent the peaks of the ion-acoustic lines. However, when the secondary peak is much lower than the primary one, the program will not identify the secondary peak. Instead, it identifies a point on a shoulder of the primary peak. When the ratio of the heights of these two points is less than some threshold value, the details are stored in a file for later examination. After making several observations, the arbitrary number 0.8 is chosen as the threshold value. This is seen to ensure that those situations of interest to us are identified along with a small number of spurious cases which subsequently can be eliminated by a manual check.

In this paper, we present a typical example of the GUP3 data, from 1 December 1999. The data set consists of

1011 ten-second dumps recorded between 10:11:30 UT and 13:00:00 UT. The automated routine described above is used to examine the data from the LP2 long-pulse channel. The times at which anomalous spectra are identified by the program are recorded for subsequent manual examination. In some cases, it transpires that the spectra identified as being anomalous contain essentially no backscattered signal and any such noisy spectra are eliminated. This leaves a number of spectra where the program suggests the presence of a satellite. Typical enhanced spectra from such a case are shown in Fig. 1a. In particular, the power profiles for these times are checked. When the returned signal is thought to be the result of a reflection from a satellite or item of space debris, the power profile measured on the LP2 channel shows a sudden sharp increase, followed by a similarly sudden sharp decrease approximately 100 km further along the beam, as shown in Fig. 1b. The spacing between these steps in the power is related to the range ambiguity of the sounding pulse, so a satellite large enough to cause a significant change in the returned power is detected in several range gates. This explains why the power increase is visible over a 100 km range. Sometimes the object detected is at a sufficiently high altitude for only the increase in power, but not the subsequent decrease, to be within the range coverage of the recorded data. These situations are classified as possible satellites.

In contrast to this example, there are times when there are enhanced spectra in the data but the power profile shows no significant change, as shown in Fig. 2. The spectra obtained at these times can, therefore, be the result of a geophysical phenomenon. In a situation where the enhancements in one ion line switch to the other line (Sedgemore-Schulthess et al., 1999), the enhancements are thought to be short-lived as are those for satellites. However, any increase in power which occurs is likely to be gradual rather than sudden, so it takes several range gates for the full increase to show in such geophysical situations. The example shown in Fig. 2 needs further consideration if it is to be identified definitely, either as a geophysical phenomenon or as one or more satellites passing through the beam.

A detailed study of the variations between adjacent points in the power profile reveals that a few very large power variations are seen, which are clearly attributable to satellites. Excluding these, the remaining variations show a continuous distribution, rather than being sharply divided between large and small changes. The distribution is shown in Fig. 3. In order to accommodate the full range of power ratio variations on the same graph, the natural logarithm of the power ratio variation has been plotted.

Considering the histogram in Fig. 3, the cases at the left-hand extreme of the x-axis are highly likely to be due to geophysical conditions, whilst those at the right-hand extreme are highly likely to be due to satellites. This leaves a large number of intermediate points, many of which could also be due to satellites, either of varying cross section, or passing through the side lobes rather than the main beam.

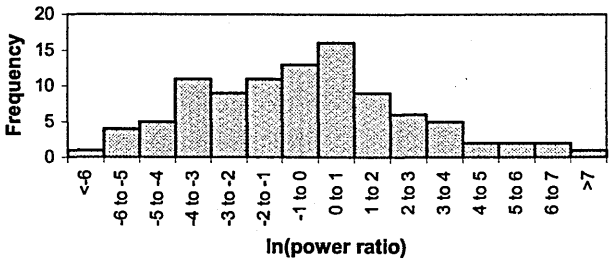

Fig. 3. Histogram showing frequency of occurrence of ln of power ratios obtained when enhanced spectra occurred in the 1 and 2 December 1999 ESR, GUP3 data.

3 Long pulse and alternating code comparisons

To progress further, a comparison is made between the long pulse (LP2) results and those from the alternating code (AC2) data. The range extent of the LP2 long pulse data is 229.5–859.5 km, whilst for the AC2 data it is only 228–732 km. As a consequence, only a subset of the anomalous spectra identified in the LP2 data can be checked using the AC2 data.

By examining the power profile from the AC2 data at the relevant times, similar characteristics can be seen, as shown in Fig. 4. When the enhanced spectra are probably due to a satellite passing through the beam, the AC2 power profile shows a steep pointed peak; otherwise, there is no significant change. The smaller extent of the peak in the power profile response arises because the range resolution is better for the alternating code data than it is for the long pulse data. At these times the peak of the AC power is confined to a very narrow range and is within the region in which the step occurs in the LP data. Thus, good agreement is shown between the two pulse schemes. In addition, the use of the AC data helps to clarify a number of cases where the LP data alone does not provide an unambiguous identification of a satellite.

In order to classify the data, we use a threshold ratio for the LP power increases between adjacent range gates above which the enhancement is probably caused by a satellite. Below this ratio geophysical causes are more likely, but there is a possibility that the anomally is caused by very small items of space debris or by a satellite being detected in the far side lobes of the radar beam. For the data we are considering here we suggest that an appropriate threshold to use is 0.2. This represents a 20% increase in the returned power. Examples which are close to the threshold are checked manually.

We now consider ways of calibrating such identifications, to verify that satellites or their debris have indeed passed through the beam.

4 Checking for satellites

The monitoring of space debris, and the determination of its orbital parameters is an important activity for the space industry. Many such objects are routinely monitored and their positions can subsequently be reconstructed. An element file

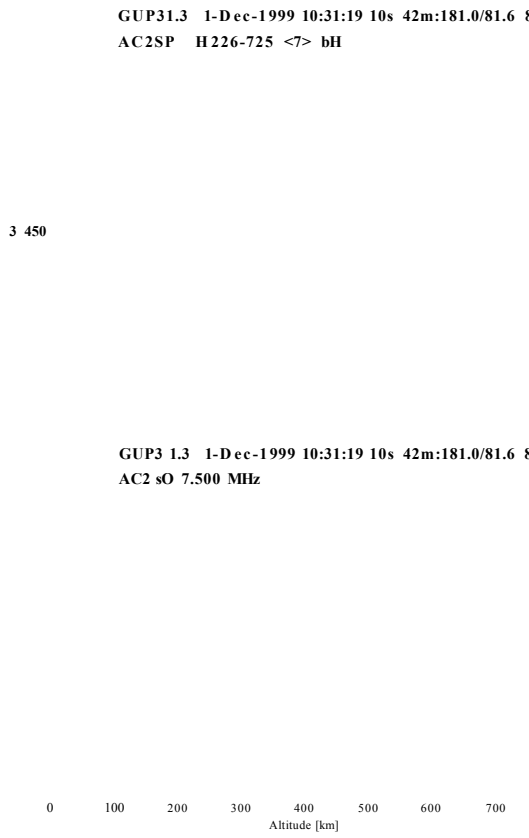

Fig. 4. Results showing **(a)** spectra, and **(b)** power profile for AC2 data at 10:31:19 UT, 1 December 1999, using EISCAT rtg3 program when a probable satellite was seen in the beam.

for satellites and other space debris with NORAD catalogue numbers, (University of Arizona, 2002), updated on 2 December 1999, is used to check for the occurrence of satellites in the ESR radar beam at various times on 1 December 1999.

At 10:31:13 UT an object with catalogue number 24134-94029 GH is found to have had an azimuth of 179.88°, an elevation of 81.63° and a range of 652 km relative to the EISCAT Svalbard Radar, as shown in Fig. 5.

The radar data indicates that at 10:31:19UT (i.e. the 10-s dump starting at 10:31:10UT) there was a probable satellite visible in the beam. The range of the observed anomalous echo is in good agreement with the predicted position of the object.

Using spherical trigonometry, the distance of the object from the centre of the radar beam can be calculated. The radar beam had an elevation of 81.6° and an azimuth of 181.0°. Hence, the identified object was 1.9 km from the centre of the beam. This is well within the limits of the expected lateral extent (~6.5 km) of the main beam at a range of ~650 km.

This example, together with five other times at which the prediction software successfully confirms the presence of a satellite or item of space debris within the range of the beam, are shown in Table 1. The examples identified at 10:31:13 UT and 12:04:10 UT are likely to have been detected within the main beam, whilst the rest are more likely to have been detected in the side lobes. At each of these times the power profiles for both the LP2 and the AC2 returned signal show the typical characteristics described earlier, suggesting that the sounding pulses were being reflected from a hard target. The object detected at 11:36:35UT is likely to have been quite large, hence, the high value obtained for the power ratio.

At 12:07:32 UT a satellite is noticed to be 3.210° from the centre of the radar beam and at 834 km along its range. This is too great a range to enable it to be visible in the AC2 data. However, the LP2 data does show enhanced spectra around this range, as well as the expected increase in power. The increase in power, though significant, is not as great as in the earlier examples. This is possibly a result of the larger distance from the beam centre, suggesting that the satellite passed through the side lobes rather than the main beam. A further satellite at 12:08:21 UT is identified to be 2.849° from the centre of the beam, but at a range of 871 km. This is not detected in either the AC2 nor the LP2 data. Additionally, at 11:55:30 UT a satellite 6.319° from the centre of the radar beam and at a range of 815 km is not detected in the LP2 data.

5 Conclusions

Over 1000 ten-second dumps of raw data from the EISCAT Svalbard Radar have been studied, in order to find a method for identifying likely causes of enhanced spectra. It is suspected that many of the cases found are due to satellites or space debris passing through the main beam or the side lobes. An automated routine has been developed and used to identify those times at which enhanced spectra occur.

It is shown that examining the variation of power with range gives a good indication of whether the spectra are caused by satellites or are possibly of a geophysical nature. In the ESR GUP3 experiment, which contains both long pulse and alternating code data, enhancements in the power profiles of both modulations are noted when satellites appear. A threshold increase of 20% in the returned power is used to help divide the cases into two classes. Situations in which the returned power shows an increase of 20% or more are classified as being due to satellites or space debris. Those which show a smaller increase in power need further investigation to see if they have a geophysical cause. On this basis, it is possible to use an automated program to distinguish between such cases. A small number of noisy spectra are identified by the program and have to be eliminated.

In the period 10:11:30 UT to 13:00:00 UT on 1 December 1999 the numbers of satellites and possibly naturally enhanced spectra occurring in the region covered by the ESR radar beam are as given in Table 2. It can be seen that there are, on average, about eight satellites per hour passing through the radar beam.

Fig. 5. Path of space debris, NORAD number 24134-94029GH, showing its position relative to the radar at ESR at 10:31:BUT on 1 December 1999.

Table 1. A sample of times at which a satellite or item of space debris appeared within the ESR beam on 1 December 1999

Time (UT) on 1 Dec 1999	NORAD Cat. No.	Angle from centre of radar beam (°)	Range (km)	Power Ratio
10:30:36	24149-94029GY	1.400	629	1.796
10:31:13	24134-94029GH	0.166	652	4.788
11:36:35	25919-99051A	0.310	706	733.497
12:04:10	12760-81053DD	0.195	762	4.467
12:06:32	25941-99057B	0.278	771	0.462
12:16:27	20466-90010B	1.394	641	2.906

Table 2. The number of satellites and possibly naturally enhanced spectra found in the region covered by the ESR beam for 10:11:30 UT to 13:00:00 UT on 1 December 1999

Range(km)	Number of satellites	Number of possibly naturally enhanced spectra
<600	2	1
600-750	7	5
>750	15	10

Satellites which are at too great a distance, such as that predicted at 12:08:21 UT with a range of 871 km, are not detected by the radar. Similarly, those at too large an angle from the beam centre, such as that predicted at 11:55:30 UT at an angular distance of 6.319°, are not detected. This gives some insight into the area within which the beam at Svalbard could detect satellite contamination. Further work needs to be carried out to provide greater refinement.

The routine has been tested using a further 6 h of data on 2 December 1999 and almost 16 h of data on 3 December 1999 and similar results have been obtained. Since there are a large number of satellites, or items of space debris, orbiting the Earth and, therefore, likely to pass through the radar beam, care must be taken to distinguish between the spectra caused by such phenomena and those caused by geophysical conditions. This applies not only to the ESR data, but to any radar data.

Further studies still need to be performed at the times of those anomalous echoes, not automatically rejected as being due to satellite contamination, to determine whether or not these are genuinely of a geophysical nature. Since the occurrences of enhanced spectra due to geophysical conditions are small, automated search routines of the type described here provide the scope for extracting such data from very large extended data sets. This method can assist in the investigation of naturally enhanced spectra and their causes.

Acknowledgements. We are indebted to the director and staff of EISCAT for opening the facility and supplying the data. EISCAT is an international facility supported by the national science councils of Finland, France, Germany, Japan, Norway, Sweden, and the United Kingdom. We thank Mike Rietveld, Russell Eberst and Alan Pickup for their help in obtaining the satellite data and directing us to appropriate tracking programs. Our thanks are also due to Rick von Glahn for allowing us to use results from the Element Manager for Windows program. The authors have greatly appreciated the helpful comments and suggestions made by the referee. The satellite tracking software and catalogue files used in this study were obtained from the following wedsites: http://www.eoss.org/elementmanager/index.html and ftp://ftp.seds.org/pub/sat/satelem/el-1999/

Topical Editor M. Lester thanks F. Sedgemore-Schulthess for his help in evaluating this paper.

References

Buchert, S. C., van Eyken, A. P., Ogawa, T., and Watnabe, S.: Naturally enhanced ion-acoustic lines seen with the EISCAT Svalbard Radar, Adv. Space. Res., 23, 1699–1704, 1999.

Collis, P. N., Häggström, I., Kaila, K., and Rietveld, M. T.: EISCAT radar observations of enhanced incoherent scatter spectra; their relation to red aurora and field-aligned currents, Geophys. Res. Lett., 18, 1031, 1991.

Forme, F. R. E: Parametric decay of beam-driven Langmuir wave and enhanced ion-acoustic fluctuations in the ionosphere: a weak turbulence approach, Ann. Geophysicae, 17, 1172, 1995.

Foster, J. C., del Pozo, C., and Groves, K.: Radar observations of the onset of current driven instabilities in the topside ionosphere, Geophys. Res. Lett., 15, 160, 1988.

Rietveld, M. T., Collis, P. N., van Eyken, A. P., and Lovhaug, U. P.: Coherent echoes during EISCAT UHF Common Programmes, J. Atmos. and Terr. Phys., 58, 161–174, 1996.

Rietveld, M. T., Collis, P. N., and St-Maurice, J.-P.: Naturally enhanced ion acoustic waves in the auroral ionosphere observed with the EISCAT 933-MHz Radar, J. Geophys. Res., 96, 19 291, 1991.

Risbeth, H. and Williams, P. J. S.: The EISCAT ionospheric radar: The system and its early results, Q. J. R. Astr. Soc., 26, 478–512, 1985.

Sedgemore-Schulthess, F., Lockwood, M., Trondsen, T. S., Lanchester, B. S., Rees, M. H., Lorentzen, D. A., and Moen, J.: Coherent ESR spectra from the dayside cusp/cleft and their implications for transient field-aligned currents, J. Geophys. Res., 104, 24 613–24 624, 1999.

Sedgemore-Schulthess, F. and St-Maurice, J.-P.: Enhanced ion-acoustic spectra and their interpretation, Surv. Geophys., 22, 1, 55–92, 2001.

Wahlund, J.-E., Forme, F. R. E., Opgenoorth, H. J., and Persson, M. A. L.: Scattering of electromagnetic waves from a plasma: Enhanced ion-acoustic fluctuations due to ion-ion two-stream instabilities, Geophys. Res. Lett., 19, 1919–1922, 1992.

Wannberg, G., Wolf, I., Vanhainen, L. G., Koseniemi, K., Rõttger, J., Postila, M., Jacobsen, R., Stenberg, A., Larsen, R., Eliasen, S., Heck, S., and Huuskonen, A.: The EISCAT Svalbard Radar: A case study in modern incoherent scatter radar system design, Radio Sci., 32, 2283–2307, 1997.